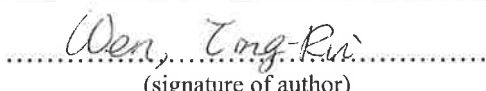




Universitetet
i Stavanger

FACULTY OF SCIENCE AND TECHNOLOGY

MASTER'S THESIS

Study programme/specialisation: Offshore Technology/ Marine and Subsea Technology	Spring semester, June, 2018 Open
Author: Ting Rui Wen	 (signature of author)
Programme coordinator: Supervisor(s):	Professor Muk Chen Ong Prof. Muk Chen Ong/ Dr. Kai Wang/ Dr. Zhengshun Cheng
Title of master's thesis: Feasibility study and dynamic analysis of floating vertical axis wind turbines in multi-applications	
Credits: 30 ECTS	
Keywords: Offshore wind; floating vertical axis wind turbine; dynamic response; water depth; wave energy converter; combined concept.	Number of pages: 96 + supplemental material/other: none Stavanger, June 15/ 2018 date/year



Universitetet
i Stavanger

FACULTY OF SCIENCE AND TECHNOLOGY

MASTER'S THESIS

Study programme/specialisation: Offshore Technology/ Marine and Subsea Technology	Spring semester, June, 2018 Open
Author: Ting Rui Wen (signature of author)
Programme coordinator: Supervisor(s):	Professor Muk Chen Ong Prof. Muk Chen Ong/ Dr. Kai Wang/ Dr. Zhengshun Cheng
Title of master's thesis: Feasibility study and dynamic analysis of floating vertical axis wind turbines in multi-applications	
Credits: 30 ECTS	
Keywords: Offshore wind; floating vertical axis wind turbine; dynamic response; water depth; wave energy converter; combined concept.	Number of pages: 96 + supplemental material/other: none Stavanger, June 15/ 2018 date/year

ABSTRACT

In the past decades, the global wind energy has rapidly grown. Greater potential of wind resources is explored in the deeper sea; hence, wind farms have progressively moved toward the deep water over the years. Floating wind turbines then become an available solution which could be widely applied to deep water. Spar, semi-submersible and tension-leg platform (TLP) are the main types of floating substructure for supporting the wind turbine. The wind turbine can be generally categorized into horizontal axis wind turbine (HAWT) and vertical axis wind turbine (VAWT) in terms of the direction of the rotating axis. Compared to floating HAWTs, floating VAWTs have several advantages such as lower maintenance and operational costs etc. The deployment of floating VAWTs starts to arouse people's attention. Recently, the applications of floating VAWTs in deep water have been studied by several researchers. However, the feasibility of deploying a floating VAWT at a moderate water depth has not yet been discussed.

In addition, offshore wind energy is not the only source to produce power in a marine environment. Wave energy exists huge potential to be utilized. The combined concept that can harvest both wind and wave resources becomes another alternative solution, which could lower the cost and increase the power efficiency. Several concepts of the integrated system which combines a floating HAWT and a wave energy converter (WEC) have been proposed and discussed, such as a semi-submersible HAWT with the flap-type WEC, a combination of spar-type HAWT and a torus-shape WEC, etc. Considering the advantages of the floating VAWT, an integration of the WEC and the floating VAWT deserves a further investigation and evaluation.

This study is inspired by the merits of the floating VAWT and the successful experience of the Hywind project in Scotland. The thesis aims to investigate and assess the feasibility of the spar-type VAWT in multi-applications. A short spar VAWT at moderate water depth and a combined torus-shape wave energy converter and spar-type VAWT concept (STC VAWT) in deep water are studied under operational conditions. Both concepts are compared with a spar-type VAWT in deep water to evaluate its advantages and disadvantages.

In the first concept, a short spar VAWT supporting a 5 MW Darrieus rotor at moderate water depth is proposed by following the deep spar concept in deep water. This feasibility is thoroughly addressed by comparing the dynamic responses of spar-type

VAWTs in deep water and moderate water depth. A fully coupled simulation tool, SIMO-RIFLEX-DMS code, is utilized to carry out time domain simulations under turbulent wind and irregular waves. Dynamic responses of the short spar and deep spar VAWTs are analyzed and compared, including the natural periods, wind turbine performance, platform motions, tower base bending moments, and tension of mooring lines. The statistical characteristics of the thrust and power production for both spars are similar. The comparison of platform motions and tower base bending moments demonstrate a good agreement for both spars, but the short spar has better performance in surge/sway motions and side-side bending moments. The 2P response dominates the bending moment spectra for both spars. A significant variation in tension of Mooring Line 1 and a larger corresponding spectrum value are found in the short spar concept. The results indicate that the application of short spar VAWTs is feasible and could become an alternative concept at moderate water depth.

An integration of spar-type VAWT and a torus-shape wave energy converter (STC VAWT) is considered in the second concept. This combined concept utilizes the relative heave motion between the torus and the spar buoy to harvest the wave energy. An integrated aero-hydro-servo-elastic tool (SIMO-RIFLEX-DMS code) is used to study the power performance and the dynamic response of the STC VAWT under operational conditions with the combinations of turbulent wind and irregular wave. The strength and weakness of the second concept are explored in comparison with the spar-type VAWT. The WEC can provide additional power and increase the total amount of production in the combined concept. The 2P loadings of the STC VAWT show a good agreement with the spar-type VAWT. The additional torus is exposed to larger wave excitation force, which leads to significant variations of hydrodynamic loads on the STC. The torus acts as a damper at the mean sea level, which could mitigate the variation of the floater motion in surge/sway/pitch. The heave natural period of the STC system is in the same range with ocean wave periods. A larger heave response may be excited during operation, whereas it is beneficial for wave energy absorption. The statistical result indicates that the STC gives larger standard deviations of tower base bending moments than the spar-type VAWT, which is due to the torus effect. The larger variations of the tension of Mooring 1, which is aligned with the wind and waves, are also observed in the combined concept. Overall, the STC VAWT is applicable in the operational stage, and a further study on the current condition or extreme environments is recommended in the future.

KEYWORDS: Offshore wind; floating vertical axis wind turbine; dynamic response; water depth; wave energy converter; combined concept.

ACKNOWLEDGEMENTS

Firstly, I must thank profusely my main supervisor, Professor Muk Chen Ong, for his organizational arrangements throughout this entire thesis work. He always motivates me with his unique insight to pursue an advanced performance. Spurred by his encouragements and greetings, I have accomplished a personal achievement in the academic field within a limited time.

I would like to extend my deep gratitude to my co-supervisor, Dr. Kai Wang, who is just like my mentor as well as my friend. His practical experience in the industry assists me to establish the numerical model. His valuable advice and patient guidance to the simulation tools are the keys for the completion of my first study.

Moreover, I would like to express my sincere appreciation for all the assistance from another co-supervisor, Dr. Zhengshun Cheng. He always responds to me and solves my questions at the first time. His attitude to the academic work has inspired me. His logical and clear thinking give me huge supports to carry out my second study.

It is my great honor to join Prof. Ong's research team and work together with many remarkable people. I appreciate Dr. Lin Li's proper advice. I would like to show my special thanks to Marek and Carlos, who do me a favor while I was in a tough time. I would also thank the fellow students: Efratos, Kunal, Kristian, Antonius, Sebastian, Bahram, Julio, Eliana, and so on. I will cherish the memories of the time we spent together in Norway.

Last but not least, I would like to show my heartfelt gratitude to my whole family members. Their moral support allows me to fulfill my dream in the distant country. I am going to devote this accomplishment to my family and share my pleasure with them, especially for my wife and my lovely sweetheart.

ABBREVIATIONS

1P	One per Revolution
2P	Two per Revolution
COB	Center of Buoyancy
COG	Center of Gravity
COM	Center of Mass
DMS	Double-Multiple Streamtube
FVAWT	Floating Vertical Axis Wind Turbine
HAWT	Horizontal Axis Wind Turbine
IEC	International Electrotechnical Commission
JONSWAP	Joint North Sea Wave Project
MWL	Mean Water Level
NTM	Normal Turbulence Model
PI	Proportional Integral
PTO	Power Take-Off
SFC	Semisubmersible and Flap-type wave energy Converter
STC	Spar Torus Combination
TLP	Tension Leg Platform
VAWT	Vertical Axis Wind Turbine
WADAM	Wave Analysis by Diffraction and Morison Theory
WEC	Wave Energy Converter

LIST OF APPENDED PAPER

This thesis is written as the collection of introductory part, one paper and one specific study which is planned to publish in the future. The information of this paper is given as follow and is attached in Appendix A.

Paper 1:

Spar-type vertical-axis wind turbines in moderate water depth: A feasibility study

Ting Rui Wen, Kai Wang, Zhengshun Cheng and Muk Chen Ong

Published in *Energies* 2018, 11(3), 555

DECLARATION OF AUTHORSHIP

Regarding the authorship in Paper 1, I am the first author and take responsible for numerical modeling, dynamic simulations, data analysis and writing the paper under the supervision of Dr. Kai Wang, Dr. Zhengshun Cheng and Professor Muk Chen Ong. Dr. Kai Wang and Professor Muk Chen Ong conceived and designed the numerical study. Dr. Kai Wang gave me huge support for the numerical model and he is one of the original developers of SIMO-RIFLEX-DMS code. Dr. Zhengshun Cheng improved the controller system and provided many valuable comments.

TABLE OF CONTENTS

ABSTRACT.....	i
ACKNOWLEDGEMENTS.....	iii
ABBREVIATIONS.....	iv
LIST OF APPENDED PAPER.....	v
DECLARATION OF AUTHORSHIP.....	v
TABLE OF CONTENTS.....	vi
LIST OF TABLES.....	viii
LIST OF FIGURES.....	ix
1. INTRODUCTION.....	1
1.1. General background and motivation.....	1
1.2. Scope and outline of this thesis.....	8
2. THEORY.....	11
2.1. Modeling of wind and wave.....	11
2.1.1 Wind.....	11
2.1.2 Waves.....	14
2.2. Aerodynamic load.....	15
2.2.1 Overview of aerodynamic models.....	15
2.2.2 Double Mutli-Streamtube (DMS) model.....	15
2.3. Hydrodynamic load.....	18
2.3.1 Potential flow theory.....	18
2.3.2 Application of Morison's equation.....	21
2.4. Stability of floating structure.....	22
2.4.1 Initial stability.....	22
2.4.2 Mooring system.....	23
2.5. Integrated dynamic analysis of a floating VAWT system.....	25
3. FLOATING WIND TURBINE CONCEPTS.....	28
3.1. Deep spar and short spar VAWTs concepts.....	28
3.2. Spar-Torus Combination concept.....	32
3.2.1 Torus.....	32
3.2.2 Spar VAWT.....	34
3.2.3 Coupled connections between Torus and Spar VAWT.....	34
3.3. Numerical modeling for floating VAWTs.....	36

3.3.1	HydroD model	36
3.3.2	SIMO model.....	41
3.3.3	RIFLEX model.....	47
3.3.4	DMS model.....	47
3.4.	Environmental conditions	48
4.	DYNAMIC ANALYSIS OF SPAR VAWTS	50
4.1.	Initial position of the dynamic model	50
4.2.	Natural period of spar VAWTs	50
4.3.	Wind turbine performance	51
4.4.	Platform motion	55
4.5.	Tower base bending moments.....	60
4.6.	Mooring line tension.....	63
5.	DYNAMIC ANALYSIS OF STC VAWT.....	65
5.1.	Coupled motion of torus and spar.....	65
5.2.	Power performance	68
5.2.1	Optimum analysis of PTO parameters.....	68
5.2.2	Power production of the VAWT.....	69
5.2.3	Power production of the WEC.....	71
5.2.4	Estimation of annual power production.....	72
5.3.	Natural period of STC.....	73
5.4.	Aerodynamic load.....	74
5.5.	Hydrodynamic load.....	76
5.6.	Floater motion.....	79
5.7.	Tower base bending moments.....	83
5.8.	Mooring line tension.....	85
6.	CONCLUSIONS.....	87
7.	RECOMMENDATIONS FOR FUTURE WORK.....	90
	REFERENCES	92
	APPENDIX A: Paper 1	
	APPENDIX B: Caculation sheet for short spar VAWT	

LIST OF TABLES

Table 3.1.	Specifications of the Darrieus 5 MW wind turbine.....	29
Table 3.2.	Properties of the deep spar and the short spar	29
Table 3.3.	The properties of mooring system components	30
Table 3.4.	Properties of the torus in the STC concept.....	33
Table 3.5.	Properties of the coupled connections between the torus and the spar ...	35
Table 3.6.	Key parameters of the mass model in the short spar VAWT.....	38
Table 3.7.	Key parameters of the mass model in the STC concept.....	39
Table 3.8.	The body mass data in the short spar model	41
Table 3.9.	Mass of moment inertia with each type of cylinder	42
Table 3.10.	Quadratic drag force coefficient in SIMO	42
Table 3.11.	Linear stiffness matrix terms in the short spar	43
Table 3.12.	Quadratic drag force coefficient of the torus	44
Table 3.13.	Environmental loading for the normal operating condition.....	49
Table 4.1.	Initial positions of all bodies in the short spar VAWT	50
Table 4.2.	Natural period of the short and deep spar VAWTs	51
Table 4.3.	Mean rotor speed for all loading cases.....	52
Table 5.1.	Mean rotor speed of the STC VAWT for all loading cases	70
Table 5.2.	Natural periods of the spar-type VAWT and the STC VAWT	74

LIST OF FIGURES

Figure 1.1.	The development of global wind energy between 2001 to 2017.....	1
Figure 1.2.	Typical HAWT and VAWT	2
Figure 1.3.	Typical concepts of floating wind turbine foundation.....	3
Figure 1.4.	The inherent advantage of the floating VAWT	4
Figure 1.5.	Typical type of wave energy converter.....	5
Figure 1.6.	The concepts of combined offshore wind and wave energy.....	6
Figure 2.1.	Double Multiple-Streamtube Model for a Darriues wind turbine	16
Figure 2.2.	The relative velocity and force of the blade in a horizontal view	17
Figure 2.3.	The superposition of hydrodynamic loads on a floating structure	20
Figure 2.4.	The gravity and buoyancy force in a submerged body.....	22
Figure 2.5.	An illustration for the inclined barge position.....	23
Figure 2.6.	The catenary mooring layout.....	24
Figure 2.7.	The relationship between the rotor rotational speed and the wind speed for an improved control system	27
Figure 3.1.	The concept of the deep spar and short spar VAWTs	30
Figure 3.2.	The diagram of the mooring system for the short spar and deep spar...	31
Figure 3.3.	The illustration of the STC VAWT and the spar-type VAWT.....	32
Figure 3.4.	The illustration of the mooring system for the STC VAWT concept	33
Figure 3.5.	The coupled connection between the torus and the spar	35
Figure 3.6.	Computation flowchart for the coupled model.....	36
Figure 3.7.	A mesh illustration for the short spar model in Genie.....	37
Figure 3.8.	The illustration of the short spar in HydroD.....	38
Figure 3.9.	Mesh illustrations for the spar and torus in Genie.....	39
Figure 3.10.	Panel models of the STC concept in HydroD	40
Figure 3.11.	The illustration of specified force in the short spar.....	43
Figure 3.12.	The motion mechanism of the docking cone coupling	45
Figure 3.13.	The mechanism of the fender coupling	46
Figure 3.14.	The properties of the fixed elongation couplings.....	46
Figure 3.15.	Mooring line of the short spar VAWT in X-Z plane.....	47
Figure 4.1.	Free decay tests for the short spar VAWT	51
Figure 4.2.	Comparison of time series in rotor speed for the short spar and deep spar under LC3.....	52

Figure 4.3.	Mean rotor speed for the short and deep spar VAWT with error bar representing the standard deviation	53
Figure 4.4.	Comparison of time series in 2P loading for the short and deep spar VAWTs under LC3	54
Figure 4.5.	Comparison of mean and standard deviation of the 2P loading for the short and deep spar VAWTs under all loading cases.....	54
Figure 4.6.	Mean power production for the short and deep spar VAWT with error bar representing the standard deviation	55
Figure 4.7.	Comparison of time series in surge, pitch, roll, and yaw motions for the short and deep spar VAWT under LC3	56
Figure 4.8.	Comparison of mean values with error bar indicating the standard deviation in surge, pitch, roll, and yaw motions for the short and deep spar VAWT.....	56
Figure 4.9.	Comparison of power spectra in six degrees of freedom for the short and deep spar VAWT under LC3	57
Figure 4.10.	Power spectra in surge under all loading cases for the short and deep spar.....	59
Figure 4.11.	Power spectra in yaw under all loading cases for the short and deep spar.....	59
Figure 4.12.	Time series of tower base bending moment for the short and deep spar under LC3.....	60
Figure 4.13.	Statistics of tower base bending moment for the short spar and deep spar VAWTs	61
Figure 4.14.	Power spectra of tower base bending moment under all cases	62
Figure 4.15.	Time series of the tension in Mooring Line 1 under LC3	63
Figure 4.16.	Statistics of the tension of Mooring Line 1 for the short spar and deep spar VAWTs	64
Figure 4.17.	Power spectra of the tension in Mooring Line 1 under all loading cases for the short and deep spar.....	64
Figure 5.1.	The coupled motion between the torus and the spar in the combined concept	65
Figure 5.2.	First order wave force in the vertical component of the torus and the spar under LC3.....	67
Figure 5.3.	The heave motion of the torus and the spar under LC3.....	67
Figure 5.4.	The heave velocity of the torus and the spar under LC3	67
Figure 5.5.	The velocity in heave of the torus relative to the spar under LC3.....	67
Figure 5.6.	The power production of the STC VAWT concept under LC3.....	68

Figure 5.7.	The optimum analysis of PTO parameters under different cases	69
Figure 5.8.	Mean rotor speed for the STC VAWT and the spar-type VAWT with error bar representing the standard deviation.....	70
Figure 5.9.	Power production of the STC VAWT and spar-type VAWT under all loading cases	71
Figure 5.10.	A comparison between wave and wind power production in the STC VAWT system under all loading cases.....	72
Figure 5.11.	The prediction of annual power production for the spar-type VAWT and the combined concept.....	73
Figure 5.12.	Free decay tests for the STC VAWT concept	73
Figure 5.13.	Statistical comparisons of aerodynamic loads between the spar-type VAWT and the STC VAWT under all loading cases	75
Figure 5.14.	The first order wave force in the vertical direction between the torus and the spar under LC4.....	76
Figure 5.15.	The wave excitation force in fore–aft direction between the torus and the spar under LC4.....	77
Figure 5.16.	Spectral analysis of wave excitation force in fore–aft for the torus and the spar under LC4.....	77
Figure 5.17.	Comparisons of resultant wave excitation force between the STC and the spar-type VAWT under LC4.....	78
Figure 5.18.	Comparative resultant wave excitation force in statistic under LC4 to LC6 between the STC and the spar-type VAWT	78
Figure 5.19.	The mean floater motion of the spar and the torus with the error bars representing the standard deviations in the STC VAWT system	79
Figure 5.20.	Floater motion with mean values and standard deviations under all loading cases for the spar in the STC and the spar-type VAWT	80
Figure 5.21.	The spectral analysis of the spar and the torus in the STC VAWT under LC3	81
Figure 5.22.	Comparisons of heave spectrum between the spar and the torus in the STC VAWT under different loading cases.....	81
Figure 5.23.	Comparative spectrum of floater motion between the spar in the STC and the spar-type VAWT under loading case LC3	82
Figure 5.24.	Comparisons of pitch spectrum between the spar in the STC and spar-type VAWT under different loading cases	83
Figure 5.25.	Comparative statistics of the tower base bending moment under all loading cases between the STC and the spar-type VAWT.....	84
Figure 5.26.	Comparisons of moment spectra between the STC and the spar-type VAWT under different loading cases	85

Figure 5.27. Comparisons of the tension of Mooring 1 in statistics between the
STC and the spar-type VAWT under all loading cases86

Figure 5.28. Power spectra of the tension in Mooring 1 for both the STC and the
spar-type VAWT under different loading cases86

1. INTRODUCTION

1.1. General background and motivation

The demand for and development of global wind power energy have both significantly increased in the past decades. Figure 1.1 shows that the annual installed wind capacity in 2017 is above 50 GW and brings the cumulative wind capacity up to 540 GW [1]. Wind power can be captured and converted into electricity through the use of wind turbines. Wind turbines are mainly classified into horizontal-axis wind turbines (HAWTs) and vertical-axis wind turbines (VAWTs) with regard to the direction of the rotating axis. As the aerodynamic efficiency of HAWTs is generally better than that of VAWTs, nowadays the application of HAWTs with higher commercial values is mainstream in the world wind energy industry.

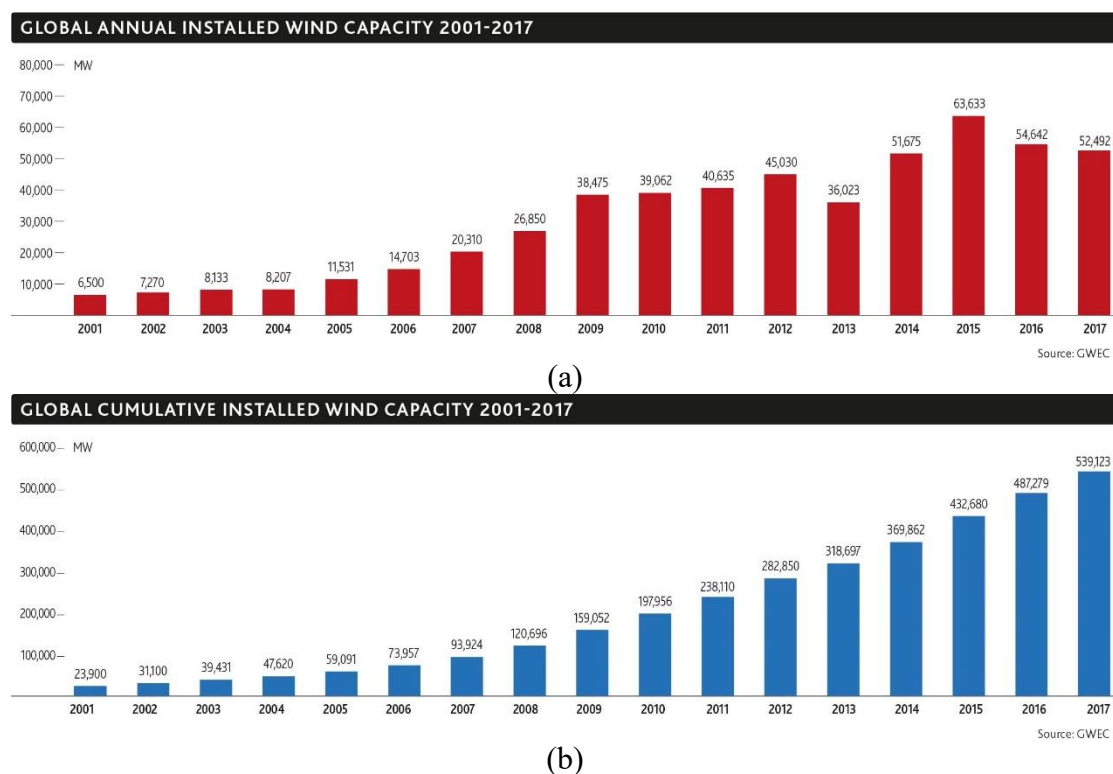


Figure 1.1. The development of global wind energy between 2001 to 2017 [1]: (a) Annual installed global capacity; (b) Global cumulative installed capacity.

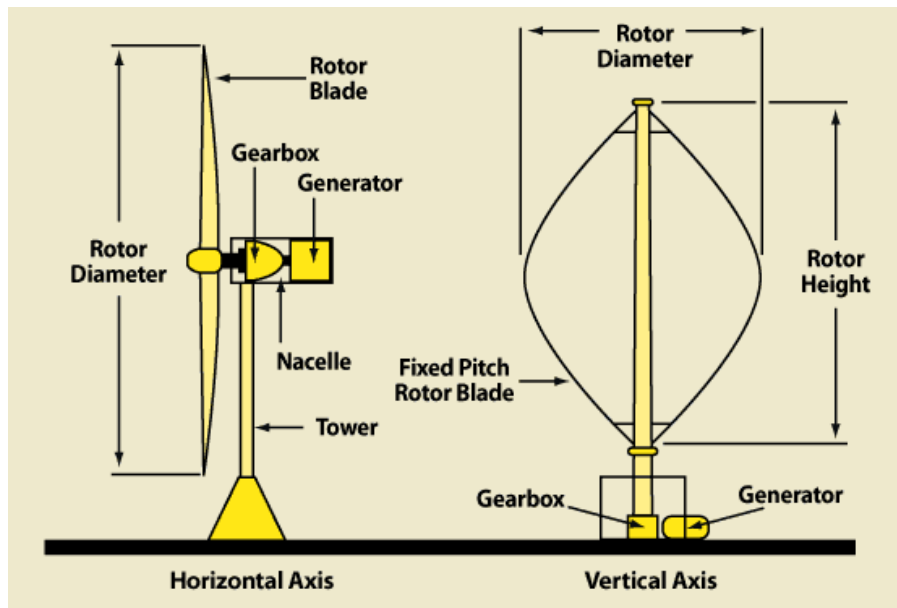


Figure 1.2. Typical Horizontal axis wind turbine (HAWT) and Vertical axis wind turbine (VAWT) [2].

Since greater wind resources and potential could be explored in deeper seas, wind farms are moving towards deep water in recent years. Floating offshore wind turbines have become an available solution which could be widely used in deep water. Spar, semi-submersible, and tension-leg platform (TLP)—which have been utilized in the oil and gas industry for a long time—are three primary types of floating structures for offshore wind turbines. The dynamic responses of these floating structures in the presence of the marine environment are crucial for their design purpose. The natural period of a floater is critical which can represent its dynamic behavior. Typically, a deeper spar is characterized by small heave motion, and its heave natural period usually locates outside the upper limit of the ocean wave periods. The spar is also well known for the soft behavior in horizontal plane, as the natural periods in surge/sway are generally higher than 100 seconds with respect to the station keeping system [3, 4]. Additionally, several prototypes of floating HAWTs have been developed, such as a catenary moored spar in the Hywind project in Norway, a semi-submersible in the WindFloat demo in Portugal, and a spar-type floating wind turbine in Japan's Minister of Environment (MOE) project at Kabashima in Japan [5]. A commercial floating wind farm, i.e., the Hywind Scotland by Statoil, started production in 2017 [6]. The feasibility of spar-type HAWTs at different water depths has been studied by Karimirad and Moan [7, 8]. Their research indicates that the short spar HAWT in moderate water depth exhibits good performance in dynamic responses and maintains almost the same power production as the deep spar HAWT in deep water.



Figure 1.3. Typical concepts of floating wind turbine foundation (Graphic from Josh Bauer, National Renewable Energy Laboratory) [9].

Floating VAWTs are a promising alternative to HAWTs due to their potential for cost-of-energy reduction and maintenance. Additionally, the structural scalability and the heavier components at the base of the structure allow a bigger rotor diameter for the VAWT to capture more energy. For the evolution of rotor size, floating VAWTs are more competitive. However, the development of floating VAWTs is still at an early stage. Some floating VAWT concepts have been proposed to explore their feasibility, such as a spar buoy with a two-bladed Darrieus rotor in the DeepWind project [10], and a Spinwind-1 prototype with a helical Darrieus rotor and a floater from the Gwind project [11], etc. Moreover, the DeepWind project was later extended for further investigation to include a 5 MW baseline rotor and an optimized blade design with less weight and higher stiffness [12, 13]. Several researchers have contributed mass efforts to floating VAWT studies in deep water conditions. Wang developed a fully coupled method (SIMO-RIFLEX-DMS code) for dynamic analysis and applied it to a semi-submersible VAWT [14]. Cheng developed another fully integrated method for VAWT numerical modeling (SIMO-RIFLEX-AC code) and studied the dynamic response for various concepts, such as the dynamic analysis of spar, TLP, and semi-submersible VAWTs, etc. [15]. Ugochukwu compared the structural dynamic responses of a 5 MW baseline floating VAWT and a 5 MW optimized floating VAWT with the DeepWind Darrieus rotor under steady and turbulent wind conditions [16]. Liu et al. presented a motion study of a 5 MW floating VAWT composed of a truss spar floating foundation with heave plates under decay tests, wind only, regular wave and wind, and irregular wind

and wave cases [17]. Overall, most of the available floating VAWT concepts have been evaluated in deep water, whereas the feasibility of deploying a floating VAWT at a moderate water depth has not yet been discussed.

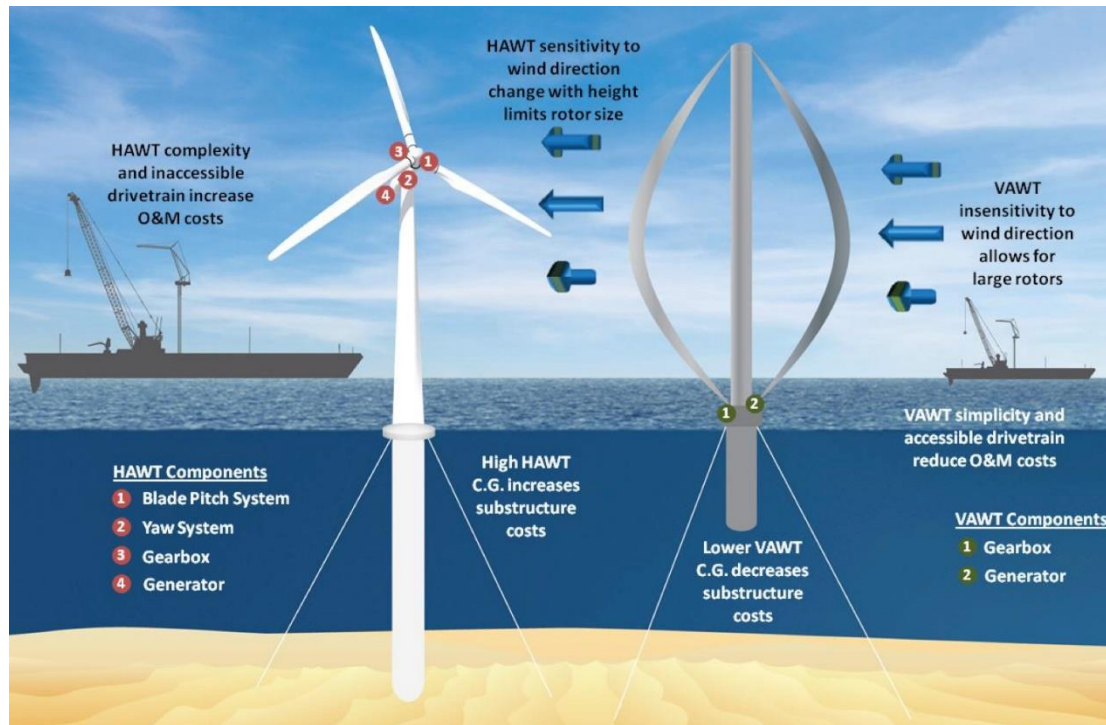


Figure 1.4. The inherent advantage of the floating vertical axis wind turbine (Graphic from Sandia National Laboratories) [18].

In addition, offshore wind energy is not the only way to generate electricity under the marine environment. There are still many potentials in harnessing the ocean energy, including waves, tides, salinity and the difference in ocean temperature, etc. During the past decades, numerous research on converting the wave energy into reliable power has been studied and proposed in the world [19]. Several types of wave energy converter (WEC) are considered as promising solutions with higher economic values by French [20], which consists of a two-body system and a power take-off (PTO) system. A detailed evaluation and study for eight wave energy converters to identify the power performance and annual absorbed energy through numerical simulations were published by Babarit et al. [21]. The working principle of each wave converters, which involve bottom-referenced type, floating heave mode, floating flap device, systematic array, and so on, depends on the water depth and the environmental conditions. Muliawan et al. [22] have done a further analysis of a floating two-body wave energy converter, which is formed with a torus, a floater, the power take-off system and the mooring system. The effects of the mooring configurations and the PTO parameters on the energy absorption have also been determined and assessed. Although so many

feasible concepts of the WEC have been proposed in the recent decade, it is hard to get involved in a real commercial phase. Still, the efficiency of the power production and a profitable manner in the market are two challenging issues for the future development of the wave energy converter.

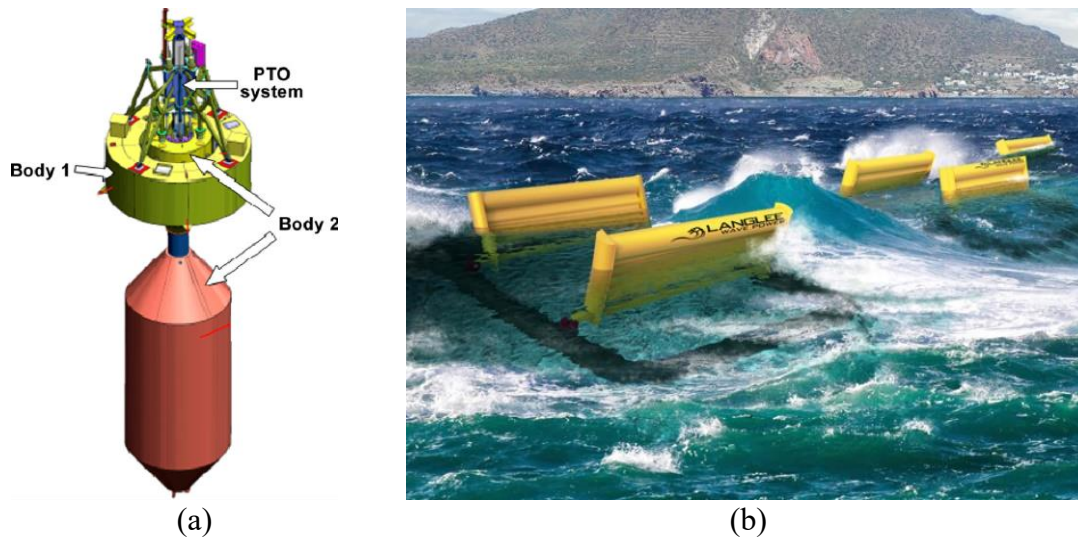


Figure 1.5. Typical type of wave energy converter: (a) Wavebob (Floating two body heave converter, graphic from Wavebob Ltd.) [19]; (b) Langlee WEC (Floating/oscillating flap type, graphic from Langlee Wave Power AS.) [23].

To lower the cost and increase the power efficiency, some alternative solutions came up afterward. One is to combine the wave energy converter with other practicable resources. Considering the natural correlation between the offshore wind and wave, the integration of a floating wind turbine and a wave energy converter become a possible solution. Both the floating structure and the wave energy can share the same platform, mooring systems, and the electrical cables. This idea could save not only the workspace but also the construction cost. In recent years, a European project—MARINA Platform—dedicated to developing the integrated systems, which could exploit the offshore wind and wave energy, and rendering these applications closer to the market requirements [24]. Several combined concepts have been proposed, and its comparisons of experimental data and numerical modelling have also been studied, such as a semi-submersible floating HAWT with the flap-type wave energy converter (SFC) [25, 26], a combination of spar-type HAWT and a torus-shape wave energy converter (STC) [27], and an oscillating water column wave energy converter on a floating foundation WindFloat [28], etc.

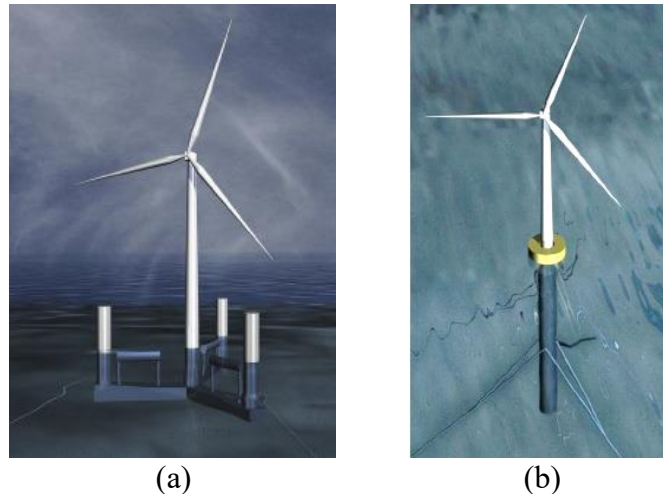


Figure 1.6. The concepts of combined offshore wind and wave energy: (a) Semisubmersible wind energy and Flap-type wave energy Converter (SFC) [25]; (b) Spar Torus Combination (STC) [29].

The STC concept is made up with one spar-type floating structure with HAWT, one torus-shape floater, the power take-off system (PTO) and the catenary mooring system. The offshore wind energy can be captured by the wind turbine, and the wave energy can be absorbed through the PTO system via a relative heave motion between the torus and the spar structure. The STC concept is suitable for the deployment in deep water, and it is not sensitive to seabed conditions or wave directions [27]. Numerical simulations with the dynamic response and power performance of the STC concept under operational modes and survival modes were studied by Muliawan et al [30, 31]. Moreover, the experimental and numerical comparisons of hydrodynamic responses for the STC concept were performed by Wan et al. [29]. For a long-term performance of STC concept, two additional survival modes were proposed and the power production, structural fatigue damage, and extreme responses were also investigated by Ren et al. [32]. Overall, the comprehensive scientific research of the STC HAWT concept has been recently studied by many remarkable scholars. Owing to the potential strength of the floating vertical axis wind turbine (VAWT), the combination of the WEC and a floating VAWT will then become another novel issue and deserve a further investigation and evaluation.

This study is inspired by the merits of the floating VAWT and the successful experience of the operation and production for spar-type HAWTs of the Hywind project in Scotland. The thesis aims to investigate and assess the feasibility of the spar-type VAWT in multi-applications. The first part of the study addresses the dynamic behavior of a short spar VAWT at moderate water depth. The second part of the study focuses on the performance of the power production, dynamic response and the structural stability of a Spar-Torus Combination (STC) VAWT concept in deep water. The dynamic responses

of both concepts are analyzed through a fully coupled simulation tool, SIMO-RIFLEX-DMS. The advantages and disadvantages of each concept are discussed and compared with a spar-type VAWT in deep water, which was proposed by Cheng et al. [33]. These research outcomes can also be provided as the conceptual selections for a decision maker and be beneficial to the development of the renewable energy in the future market.

1.2. Scope and outline of this thesis

The main scope of the thesis is to investigate the feasibility of two different spar-type VAWT concepts—which are short spar VAWT and Spar-Torus Combination (STC) VAWT—and analyze its dynamic responses through numerical modeling. Several sub-scopes of the study have been defined and achieved, as listed in the following:

A. Short spar VAWT concept

- To establish a numerical model of the short spar VAWT in moderate water depth 150m.
- To establish five set of environmental cases, which are the combinations of turbulent wind and irregular wave in an operational condition.
- To perform one-hour duration of dynamic simulation with five random seeds for each environmental case.
- To investigate the aerodynamic performance and evaluate the dynamic response of the platform motion, tower base bending moment and tension of mooring.
- To compare the result with that of a spar-type VAWT concept in deep water by Cheng et al. [33] and discuss the pros and cons of the proposed concept.

B. Spar-Torus Combination (STC) VAWT concept

- To establish a numerical model of the STC VAWT in deep water 320m.
- To set up five environmental cases under the operational condition which are identical with the cases in short spar VAWT concept.
- To find the optimum PTO parameters based on the environmental cases so that the performance of the wave energy converter could be optimized.
- To run one-hour simulations of dynamic analysis with five random seeds for each case accounting for the stochastic variations.
- To explore the effect of the torus on the power performance.

- To investigate the aerodynamic load, hydrodynamic load, the dynamic response of floaters motion, tower base bending moment and tension of mooring.
- To evaluate the result and discuss the comparison of the difference between the STC VAWT and a spar-type VAWT concept by Cheng et al. [33].

Additionally, the thesis is written in the form of one journal paper of the short spar VAWT and one concept of Spar-Torus Combination VAWT. The paper of the short spar VAWT is included in Appendix A and briefly introduced.

Paper 1: In this paper, a short spar VAWT with catenary mooring lines carrying a 5 MW Darrieus rotor in a moderate water depth (150 m) is proposed. A comparative study between the proposed concept and a concept of deep spar VAWT by Cheng et al. [33] is carried out. The dynamic response and power performance of both the spar VAWTs are analyzed through a fully coupled SIMO-RIFLEX-DMS code under different combinations of irregular wind and wave for operating conditions. The power productions of both the spar VAWTs are similar. The short spar VAWT displays a smaller motion in surge/sway, but it behaves higher variation in tension of mooring line 1. The tower base bending moment spectra of both the spar VAWTs are controlled by the 2P response. The results indicate that the deployment of the short spar VAWT in moderate water depth is feasible.

Finally, the outline of this thesis involves seven chapters, which are briefly summarized in the following parts:

Chapter 1: The general background and motivation of the study are introduced, and the scope of work and outline are defined. Part of contents from **Paper 1** is included in this chapter.

Chapter 2: The main theory of this study and related literature reviews are summarized in this chapter.

Chapter 3: The methodology and modeling of the short spar VAWT, the deep spar VAWT by Cheng et al. [33], and the Spar-Torus Combination (STC) VAWT are presented. The environmental conditions in an operational mode are introduced. This chapter covers part of the contents from **Paper 1**.

Chapter 4: The dynamic analysis of the short spar VAWT is included. A comparative study of power performance, platform motions, tower base bending moments, and tension of mooring lines between the short spar VAWT in moderate water and deep spar VAWT by Cheng et al. [33] in deep water is discussed. This chapter mainly covers the simulation results from **Paper 1**.

Chapter 5: This chapter deals with an overall dynamic analysis of the Spar-Torus Combination (STC) VAWT. The coupled motion between the torus and the spar is firstly investigated. The power performance and structural stability of the STC VAWT concept are addressed. A discussion of the captured wind energy and absorbed wave energy for the proposed concept is presented. The influence of the torus on the structural dynamic of the STC VAWT model is studied and emphasized. The comparison of STC VAWT and a concept of spar-type VAWT, which is identical with the deep spar VAWT by Cheng et al. [33], are also discussed.

Chapter 6: A summary of the thesis is included in this chapter. The main conclusions and the feasibility of each proposed concepts are addressed here.

Chapter 7: The last part involves the recommendations for the future work of the thesis.

2. THEORY

This section generally introduces basic theories about the dynamic analysis of a floating VAWT system. The numerical simulations of wind and wave are given in the first part. The aerodynamic model of the vertical axis wind turbine and the hydrodynamic loads on the floating structure are addressed. The initial stability of the floating structure and mooring are presented. The principle of an integrated dynamic analysis of floating VAWT and a control system are shown in the last part.

2.1. Modeling of wind and wave

This section addresses the theory of the wind field generation and the wave profile. To reflect the stochastic variations of wind and wave, a turbulent wind model and irregular wave model are applied to this study. The spectra of wind and wave are utilized to give the energy distribution with various frequencies. The wind and wave spectra are then provided as the inputs for further calculations on the aerodynamic and hydrodynamic loads. Aforementioned theories are summarized in the first section.

2.1.1 Wind

Power of law is one of the prominent theories to describe the profile of the wind speed. The wind speed may vary with the height, and the gradient of wind speed profile is controlled by the atmospheric stability and the terrain conditions. The mean wind speed $U(z)$ at certain height z is expressed in the following equation [34]:

$$U(z) = U(z_{ref}) \left(\frac{z}{z_{ref}} \right)^\gamma$$

Where $U(z_{ref})$ is the mean wind speed at reference height z_{ref} and the exponent γ depends on the terrain conditions; z_{ref} is the reference height which is 79.78 meters above mean water level in this study; Due to the offshore condition, γ is defined as 0.14 according to IEC 61400-1 Class C [35].

The turbulent wind with the characteristic of violent change of pressure and wind velocity could reflect the real situation during operation. A dissipation of kinetic energy of wind into the thermal due to the flow across the boundary layer could cause this phenomenon. A turbulence intensity is usually used to quantify this effect, which is

defined as the ratio of standard deviation of the wind speed and the mean speed in a time series of record.

$$I = \frac{\sigma}{\bar{U}}$$

The turbulence characteristics will vary with the wind speed. IEC 61400-3 gives the expression for the standard deviation of the longitudinal wind speed component [35]. The turbulence intensity I_{15} is determined at $u_{hub}=15\text{m/s}$, which could follow the IEC standard with the different type of Class.

$$\sigma_u = \frac{u_{hub}}{\ln(z_{hub}/z_0)} + 1.28 \times 1.44 \times I_{15}$$

A turbulent wind field can be generated through the Turbsim program by using a statistical model to numerically simulate the time series of wind fields [34]. The IEC Kaimal turbulence model is applied to this study, which can be described by a velocity spectrum and presented in the equation below.

$$S_k(f) = \frac{4\sigma_k^2 \cdot L_k / \bar{u}_{hub}}{(1 + 6f \cdot L_k / \bar{u}_{hub})^{5/3}}$$

where k denotes u, v, w in longitudinal, lateral and vertical direction, respectively; f is the cyclic frequency; \bar{u}_{hub} is the mean wind speed at hub height; σ_k is the standard deviation and the relation in different direction is defined in the following expressions; L_k is an integral scale parameter and is proportional to the turbulence scale parameter Λ_U ; The minima of the hub height z_{hub} and 60 meters could determine the turbulence scale parameter.

$$\sigma_v = 0.8\sigma_u$$

$$\sigma_w = 0.5\sigma_u$$

$$L_k = \begin{cases} 8.10\Lambda_U, & k = u \\ 2.70\Lambda_U, & k = v \\ 0.66\Lambda_U, & k = w \end{cases}$$

$$\Lambda_U = 0.7 \times \min(60\text{m}, z_{hub})$$

Additionally, the neutral stability is assumed in this model which implies the gradient Richardson number is equal to zero. A grid height and width should be specified in Turbsim program which needs to cover the whole area of the vertical axis wind turbine. This velocity spectra from the IEC Kaimal model is assumed to be invariant across the whole grid, but a small amount of variation of the standard deviation in longitude direction exists due to a spatial coherence [34]. The spatial coherence from the IEC spectral model in u component between point i and j is given below:

$$Coh_{i,j} = exp\left(-a \sqrt{\left(\frac{f \cdot r}{\bar{u}_{hub}}\right)^2 + \left(0.12 \frac{r}{L_c}\right)^2}\right)$$

where f is frequency; r is the distance between point i and j; a and L_c are the coherence decrement and coherence scale parameter, respectively, which are recommended by the IEC 61400-1 as follow [35].

$$a = 12$$

$$L_c = 5.67 \times \min(60m, z_{hub})$$

The coherence in v and w components are not specified by IEC standard; hence, these values are implemented with zero. The constant standard deviations in v and w components will cover the whole grid. Finally, the velocity distribution in the time domain can be generated from the velocity spectrum by doing an inverse fast Fourier transform.

2.1.2 Waves

The free surface of waves is a stochastic process with random probability in nature. In order to describe the real sea surface, a sum of sinusoidal wave components is usually used for a simplified solution. A sea state can be either long-term or short-term condition. In this thesis, the short-term sea state which is a duration of one hour will be applied. Wave spectrum is often used to define the energy of sea state within a short-term condition. Several spectra have been developed to describe the sea state for the short-term condition, and the JONSWAP spectrum is adopted in the following simulation.

The JONSWAP spectrum was established from a well-known joint research project, the “Joint North Sea Wave Project”. It was based on wave measurements which started from Sylt and extended 160 km into the North Sea during the period of 1968 to 1969. The JONSWAP spectrum can be used to describe the sea state, which could consider both conditions of under developing sea and fully developed sea. The JONSWAP spectrum is defined as follows [36]:

$$S_{\xi}(\omega) = \frac{\alpha g^2}{\omega^5} \exp\left(-\beta \left(\frac{\omega_p}{\omega}\right)^4\right) \gamma^{\exp\left(\frac{(\omega/\omega_p-1)^2}{2\alpha^2}\right)}$$

where ω_p is the peak frequency which is equal to $2\pi/T_p$; γ is the peakedness parameter and a typical value of 3.3 refers to a non-fully developed sea state; β is form parameter and the default value is set to 1.25; σ is the spectral parameter which is either 0.07 ($\omega < \omega_p$) or 0.09 ($\omega > \omega_p$); α is the spectral parameter, but the significant wave height H_s , is often used to parameterize the spectrum.

$$\alpha = \left(\frac{H_s \omega_p^2}{4g}\right)^2 \frac{1}{0.065\gamma^{0.803} + 0.135}$$

The shape of JONSWAP may be controlled by several key parameters, which are H_s , T_p , and γ . As increasing the significant wave height H_s and the peak period T_p , the wave energy and the potential instability of a floating structure are also increased. The parameter γ determines the peakedness of the spectrum.

2.2. Aerodynamic load

The wind field data, the geometry of the blade, Reynolds number, drag and lift coefficients are the key inputs for calculating the aerodynamic loads on a rotor. Several main aerodynamic models of vertical wind axis turbine will be briefly introduced in the first section. The improved double multi-streamtube (DMS) is applied to this study and addressed in the second part.

2.2.1 Overview of aerodynamic models

The first Darrieus-type vertical axis wind turbine was invented by a French aeronautical engineer—Georges Darrieus—in the early 20th century. Sandia National Laboratories has launched a series of researches on vertical wind axis turbine since 1970. A plenty of aerodynamic models are developed to simulate the dynamic behavior of the rotor, including streamtube models, actuator cylinder (AC) flow model, cascade models, panel models, vortex models, computational fluid dynamic (CFD) models and so on. The basis of streamtube models comes from the conservation of mass and momentum in a quasi-steady flow. The streamtube models can be generally categorized into three types: (a) single streamtube model; (b) multi-streamtube model; (c) double multi-streamtube (DMS) model. The DMS model can perform a better accuracy on the aerodynamic load than the rest of two streamtube models, since the variation of induced velocity with the azimuth angle in each streamtube is considered. In this study, the DMS model is utilized to estimate the aerodynamic loads on the VAWT, and a detailed explanation is given in the next section.

2.2.2 Double Mutli-Streamtube (DMS) model

The double multi-streamtube (DMS) model initially proposed by Paraschivoiu [37], and it was applied to a land-based vertical axis wind turbine. For a floating VAWT, the pitch or roll motion will lead to a tilt at the tower of the wind turbine. This resulting effect on the aerodynamics could be different from the behavior of the original situation. Thus, an improved DMS model was developed by Wang [38] to consider the tower tilting effect. The general idea is described as follows.

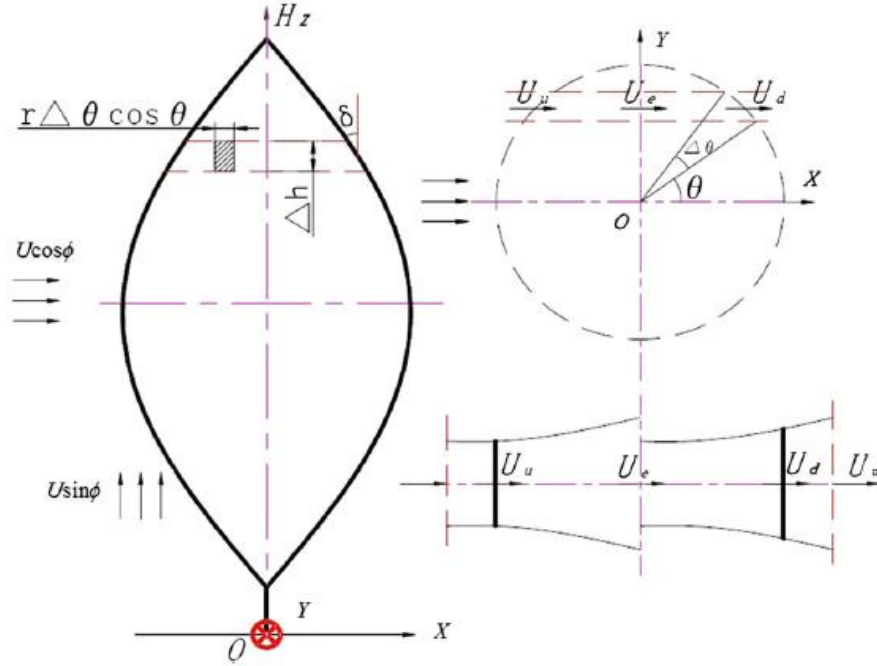


Figure 2.1. Double Multiple-Streamtube Model for a Darrieus wind turbine with two actuator disk in tandem with a horizontal and vertical inflow [38].

Figure 2.1 indicates that the flow through the rotor is divided by a series of aerodynamically independent streamtubes. In each streamtube, two actuator disks which refer to the upwind and downwind are placed in a tandem. For a tilting angle ϕ at the tower due to the pitch, the freestream velocity U can be divided into $U \cdot \sin \phi$ and $U \cdot \cos \phi$ which are parallel and normal to the tilting tower. Then, it can be equivalent to a non-tilting condition. Those induced velocities of upwind horizontal velocity U_u , upwind vertical velocity V_u , the equilibrium velocity U_e , and the downwind horizontal velocity U_d can be reformulated as the following.

$$U_u = U(\cos \phi - a_u)$$

$$V_u = U \sin \phi$$

$$U_e = U(\cos \phi - 2a_u)$$

$$U_d = U_e(1 - a_d) = U(\cos \phi - 2a_u)(1 - a_d)$$

The downwind vertical velocity is negligible if the tilting angle is small. The induced factor a_u and a_d at the upwind disk and downwind disk can be derived from a numerical solution which combines the Glauert momentum theory and the blade element theory.

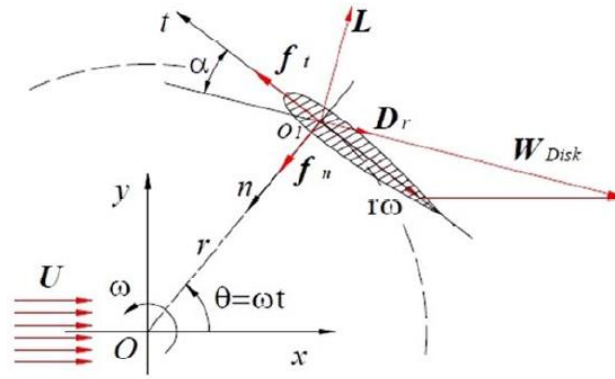


Figure 2.2. The relative velocity and force of the blade section in a horizontal view [38].

From the blade element theory, the lift force and the drag force are written in the formulas as below and depicted in Figure 2.2. The drag coefficient C_D and lift coefficient C_L are parallel and perpendicular to the relative wind direction. The drag and lift coefficients vary with the azimuthal angle and are also controlled by the blade shape and the Reynolds number.

$$L = C_L \cdot \frac{1}{2} \rho W_{Disk}^2 \cdot c$$

$$D_r = C_D \cdot \frac{1}{2} \rho W_{Disk}^2 \cdot c$$

The local relative wind velocity W_{Disk} should be treated separately at the upwind side W_u and the downwind side W_d , since the induced velocities are different as mentioned earlier. Then, the local upwind and downwind relative velocity can be found by the sum of tangential velocity due to the rotation, the induced velocity, and the tilting effect. The local angle of attack α can be derived from the basic trigonometry.

In order to find the torque of the rotor, the power performance and the influence of dynamic stall correction, the drag and lift coefficients can be projected into the tangential and normal direction to derive C_t and C_n . Similarly, the thrust force and lateral force can be calculated from the thrust force coefficient C_x and the lateral force coefficient C_y , which are the projection of tangential and normal force coefficient into x and y direction, respectively.

Furthermore, the accuracy of the aerodynamic model can be improved by including the dynamic stall effect. The dynamic stall usually occurs at a lower tip-speed ratio. As the

blade encounters a higher angle of attack, the originally attached flow would separate from its surface. In addition, a wake behind the blade in the upwind side may result in a lower wind speed in the downwind zone. To consider the dynamic stall effect, the Beddoes-Leishman Dynamic Stall (BL DS) model is applied to this study and combined with the improved DMS model.

The BL DS model consists of three components, which are unsteady attached flow, unsteady separated flow, and dynamic vortex lift. The normal force coefficient C_N^{Pot} under the attached flow condition can be regarded as the sum of the circulatory normal force coefficient C_N^C and the impulse normal force coefficient C_N^I . The chordwise force coefficient C_C , which is in the tangential direction, can be derived from the effective angle of attack α_e and shown in the equation below.

$$\begin{aligned} C_N^{Pot} &= C_N^C + C_N^I \\ C_C &= C_N^C \cdot \alpha_e \end{aligned}$$

In the unsteady separated flow condition, the leading-edge separation and trailing-edge separation are estimated. At the final stage, a vortex near the leading edge would detach from the blade at a certain point and then move to the downstream side. Overall, the total normal force coefficient and the chordwise coefficient force including the above three components are integrated with the previous force coefficients in DMS model. Thus, the total aerodynamic loads on the airfoil with the dynamic stall effect could be obtained. A more detailed description of the mathematical derivation can follow Wang et al. [38].

2.3. Hydrodynamic load

The hydrodynamic loads on a floating structure are computed through the combination of potential theory and the Morison's equation. The wave excitation force, the added mass, and damping of the system can be derived from a potential flow model. The drag force along the structure hull can be obtained through the Morison's equation. The second order wave drift force can be estimated by the Newman's approximation. The prominent theories of hydrodynamics are introduced as follows.

2.3.1 Potential flow theory

In hydrodynamics, the velocity potential is used to describe the velocity field as the variation with time and space. The potential function could be derived from the

combination of several equations, including conservation of mass, conservation of momentum and boundary condition. The continuity equation is one expression to represent the conservation of mass, which implies the net mass flow through a fluid element should be equal to zero and is displayed in the following.

$$\frac{D\rho}{Dt} + \rho \nabla \cdot \vec{U} = 0$$

where ρ is the density of water, t refers to time and \vec{U} is the velocity vector. For the incompressible fluid, the continuity equation can be simplified as follow. As an irrotational flow is assumed, the curl of the velocity vector is equal to zero. Then, a potential function is found to express the velocity, which is $\nabla \cdot \varphi = \vec{U}$. To satisfy the assumption of incompressible and irrotational flow, a Laplace differential equation of second order can be finally derived.

$$\nabla \cdot \vec{U} = 0 \text{ (incompressible)}$$

$$\nabla \times \vec{U} = 0 \text{ (irrotational)}$$

$$\nabla^2 \varphi = 0 \text{ (potential flow equation)}$$

Generally, four boundary conditions are applied to solve the velocity potential: (1) seabed condition: no water can flow through the seabed; (2) body surface condition: no water can flow through the surface of the floating body; (3) infinity condition: no disturbance of the incident wave; (4) free surface condition: the water particle at free surface will remain at the still water surface, and the pressure at surface is equal to atmospheric pressure. As a linear wave velocity profile is assumed, the velocity potential can be derived as follow.

$$\varphi(x, z, t) = \frac{\xi_0 g \cosh k(z + d)}{\omega \cosh(kd)} \cos(\omega t - kx) \text{ (Airy wave theory)}$$

The above equation is the well-known Airy theory. The velocity of the water particle can be found by taking the derivatives of the potential function in each degree of freedom, and then the acceleration can be easily derived. From the general expression of the Bernoulli equation, the dynamic pressure under the wave can be obtained through the product of water density and the derivative of the potential function in time.

$$u = \frac{\partial \varphi}{\partial x}$$

$$a = \frac{\partial u}{\partial t}$$

$$P_d = -\rho \frac{\partial \phi}{\partial t}$$

The real sea state physically consists of irregular waves with random heights and periods, but it can be usually relevant to a combination of a series of sinusoidal waves. The wave-induced responses and the loads on a floating structure can be dealt with the superposition of the regular wave components and compose of two conditions: (a) a restrained floating body encounters the regular incoming waves; (b) a freely floating body is forced to oscillate with the wave excitation frequency [39].

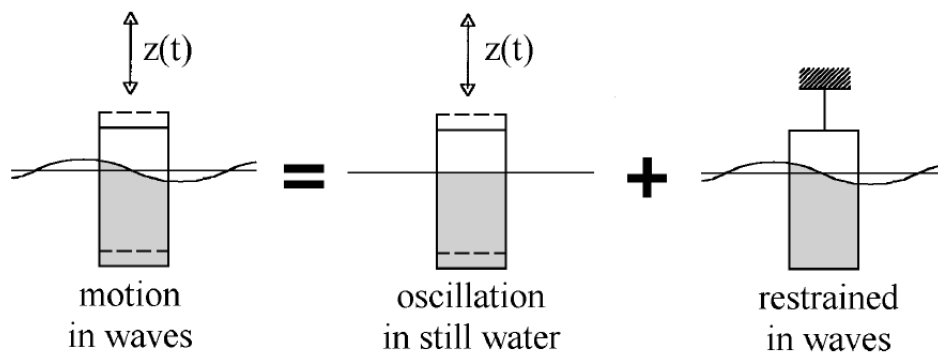


Figure 2.3. The superposition of hydrodynamic loads on a floating structure [40].

The hydrodynamic loads in the first condition of the restrained body are also called the wave excitation loads, which can be regarded as the combination of Froude-Kriloff force and the diffraction force and moment. The Froude-Kriloff force can be described from the unsteady pressure caused by the undisturbed waves, which is the integration of the pressure on the wet surface of the floating body and shown as follow. The diffraction force and moment result from the disturbance of the floating body in the pressure field, which could be obtained through the added mass and damping coefficients. The total wave excitation force on the floating body is non-viscous due to the derivation from the potential theory. For the consideration of the viscous effect, the Morison's equation is applicable and introduced in Section 2.3.2.

$$F_i = - \iint_S p \cdot n_i ds$$

The hydrodynamic loads in the second condition of a freely floating body are composed of the terms of added mass, damping and the restoring force and moments. The harmonic oscillations of a floating body will lead to the outgoing waves and the dynamic pressure on its surface. On the wet surface of the floating body, the motion of the water particle is assumed to be equal to forced body motion. The integration of the

pressure through the surface of the floating body can find the resultant force and moments including the added mass and damping terms. The contribution of added mass and damping loads are expressed as follows.

$$F_k = -A_{kj} \frac{d^2 n_j}{dt^2} - B_{kj} \frac{dn_j}{dt}$$

where A_{kj} and B_{kj} are respectively the added mass and damping coefficients, which denotes the motion j of the floating body with respect to the specified direction of k . In addition, the restoring force and moment of a freely floating body are controlled by the hydrostatic properties, which is expressed as follows.

$$F_k = -C_{kj} n_j$$

C_{kj} is the restoring stiffness of the body motion j on the specified direction of k . For a symmetric moored structure, the restoring coefficient will be dominated by the water plane area in heave and restrained by the submerged volume and metacentric height in roll/pitch. The effect of the spread mooring system in surge, sway and yaw should also be considered.

2.3.2 Application of Morison's equation

In the case of a submerged cylinder in a wave, a total force acting on a unit length of the cylinder can be formulated by Morison's equation. Several requirements need to achieve in advance: the water particle acceleration does change much over the diameter of the cylinder ($D/L < 0.2$); The amplitude a , the motion of the cylinder should not be too big ($a/D < 0.2$); It should be non-breaking waves ($H/L < 0.14$). Basically, Morison's equation is based on experiments and is given by:

$$f(z, t) = f_M + f_D = \frac{\pi D^2}{4} \rho C_M \dot{u} + \frac{1}{2} \rho C_D D u |u|$$

where D is the diameter of the cylinder; ρ is the fluid density; C_M is the mass coefficient; C_D is the drag coefficient; u is the horizontal particle velocity; \dot{u} is the horizontal particle acceleration. Then the total force is the sum of the mass force and the drag force, and it can be integrated over the previous equation:

$$F(t) = \int_{-d}^{surface} f(z, t) dz = \int_{-d}^{\xi} f_M(z, t) dz + \int_{-d}^{\xi} f_D(z, t) dz$$

In a case of a horizontal motion of the cylinder, the application of the Morison's equation needs some modifications. The modified Morison's equation on the horizontal hydrodynamic force per unit length is reformulated as follow. Here u_b and \dot{u}_b are respectively the horizontal velocity and acceleration of the moving cylinder.

$$f(z, t) = \frac{\pi D^2}{4} \rho \dot{u} + \frac{\pi D^2}{4} \rho C_M (\dot{u} - \dot{u}_b) + \frac{1}{2} \rho C_D D (u - u_b) |u - u_b|$$

For a large volume submerged structure, the Morison's equation is also applicable to find the viscous force. However, only the quadratic drag term in the above equation needs to be considered. In this study, the spar structure is modeled with slender elements in SIMO to calculate the drag force along the submerged part. The critical parameter, drag coefficient (C_D), can follow the recommendations from DNV-RV-C205 [41].

2.4. Stability of floating structure

This section addresses the hydrostatic properties of a floating structure. Initial stability is an important index to judge the stable condition of the floating body, which is defined as the resistance to a small deviation of tilting angle in a vertical direction. Station keeping is utilized to maintain the floating structure in a proper position, which is usually categorized into dynamic positioning and mooring. The basic theory of the initial stability and mooring are presented as follows.

2.4.1 Initial stability

The requirement of the static equilibrium for a floating structure should satisfy at least one criteria: the amplitude of the gravity and buoyancy force should be equal, and the directions of forces are opposite in line as shown in Figure 2.4. The buoyancy force can be found through Archimedes' principle. Center of buoyancy (COB) of the body is the point that the fluid pressure acting across the submerged surface is simplified as a resultant force acting at a single point. The COB of a body locates on the center of mass of the displaced fluid.

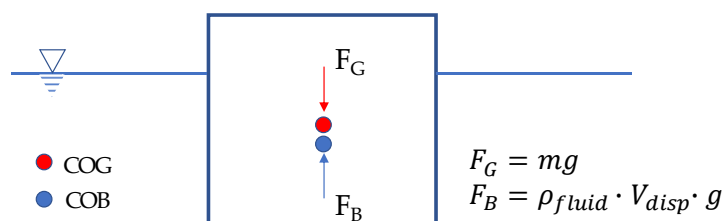


Figure 2.4. The gravity and buoyancy force in a submerged body.

The initial stability of a floating body represents that the inherent ability of the body to resist the overturning loads and return to the initial state after the applied loads are removed. The principal can be referred to the stability of barge which is shown in the Figure 2.5.

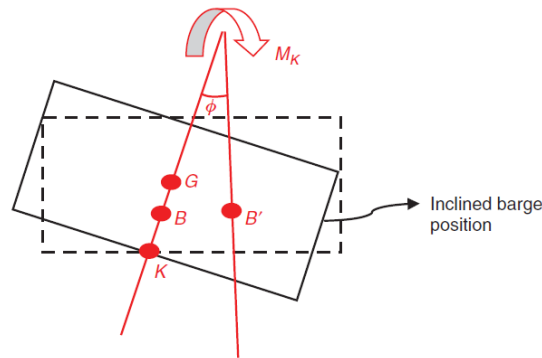


Figure 2.5. An illustration for the inclined barge position [42]

where B is the original position of the center of buoyancy; G is the center of gravity; ϕ is the angle of inclination; B' is the center of buoyancy in inclination mode; K is the keel; M_K is the moment causing the inclination.

From geometry, the metacenter height is given as [42]:

$$\overline{GM} = \overline{KB} + \overline{BM} - \overline{KG}$$

Here \overline{GM} is metacenter height, and it will increase as \overline{KG} decreases; \overline{BM} is metacenter radius, which is the ratio between moment of inertia and the submerged volume (I/V); \overline{KG} is the distance between the center of gravity and keel; \overline{KB} is the distance between the center of buoyancy and keel, which depends on the shape of the submerged part.

The application of \overline{GM} could be the criteria to evaluate the stability of the floating body: (a) $\overline{GM} > 0$: initial stability; (b) $\overline{GM} = 0$: indifferent equilibrium; (c) $\overline{GM} < 0$: unstable condition.

2.4.2 Mooring system

Mooring system makes use of mooring lines to maintain the position of a floating structure at sea relative to a fixed position in the seabed. The catenary mooring system

and taut mooring system are the two groups of the mooring system. In this study, the catenary mooring system is applied to the spar structure which can provide the restriction in sway, surge, and yaw direction.

For a free hanging chain catenary, the shape of the mooring line is affected by its self-weight effect. A typical layout of a catenary mooring line is illustrated in the figure below. The formula of the geometry for the mooring can be formulated as follows [42]:

$$y = \frac{H}{W} \left(\cosh \frac{W}{H} x - 1 \right)$$

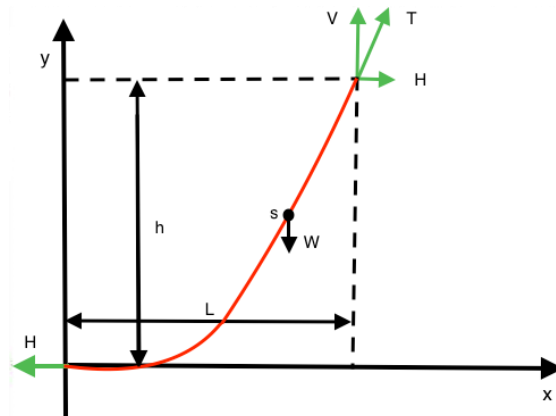


Figure 2.6. The catenary mooring layout [42]

The relevant forces and distance to the mooring configuration can be derived from the following equations [42]. Here T is tension in mooring line; V is vertical component of the tension; H is horizontal component of the tension; S is length of the chain to seafloor; L is length from the point where the tension is applied to the seafloor; h is water depth; W is submerged weight per unit length of the hanging chain.

- Length of catenary:

$$S = \frac{H}{W} \left(\sinh \frac{W}{H} L \right)$$

- Water depth:

$$h = \frac{H}{W} \left(\cosh \frac{W}{H} L - 1 \right)$$

- Horizontal force:

$$H = \frac{W}{2h}(S^2 - h^2)$$

- Distance to touchdown point:

$$L = \frac{H}{W} \cosh^{-1} \left(\frac{W}{H} h + 1 \right)$$

- Vertical force:

$$V = W \times S$$

- Tension:

$$T = \sqrt{H^2 + (WS)^2}$$

2.5. Integrated dynamic analysis of a floating VAWT system

The aero-hydro-servo-elastic is an integrated numerical tool for executing dynamic analysis of a floating wind turbine system in time domain. The SIMO-RIFLEX-DMS code, which was developed by NTNU and SINTEF OCEAN, is one of the fully coupled analysis tools for the floating VAWT and incorporates the wind flow simulation, aerodynamics, hydrodynamics, structural dynamic, control system and mooring system. Generally, the basic motion equation of a floating structure due to the wind and wave effect can be formulated as follows.

$$(M + A_\infty)\ddot{x}(t) + \int_{-\infty}^{\infty} \kappa(t - \tau)\dot{x}(\tau)d\tau + (K_m(x, t) + K_h)x(t) = F_{exc}(x, \dot{x}, t)$$

where $x(t)$, $\dot{x}(t)$, and $\ddot{x}(t)$ represent the displacement, velocity, and acceleration of the floating structure, respectively; M is mass matrix of the system and A_∞ is the added mass at infinite frequencies; $\kappa(t - \tau)$ is the retardation function and derived from the transform of frequency-dependent added mass and damping, thus it also implies the fluid memory effect; K_m is the nonlinear restoring matrix of the mooring system, and K_h is the hydrostatic restoring matrix of the floating structure. In principle, the left terms in the above equation represent the dynamic motion of the floater, and the right term F_{exc} accounts for the excitation forces acting on the system.

$$F_{exc}(x, \dot{x}, t) = F^{Aero}(x, \dot{x}, t) + F^{FK}(t) + F^D(t) + F^{Drag}(\dot{x}, t)$$

The excitation forces mainly include the following terms: F^{Aero} is the aerodynamic force, which is calculated from the DMS model in this study; F^{FK} and F^D are the Froude-Kriloff force and the diffraction force, respectively, which have been mentioned in section 2.3.1; F^{Drag} is the viscous force, and Morison's equation is used to estimate the viscous drag force on the structure hull.

In a numerical model of the floating VAWT system, the blade is modeled as a beam element, which has two symmetric planes to emphasize different properties in flap-wise and edge-wise direction. The tower and shaft are considered as beam elements with axisymmetric cross sections. The mooring lines are modeled as bar elements. The platform is assumed as a rigid body, and master/slave nodes provide a link between the platform and tower/ fairlead. The control system accounts for an electric torque installed on a flexible joint and aims to control the rotating speed. The integrated dynamic motions of the whole system are solved by the nonlinear finite element method (FEM) at each time step. The general motion equation of the whole system can be simplified into the following expression [15]. where M_g , B_g , and K_g are respectively global mass, damping and stiffness matrices; The damping term is modeled as the Rayleigh damping in this study; $r(t)$, $\dot{r}(t)$, and $\ddot{r}(t)$ represent the displacement, velocity and acceleration vectors of the whole system, respectively. A detailed explanation of the SIMO-RIFLEX-DMS code and the relation of each module are presented in Section 3.3.

$$M_g \ddot{r}(t) + B_g \dot{r}(t) + K_g r(t) = R^E(r, \dot{r}, t)$$

In addition, a proportional-integral (PI) generator control, which was developed by Merz and Svendsen [43], is a control strategy of the external controller for the VAWT. This control system aims to regulate the generator torque and rotational speed within the operational range. An approximately constant rotational speed is expected to maintain as the rated rotational speed is achieved. The basic idea of the control algorithm is to minimize the difference between the measured rotational speed Ω_{mes} and the reference rotational speed Ω_{ref} . Then, the required electrical torque $T(t)$ can be derived from the error of rotational speed $\Delta\Omega$. where K_G is the generator stiffness; K_P and K_I are proportional and integral gains, respectively.

$$\Delta\Omega = \Omega_{mes} - \Omega_{ref}$$

$$T(t) = K_G \left(K_P \Delta\Omega(t) + K_I \int_0^t \Delta\Omega(\tau) d\tau \right)$$

However, the generator power may increase with the rise of wind speed even it is above the rated speed. This phenomenon may cause a larger aerodynamic load and arouse the potential instability of the system. An improved PI control system, which was proposed by Cheng et al [44], is then adopted in this study. The principle of the improved strategy is to maximize the power production as the wind speed is below rated speed, but it should keep an approximately constant power generation for the above-rated speed condition. An illustration of this strategy is shown in the figure below [45].

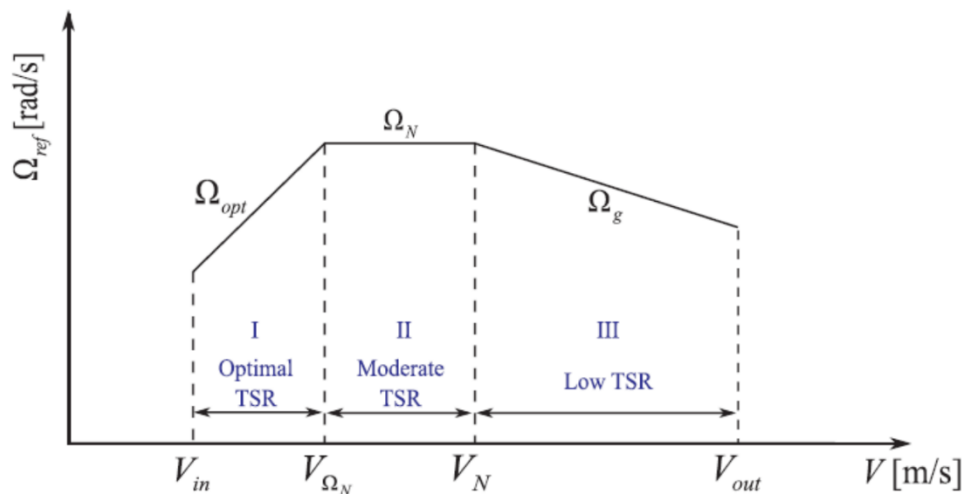


Figure 2.7. The relationship between the rotor rotational speed and the wind speed for an improved control system [45]. Here V_{in} , V_N , and V_{out} are cut-in, rated, and cut-out wind speed, respectively; V_{Ω_N} is the wind speed with respect to the rated rotational speed; Ω_{opt} is the optimal rotational speed to produce maximal power; Ω_N is the rated rotational speed; Ω_g is the rotational speed to maintain an approximately constant generator power.

3. FLOATING WIND TURBINE CONCEPTS

Firstly, a short spar and a deep spar VAWTs will be introduced in this section. The Spar-Torus combination vertical axis wind turbine will be demonstrated in the second part. SIMO-RIFLEX-DMS code is used to carry out a fully coupled aero-hydro-servo-elastic analysis in this thesis. All the detailed procedure, initial settings, and environmental conditions will be presented in the following sections.

3.1. Deep spar and short spar VAWTs concepts

A comparison of dynamic responses between the deep spar VAWT and short spar VAWT is studied in the first part of the thesis. The schematic layouts of the deep spar and short spar model are shown in Figure 3.1. A Darrieus 5 MW wind turbine is used for both models, and its specifications are listed in Table 3.1. The deep spar VAWT is a feasible concept of a catenary moored spar-type VAWT which was introduced by Cheng et al. [33]. The model of the short spar VAWT mainly follows the concept of the spar HAWT from Karimirad and Moan [7, 8], but most of the details have been modified. The floater of the short spar VAWT consists of two different parts of cylinders, and heavy ballast is placed on the bottom. The dimension of the short spar and configuration of the ballast are determined through the following criteria: (a) the water depth; (b) the static equilibrium of the self-weight, buoyancy force, and the tension of mooring; and (c) the typical requirement of the initial stability. The detailed stability check and configuration of the short spar are shown in Appendix B.

Table 3.2 lists the properties of the deep spar and short spar VAWTs. In principle, the water depth could limit the application of the spar in shallow water conditions. At a moderate water depth, the draft needs to be reduced so that it can achieve an adequate design. The short spar model shows that its depth is reduced to 80m, but the diameter is increased to maintain the relevant displacement and buoyancy with the deep spar. The total mass (structural and ballast) of the short spar is 1.1% heavier than that of the deep spar. The variation of the depth of the short spar leads to a smaller mass moment of inertia in the roll and pitch directions, but the wider diameter causes a larger mass momentum in the yaw direction.

Table 3.1. Specifications of the Darrieus 5 MW wind turbine [33]

Item	Unit	Value
Rated power	[MW]	5
Rotor height, root to root	[m]	129.56
Rotor radius	[m]	63.74
Chord length	[m]	7.45
Airfoil section	[-]	NACA 0018
Cut-in, rated, cut-out wind speed	[m/s]	5, 14, 25
Rated rotational speed	[rpm]	5.26
Total mass, incl. rotor and tower	[kg]	754226
Center of mass	[m]	(0,0,75.6)

Table 3.2. Properties of the deep spar and short spar

Item	Unit	Deep spar	Short spar
Water depth	[m]	320	150
Draft	[m]	120	80
Waterline diameter	[m]	6.5	9
Diameter at bottom	[m]	9.4	12
Hull mass, including ballast and generator	[ton]	7308.3	7962.8
COM location below MSL ¹	[m]	-89.76	-62.86
COG location below MSL ²	[m]	-74.29	-50.88
Displacement	[m ³]	8027	8642
COB location below MSL ³	[m]	-62.06	-41.68
Mass moment of inertia in roll and pitch, I_{XX} and I_{YY}	[ton·m ²]	6.362×10^7	3.599×10^7
Mass moment of inertia in yaw, I_{ZZ}	[ton·m ²]	1.588×10^5	1.889×10^5

Note:

(1) Center of Mass (COM) of floater only includes spar, ballast, and generator.

(2) Center of Gravity (COG) of floater includes turbine, rotor, tower and spar(ballast).

(3) COB represents the center of buoyancy; MSL refers to the mean seawater level.

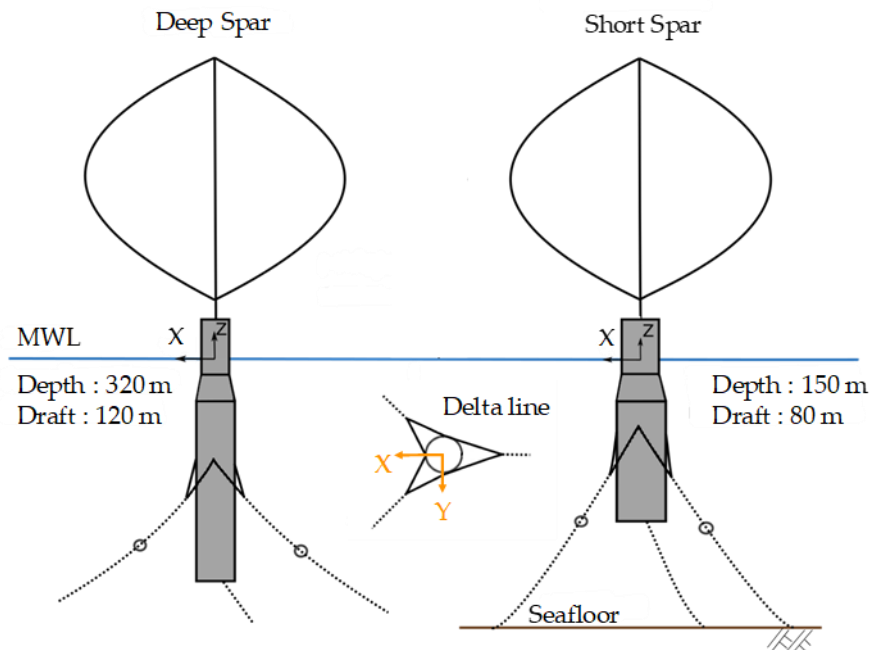


Figure 3.1. The diagram of the deep spar and short spar vertical-axis wind turbines (VAWTs) in deep and moderate water. Here MWL refers to mean water level.

The spread mooring system includes three sets of mooring lines connected with the fairlead position of the spar structure. Each mooring line has four segments which are the two delta lines, upper line, clump mass, and lower line. The delta lines can provide yaw stiffness. The water depth will govern the total length of the mooring lines. Generally, the stiffness of the mooring line in moderate water depth is stronger than that in deep water. The properties of the mooring components follow Cheng et al. [33], and the length of the mooring line in the short spar is shortened to find a sufficient design for moderate water depth. Figure 3.2 illustrates the layout of the mooring system for both the deep spar and short spar VAWTs. The properties of each component in the mooring system for both spar models are listed in Table 3.3.

Table 3.3. The properties of mooring system components

Type	Component	Length [m]	Mass[kg/m]	Axial stiffness[kN]
Deep Spar	Delta line	50	42.5	200,000
	Upper line	250	42.5	80,000
	Clump mass	2	17,253	80,000
	Lower line	600	42.5	60,000
Short Spar	Delta line	50	42.5	200,000
	Upper line	125	42.5	80,000
	Clump mass	2	17,253	80,000
	Lower line	250	42.5	60,000

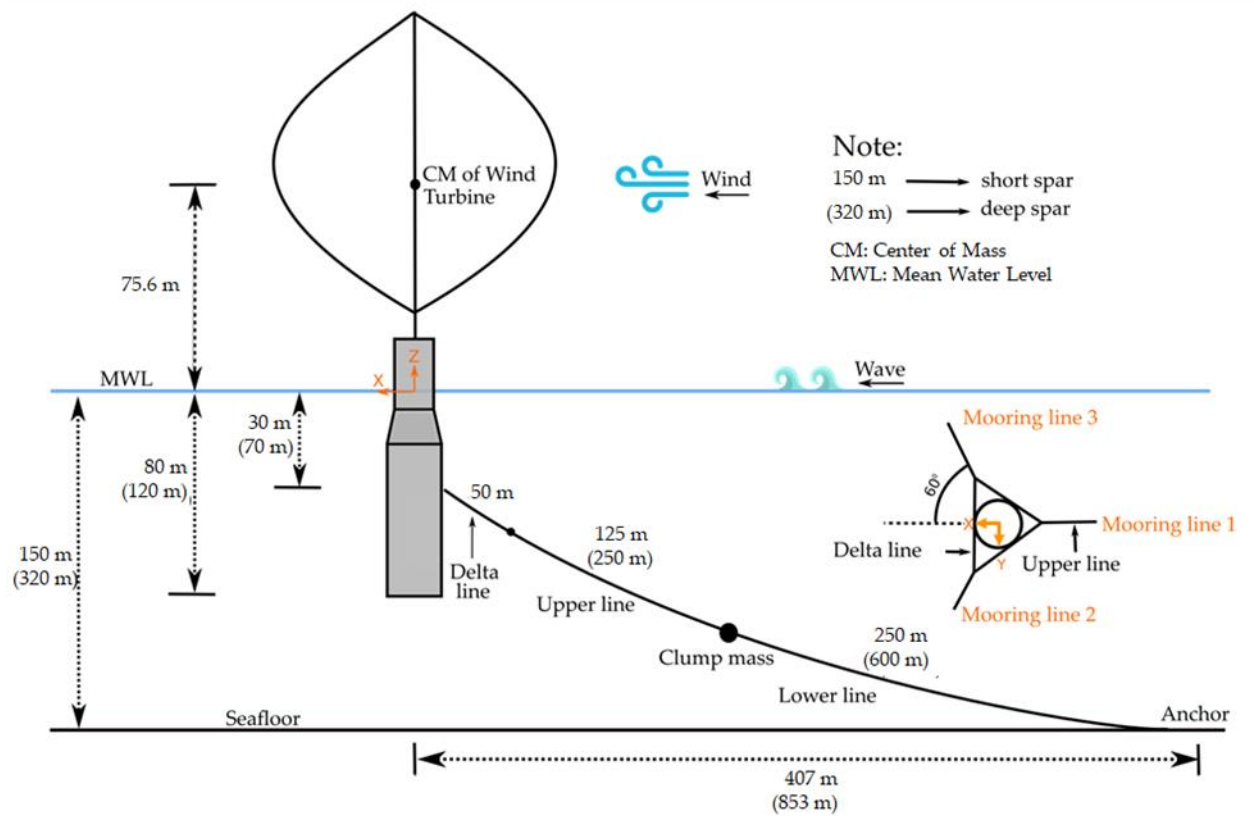


Figure 3.2. The diagram of the mooring system for the short spar and deep spar VAWTs.

3.2. Spar-Torus Combination concept

The Spar-Torus Combination(STC) VAWT model is basically inspired by the concept of STC HAWT from Muliawan et al. [27], which combines a spar-type floating wind turbine and a torus-shaped wave energy converter. This novel concept consists of a vertical axis wind turbine, torus, spar structure and mooring system. The torus and spar structure are two concentric floaters but move with different phase angle in heave direction. The conceptual sketch is shown in Figure 3.3, and its detailed configuration is displayed in Figure 3.4. A Darrieus 5MW wind turbine is adopted in this model, and a 320m water depth is considered in the second part of the study. The main character in this concept is that not only the spar vertical axis wind turbine could extract the wind energy, but also the torus could absorb the wave energy by sliding along the spar structure in a relative heave motion. The detailed components and mechanisms for this concept are introduced in the following sections.

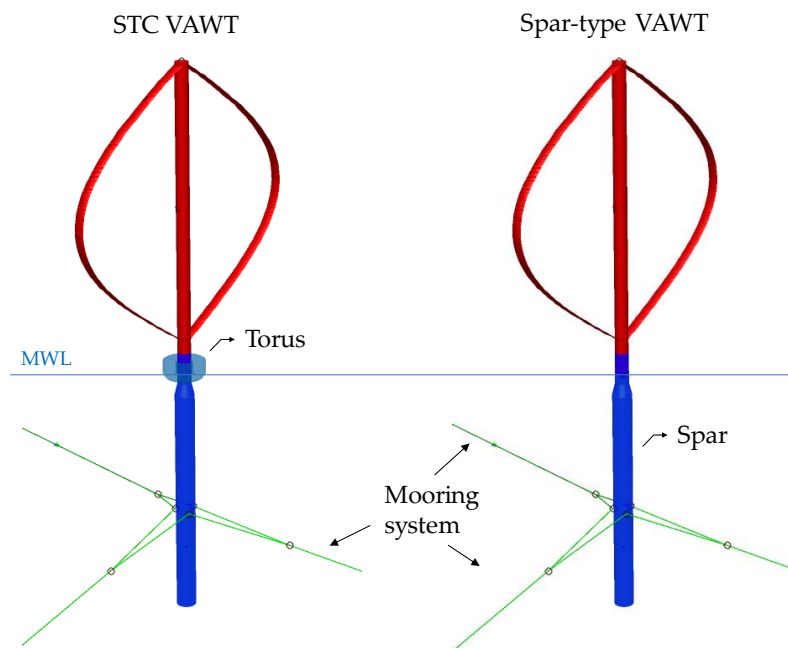


Figure 3.3. The illustration of the Spar-Torus Combination(STC) VAWT concept and the spar-type VAWT concept.

3.2.1 Torus

The torus is a ring shape and axisymmetric buoy, which floats on the sea surface. Due to the wave propagation, the torus slides in a relative heave motion with the spar structure to extract the wave energy. A fixed ballast system is assigned to the interior of

the torus for the operational conditions in this study. The properties of the torus structure are listed in Table 3.4. These parameters mainly follow the geometry and dimensions of the feasible STC concept from Muliawan et al. [27, 31]; hence, no detailed verifications or engineering calculations will be discussed here.

Table 3.4. Properties of the torus in the STC concept [31]

Item	Unit	Value	Remark
Outer diameter	[m]	20	
Inner diameter	[m]	8	
Draft	[m]	2	
Height	[m]	8	
Displacement	[m ³]	408	
Mass	[ton]	418	
COM location below MSL	[m]	-0.9	
Mass moment of inertia, I_{xx}, I_{yy}	[ton·m ²]	1.076×10^4	In roll and pitch
Mass moment of inertia, I_{zz}	[ton·m ²]	2.056×10^4	In yaw

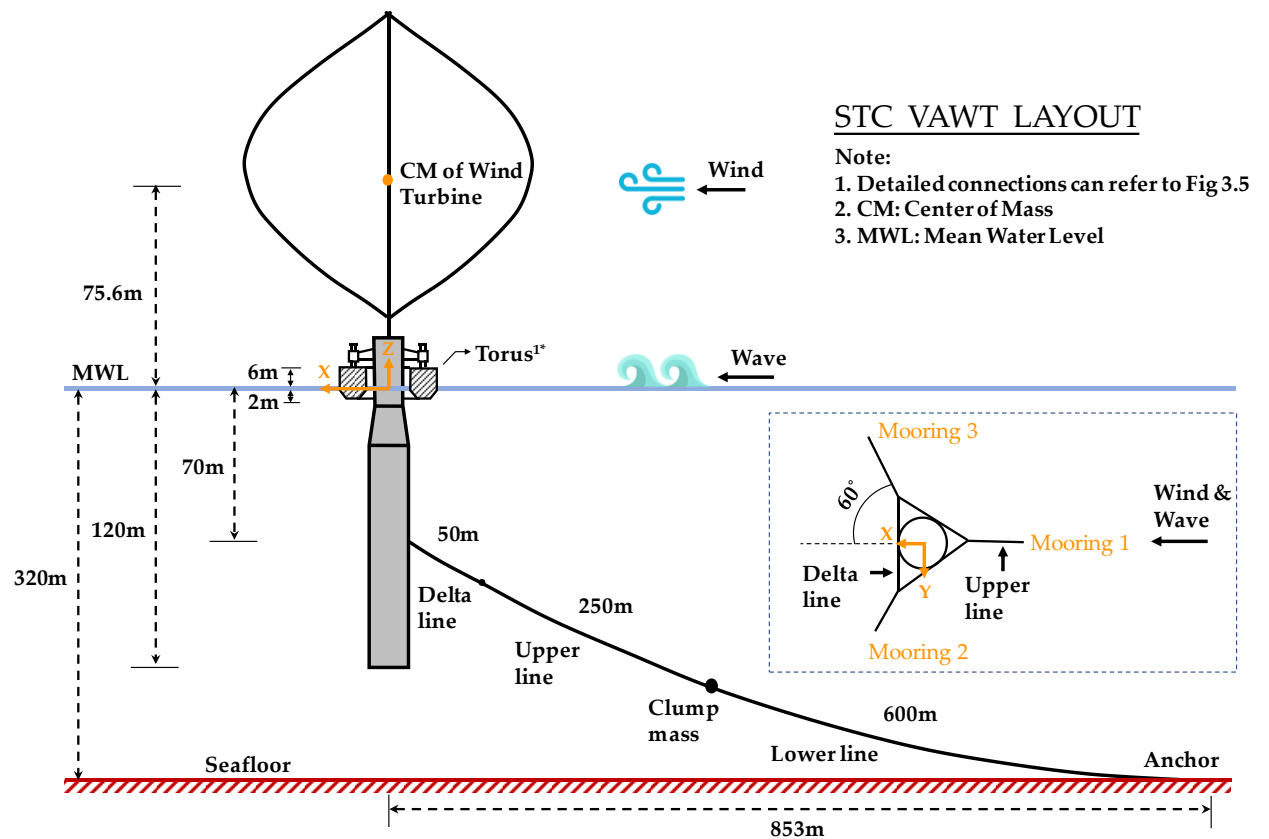


Figure 3.4. The illustration of the mooring system for the STC VAWT concept (not on scale).

3.2.2 Spar VAWT

The spar VAWT is a catenary moored spar structure carrying a two-bladed Darrieus 5MW rotor. Basically, the spar VAWT in the STC concept follows the identical structure configuration with the deep spar VAWT, which was introduced by Cheng et al. [33] and presented in Section 3.1. The properties of the Darrieus 5MW rotor, spar structure, and the mooring systems can refer to Tables 3.1, 3.2 and 3.3, respectively. The whole conceptual layout including the torus and the spar VAWT can be seen in Figure 3.4.

3.2.3 Coupled connections between Torus and Spar VAWT

The coupled connections between the torus and spar structure include three critical components, which are bearing system, end stop system, and power take-off system. The detailed explanation of the mechanical structure can be referred to Muliawan et al. [27]. The bearing system mainly controls the relative motion and transfers the coupled forces between the torus and the spar structure. The torus is on wheels at each side and different elevations so that it can slide freely along the surface of spar structure in heave direction. The rest of degrees of freedom in motions between these two floaters are constrained by the bearing system, which forces them to move together. The sketch of the bearing system is illustrated in Figure 3.5(a).

The end stop system restricts the relative motion in heave between the torus and the spar structure. It is a protective mechanism to avoid too large heave motion in a hazardous sea state. Two end stop springs are installed separately on the upper and lower locations of the system. The relative end stop distance is determined from the coupled force between these two floaters, and a +/- 3m distance is assigned in this study under operational conditions based on Muliawan's recommendation [27]. The properties of the end stop springs are listed in Table 3.5, and the sketch of the end stop system is shown in Figure 3.5(b).

The power take-off system (PTO) is the key component of the wave energy converter (WEC), which absorbs the wave energy through the relative heave motion between the torus and the spar. It is essentially a hydraulic cylinder which connects the torus and the spar structure. When the wave drags the torus to slide along the spar, the relative heave motion forces the piston to move back and forth. These inside pressurized fluids will drive the generator to convert to power. The power take-off system is simplified as a linear damping and linear spring in the STC model of this study. The properties of the power take-off system are listed in Table 3.5. The conceptual idea of the power take-off system is shown in Figure 3.5(c).

Table 3.5. Properties of the coupled connections between the torus and the spar [30, 31]

Item	Unit	Value
Stiffness upper end stop spring	[kN/m]	10^6
Stiffness lower end stop spring	[kN/m]	10^6
PTO damper	[kN·s/m]	8000
PTO stiffness	[kN/m]	10

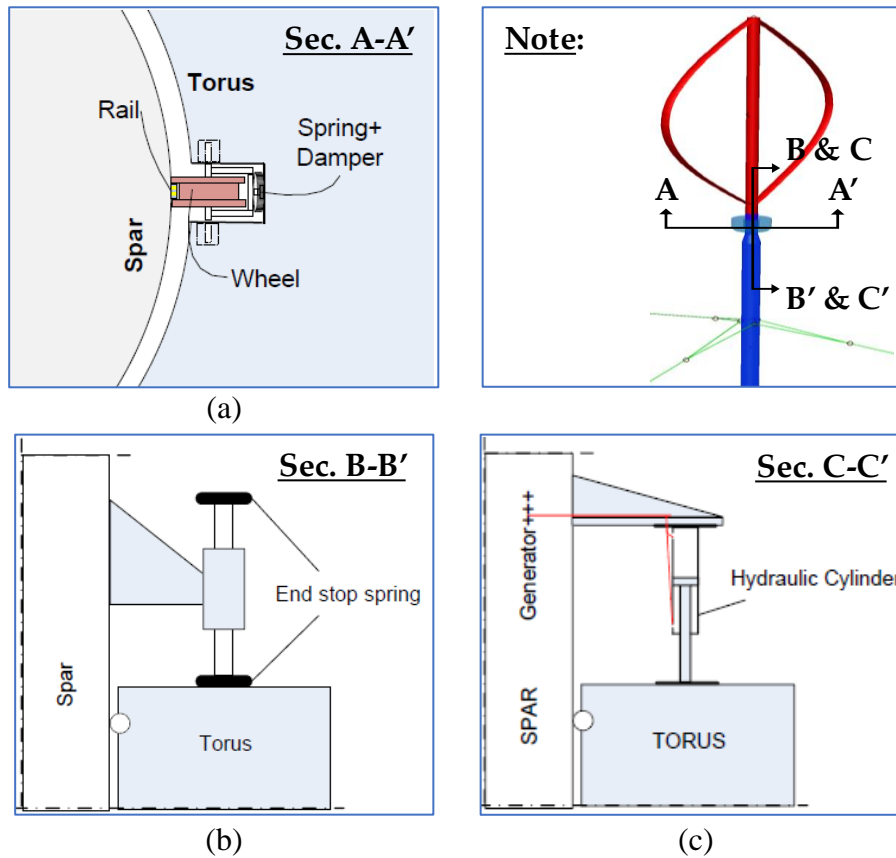


Figure 3.5. The coupled connection between the torus and the spar: (a) Bearing system; (b) End stop system; (c) Power take-off system [27].

3.3. Numerical modeling for floating VAWTs

A fully coupled simulation tool (SIMO-RIFLEX-DMS) was adopted for dynamic analysis in the time domain of both the spar-type VAWTs and Spar-Torus Combination VAWT. The flowchart is shown in Figure 3.6 [14]. SIMO calculates the hydrodynamic loads on the floating structure; DMS computes the aerodynamic loads on the blades according to the improved Double-Multiple Streamtube model; RIFLEX is a nonlinear finite element solver for estimating dynamic structural responses, and also provides links to the DMS code and an external controller. The external controller is a proportional–integral-based generator torque controller written in Java. The controller used by Cheng [15] was utilized in this study. The strategy of the controller involves maximizing the power capture for the wind speed below the rated speed and maintaining approximately constant power production for the wind speed above the rated speed. Verification of this aero-hydro-servo-elastic simulation tool (SIMO-RIFLEX-DMS) has been conducted through a series of code-to-code comparisons (HAWC2, SIMO-RIFLEX-AC) and model-to-model comparisons from Wang [46] and Cheng [44]. The detailed setting of each step with the short spar VAWT and Spar-Torus Combination VAWT will be presented in the following sections, and the model of the deep spar VAWT can refer to Cheng et al. [33].

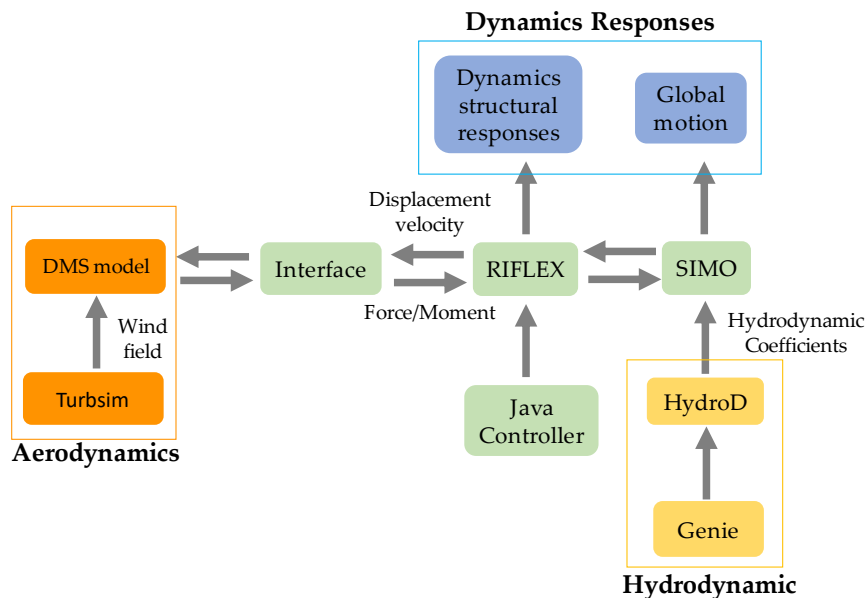


Figure 3.6. Computation flowchart for the coupled model (reproduced from Wang [14]).

3.3.1 HydroD model

The hydrodynamic properties, wave loads, and motion response of the floating structure can be derived from HydroD software. The WADAM (Wave Analysis by Diffraction

and Morison Theory), one of the modules in HydroD, was adopted to obtain kinetic parameters in the frequency domain including hydrostatic data, first-order wave force transfer function, retardation function, second-order wave drift force, etc. The outputs of HydroD were imported into the SIMO model. The main procedures of short spar VAWT and Spar-Torus Combination VAWT are presented as follows.

3.3.1.1 Short spar VAWT

A panel model is selected to calculate the hydrostatic and hydrodynamic forces from potential theory for the body of the short spar. The basic part of a panel model consists of the quadrilateral or triangular panels representing the wet surfaces of a body. The wet surface of a panel model is identified by defining a dummy load on the panel model in GeniE, which is another DNV GL software for modeling a structure. In our case, a mesh fineness of 1m long squares for the spar structure is generated from GeniE and shown in Figure 3.7.

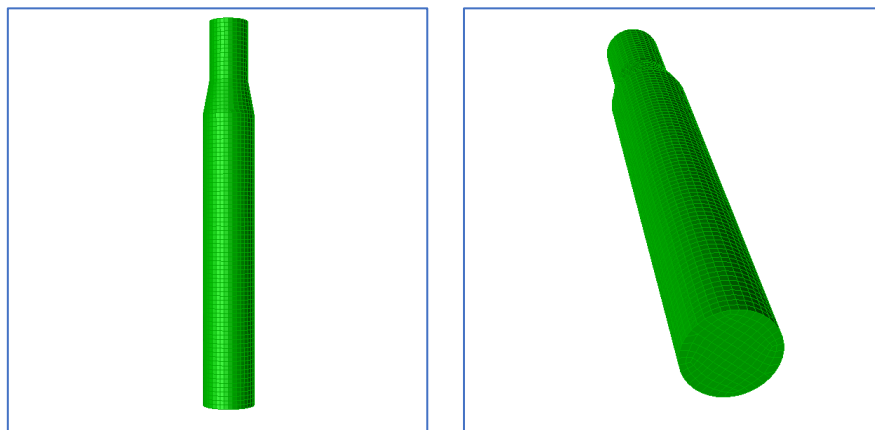


Figure 3.7. A mesh illustration for the short spar model in Genie.

The water depth is defined to 150 meters in this short spar model and four wave directions are used to simulate the frequency domain analysis which is set to 0, 30, 60 and 90 degrees. Since the spar structure is axisymmetric, the rest of angles (90 to 360 degrees) in wave direction will have the identical results with the initial setting. Additionally, the frequency is set to perform frequency domain analysis. The number of frequency should be enough to ensure the accuracy of the simulation results. 39 wave frequencies are assigned to the simulation which starts from 0.134 to 5.026 rad/s.

“Center of gravity centered system” is specified in the input coordinate system. The total mass of the short spar structure which includes the weight of spar, ballast and wind turbine should be assigned. The coordinate of COG and radius of gyration are set into

this mass model. The value of total mass, COG, and radius of gyration are summarized in the table below.

Table 3.6. Key parameters of the mass model in the short spar VAWT

Parameter	Value	
Total mass, M [Kg]		8717032
COG coordinate [m]	X:	0
	Y:	0
	Z:	-50.88
	RX:	25.49
Radius of gyration [m]	RY:	25.49
	RZ:	4.65

Note: $RX = \sqrt{I_{XX}/M}$

In the WADAM setting, a single body will be selected. The loading condition is set to the water surface at $z=0$. For the drift forces in executive directives, the far field integration will be used to calculate the second order wave drift coefficients in surge, sway and yaw direction (three horizontal degrees of freedom). The short spar model in HydroD is shown in the figure below.

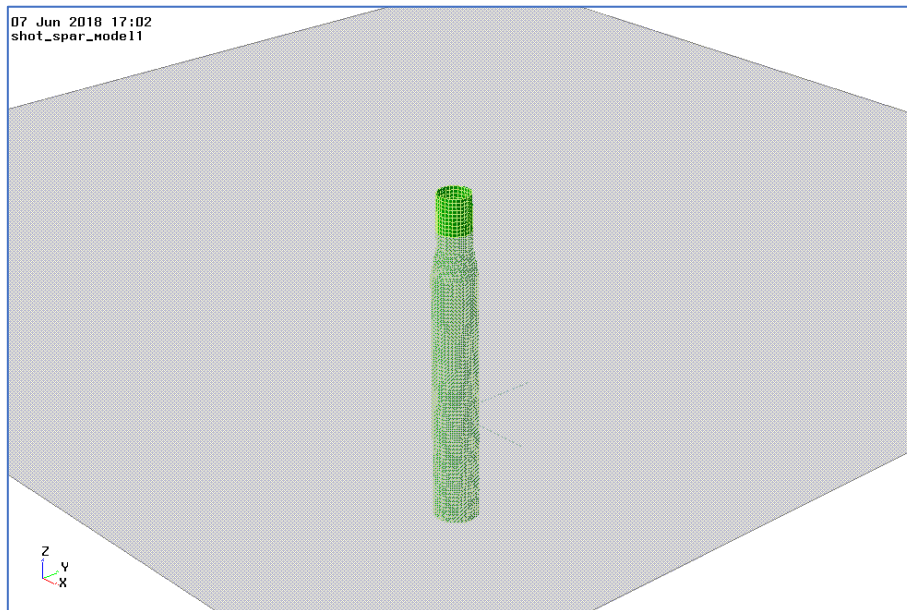


Figure 3.8. The illustration of the short spar in HydroD

3.3.1.2 Spar-Torus Combination VAWT

A multi-body analysis in WADAM is used to model the hydrodynamic interaction between the torus and the spar for the STC concept. Similarly, the structural models of the torus and the spar were built separately from GeniE in advance. The wet surfaces were assigned to the area of these two bodies, which is exposed to seawater. The mesh density was set to 1m element length to create finite element mesh in both models. Two FEM models of the spar (T1.FEM) and the torus (T2.FEM) were exported from GeniE individually. The generated mesh in the torus and spar model are shown in Figure 3.9.

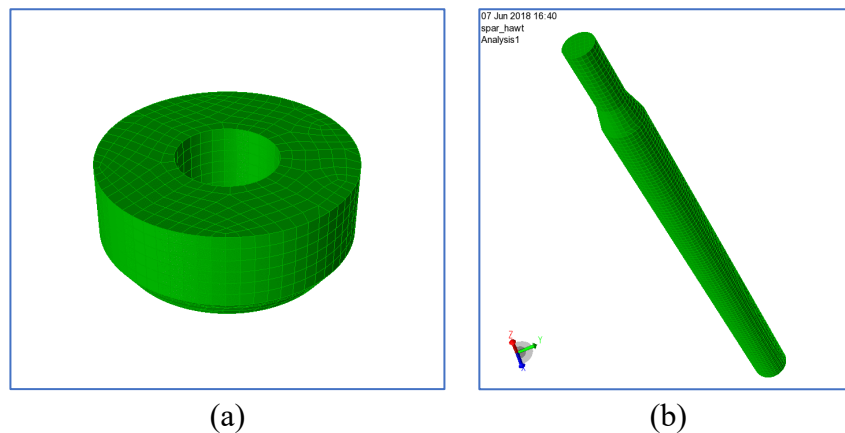


Figure 3.9. Mesh illustrations for the spar and torus in Genie: (a) Torus; (b) Spar.

The water depth is 320m in this HydroD model. Four sets of wave direction between 0 to 90 degrees were defined, and a double symmetry was specified later in this model to include all directions of coming waves. Total 31 frequency sets were assigned to perform frequency domain analysis, which ranges from 0.02 to 5.02 rad/s. Since the STC concept consists of two large bodies, panel models were adopted to compute the hydrodynamic forces based on the potential theory for the torus and the spar. Some key parameters of the torus and the spar in the mass model are listed in Table 3.7, and the mass properties of the spar structure generally are identical with the deep spar concept [33].

Table 3.7. Key parameters of the mass model in the STC concept

Parameter		Torus	Spar
Total mass, M [Kg]		418000	8216000
COG coordinate [m]	X:	0	0
	Y:	0	0
	Z:	-0.9	-78.5
Radius of gyration [m]	RX:	5.07	92.19
	RY:	5.07	92.19
	RZ:	7.01	4.52

To simulate the hydrodynamic interactions due to the wave motions for the adjacent bodies, the torus and the spar are simultaneously considered in a multi-body model. Since the mechanical connections link the spar and the torus, a coupled stiffness matrix and a coupled damping matrix are defined in this analysis. The relative stiffness and damping values in each degree of freedom follow the recommendations from Muliawan et al. [27, 31], which has been introduced in Section 3.2.3. The water surface in the loading condition is specified at $z=0$. The wave drift forces using far-field integration method of the spar and torus could derive from the simulations of each single bodies. The panel models of the STC concept in HydroD are shown in Figure 3.10.

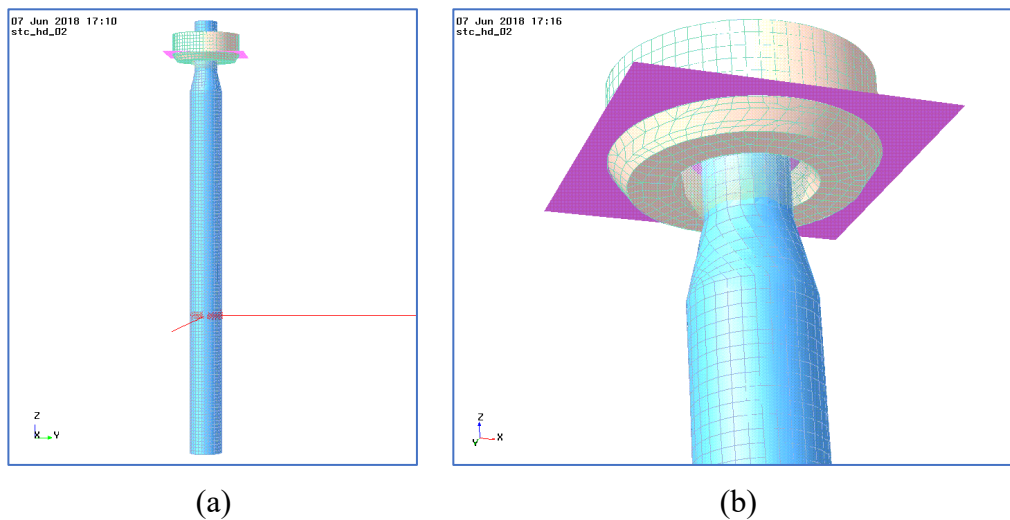


Figure 3.10. Panel models of the STC concept in HydroD: (a) Full view; (b) Zoom in the model.

3.3.2 SIMO model

SIMO is a computer program for calculating the hydrodynamic loads on a floating structure [47]. The floater is modeled with a rigid body in SIMO, and the hydrodynamic loads mainly include first-order wave loads, second-order wave drift loads, and viscous drag force. The first-order wave loads were derived from the linear potential flow model, and the second-order wave drift loads were estimated through Newman's approximation. The viscous drag forces were calculated from the viscous term of the Morison equation and quadratic drag force coefficient. The detailed description of the short spar VAWT and Spar-Torus Combination VAWT are demonstrated below.

3.3.2.1 Short spar VAWT

After importing the hydrodynamic properties from HydroD, some parameters in SIMO need to do some modifications. The main reason is that the result from HydroD includes the effects of the wind turbine; hence, it should be eliminated in this step to maintain the overall balance for the coupled simulation which shows in the following procedure.

First, the coordinate of the center of gravity, total mass, and mass of inertia for the short spar body in the system description file should be revised by deducting the weight of wind turbine from the initial total mass. The updated parameters are summarized in the table below.

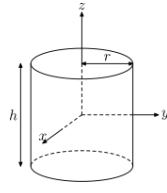
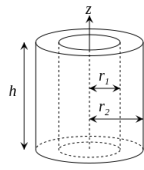
Table 3.8. The body mass data in the short spar model

Parameter	Value	
Total mass, M [ton]	7962.8	
COG coordinate [m]	X:	0
	Y:	0
	Z:	-62.86
Mass of inertia [ton*m ²]	I _{xx} :	3.59×10^7
	I _{yy} :	3.59×10^7
	I _{zz} :	1.89×10^7

Note:

1. Global coordinate system is specified in body data.
2. The ballast part is simulated with a solid cylinder for calculating the mass of inertia, and the spar is modeled with a thick wall tube (Table 3.9).
3. The original point (0,0,0) in SIMO should be the reference point for calculating the mass of inertia.

Table 3.9. Mass of moment inertia with each type of cylinder [48]

Type	Mass of inertia	Note
	$I_z = \frac{1}{2}mr^2$ $I_x = I_y = \frac{1}{4}mr^2 + \frac{1}{12}mh^2$	Ballast
	$I_z = \frac{1}{2}m(r_1^2 + r_2^2)$ $I_x = I_y = \frac{1}{4}m(r_1^2 + r_2^2) + \frac{1}{12}mh^2$	Spar

To estimate the drag force of the submerged spar, four slender elements are added in SIMO by using Morison equation. The quadratic drag force coefficients in the transverse direction should be set on the sides of the spar (parallel to the flow), and a quadratic term in the longitudinal direction is placed on the bottom of the spar to represent the drag effect in heave motion.

Table 3.10. Quadratic drag force coefficient in SIMO

No	z [m]	L [m]	V [m ³ /m]	D [m]	C _D [-]	C _{2x} [Ns ² /m ³]	C _{2y} /C _{2z} [Ns ² /m ³]
1	10~0-4	14	63.6	9	0.6	-	2767.5
2	-4~-12	8	87.2	10.5	0.6	-	3239.7
3	-12~-80	68	113.1	12	0.6	-	3690.0
4	-80~-81	1	-	12	1.9	11685.0	-

Note:

1. Load type in SIMO should be assigned to “gravity and buoyancy not included”.
2. The drag coefficient (C_D) can follow “DNV-RP-C205 Table E-1” [41].
3. Quadratic drag force per unit length, C_{2x}, is in the longitudinal direction of the cylinder; C_{2y}/C_{2z} is in the transverse direction which can be obtained from the formula: $C_{2x} = (1/2)\rho_{sea}DC_D$, where D is the diameter of the spar and $\rho_{sea}=1025\text{kg/m}^3$.

Additionally, A specified force in the upward direction is applied on the original point of the system (0,0,0) to counter the gravity effect from the wind turbine and mooring lines. The specified force is equal to 9011.72 kN and illustrated in the Figure 3.11.

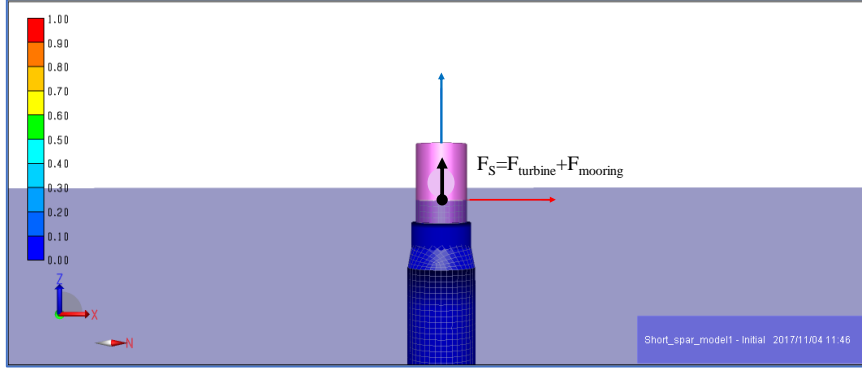


Figure 3.11. The illustration of specified force in short spar.

When a floater is freely floating, the restoring forces will follow hydrostatic and mass considerations. The linear stiffness matrix in SIMO is a 6 by 6 matrix which defines the stiffness in different degrees of freedom. Similarly, the weight of turbine should be excluded, thus the parameters in the matrix should be modified. The only non-zero terms for the spar as a symmetry plane for the submerged volume are C_{33} , C_{44} and C_{55} in heave, roll and pitch motions, respectively [39]. The stiffness matrix is summarized in the table below.

Table 3.11. Linear stiffness matrix terms in the short spar

Stiffness term	Unit
$C_{33} = \rho_{sea} g A_{WP} = 639.68$	[N/m]
$C_{44} = \rho_{sea} g V(z_b - z_G) + \rho_{sea} g \iint_{A_{WP}} y^2 ds$ $= (F_{spar\&turbine}) \cdot z_b - F_{spar} \cdot z_{G,spar} + \frac{\pi}{4} r_{WP}^4 = 1397853$	[Nm]
$C_{55} = C_{44} = 1397853$ (a symmetric plane)	[Nm]

Note:

1. A_{WP} is the water plane area of the spar.
2. $F_{spar\&turbine}$ is the gravity force of the spar, ballast and wind turbine.
3. z_b is the z-coordinates of the center of buoyancy for the overall system (spar, ballast and wind turbine).
4. $z_{G,spar}$ is the z-coordinates of the center of gravity for the spar and ballast only.
5. r_{WP} is the radius of the spar in water plane area.

3.3.2.2 Spar-Torus Combination VAWT

For this STC concept, the torus and the spar are modeled as two rigid bodies in SIMO program. The coupled connections between the torus and the spar are simulated with the coupling functions by using the features of SIMO. The spar in this concept needs to do some adjustments to offset the weight effect of the wind turbine during this stage. In principle these adjustments can follow the same procedures which have been introduced in Section 3.3.2.1. Thus, we do not go further discussion. The setup of the torus and the coupling are presented in the following parts.

The torus is considered as a rigid body in this simulation. Basically, the mass properties can be referred to Table 3.4. The viscous effect due to the flow in the horizontal direction is considered. One slender element was joined into the body to calculate the drag force along the submerged part. The quadratic drag force coefficient in the transverse direction of the torus is summarized in the Table below.

Table 3.12. Quadratic drag force coefficient of the torus

No	z [m]	L [m]	V [m ³ /m]	D [m]	C _D [-]	C _{2x} [Ns ² /m ³]	C _{2y} /C _{2z} [Ns ² /m ³]
1	0~0-2	2	204	20	1.0	-	10250

Note:

1. The drag coefficient (C_D) can follow Muliawan et al. [31].
2. Quadratic drag force per unit length, C_{2x}, is in the longitudinal direction of the cylinder; C_{2y}/C_{2z} is in the transverse direction.

The mechanism of coupled connections has been mentioned in the previous sections. The bearing system allows the torus to slide freely along the spar in heave, but the system forces the torus and spar to move together in the horizontal direction. A docking cone device from SIMO is applied in the coupled analysis. The torus and the spar are regarded as the docking cone point and the docking pin point, respectively. The motion behavior of the coupling system is illustrated in the Figure 3.12. As pin point of the spar goes into the opening cone of the torus, the relative motion in the horizontal direction will be restricted by the size of the cone at the respective distance (Δz). Once the pin point is outside the cone, a radial restoring force will be given to restrain the motion. This mechanical process could represent the contact force between the torus and the spar, which is shown in Figure 3.12. To deploy the feature of docking cone in the coupling simulation, three docking cones are specified at different elevations in this model. In addition, no friction force is considered along with the surface of the spar; hence, the torus can move freely in heave motion.

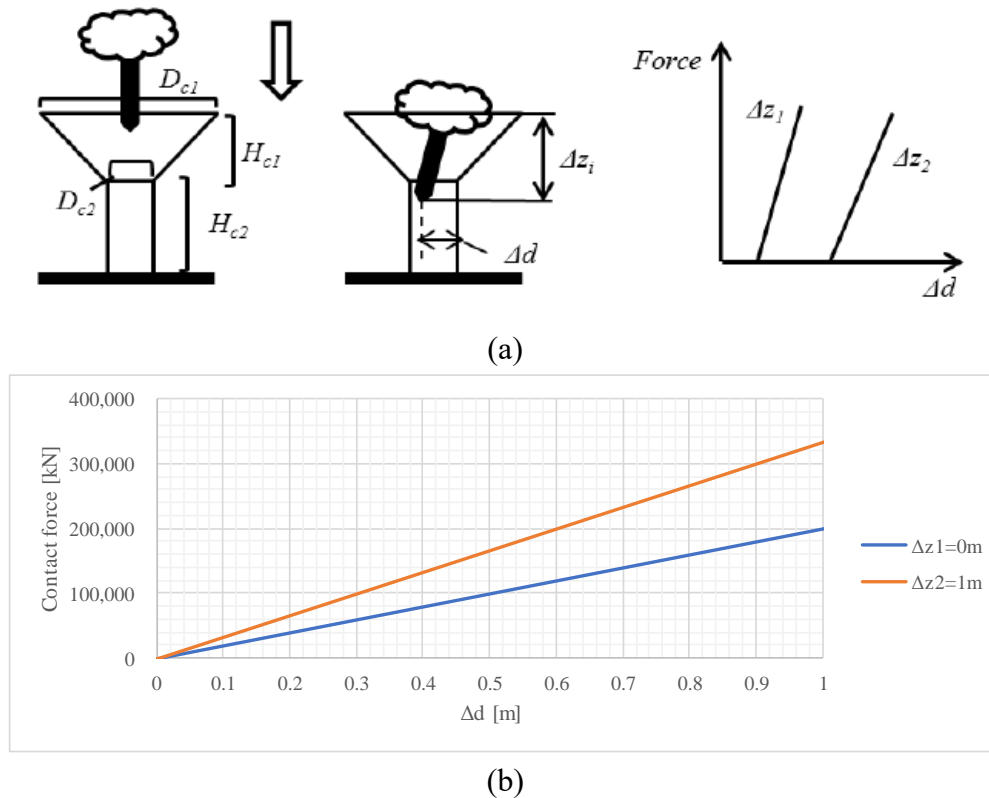


Figure 3.12. The motion mechanism of the docking cone coupling: (a) Illustration of docking cone coupling [36]; (b) Contact force.

The end stop system can control the excessive relative heave motion between the torus and the spar. A fender feature is applied in modeling the end stop system. Two fender planes of the spar are specified in the upper and lower location separately, and one fender point of the torus is defined in the center between the upper and lower fender plane. The mechanism of the fender feature is shown in the Figure 3.13. The coupling system will encounter resistance as the torus is in contact with one of the fender planes (distance < 0), and the contact force is demonstrated in Figure 3.13. The relation between the force and the contact distance can be modeled as a linear spring, and its properties have been mentioned in Table 3.5.

The power take-off (PTO) system captures the energy through the relative heave motion between the torus and the spar, which can be simplified as a linear stiffness spring and a linear damper. The fixed elongation coupling in SIMO is used to simulate these properties. The parameters of the stiffness and the damping in the PTO system can be referred to Table 3.5, which have been plotted in Figure 3.14.

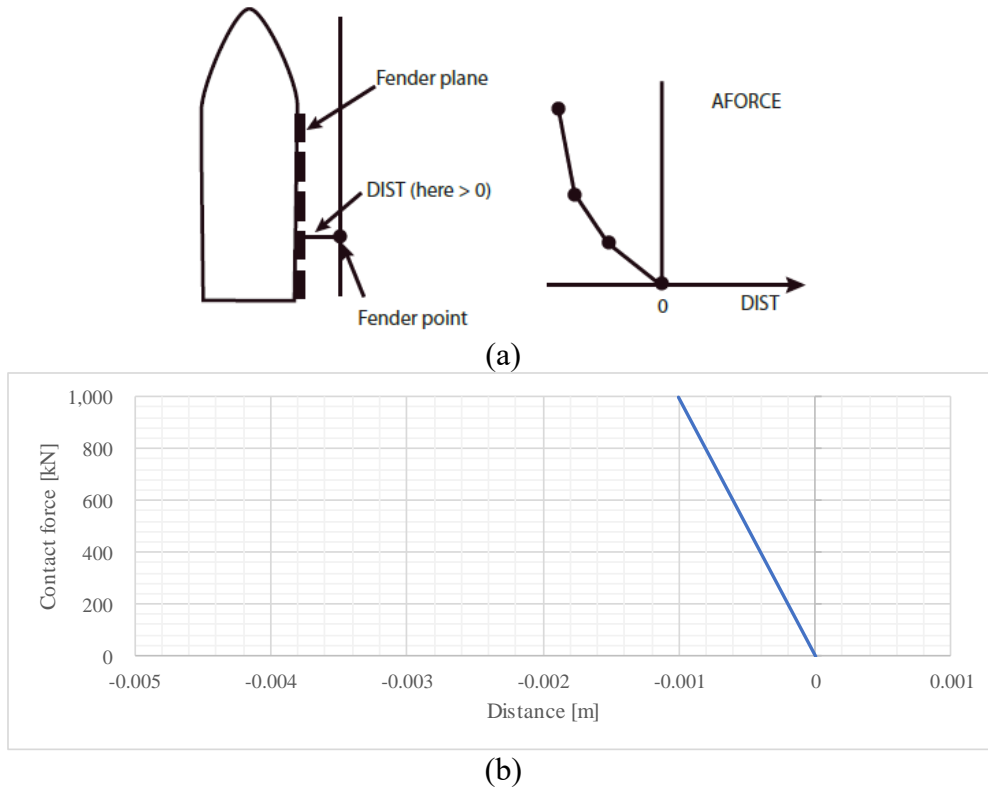


Figure 3.13. The mechanism of the fender coupling: (a) Illustration of fender coupling [47]; (b) Contact force.

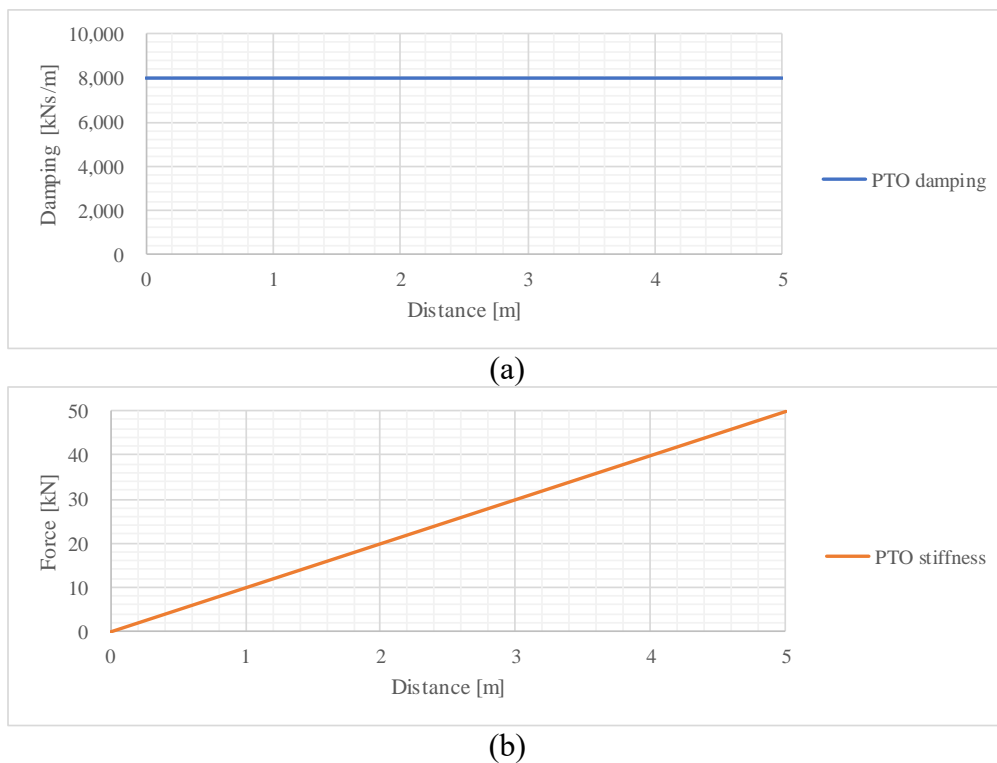


Figure 3.14. The properties of the fixed elongation couplings: (a) PTO damping; (b) PTO stiffness.

3.3.3 RIFLEX model

The floating VAWT system, including the blades, tower, shaft, and the mooring system, was modeled in the RIFLEX program. RIFLEX was developed as a finite element solver for analysis of mooring lines and other slender structures [49]. The blades, tower, and shaft are modeled as beam elements. The bar element is used to simulate the mooring line. For the sizes and settings of the VAWT, we can refer to Wang's Ph.D. thesis [14]. The configurations of three mooring lines in the deep spar and short spar follow the specifications of the spread mooring system mentioned in Section 3.1.

Basically, the configuration of mooring lines in short spar is designed by the static analysis, which is mainly controlled by the water depth, length of catenary and submerged length of hanging chain. The theory part and calculation results can be referred to Chapter 2 and Appendix B, respectively. The stress-free configuration of three mooring lines at initial stage should be given, then it will be loaded in RIFLEX model for static simulation. The final anchor points derived from the previous calculations should be specified in RIFLEX, and one of the mooring layouts is plotted in the figure below.



Figure 3.15. Mooring line of the short spar VAWT in X-Z plane.

On the other hand, the blade, tower, shaft and mooring lines in STC VAWT model remain the same settings as the deep spar VAWT, since the specifications of the spar structure and the wind turbine for both concepts are identical. This detailed information can follow Cheng et al. [33].

3.3.4 DMS model

The DMS model provides the aerodynamic loads acting on the blades through an external aerodynamic module. The aerodynamic response of the vertical wind axis turbine using the DMS model has been verified and studied by Wang et al. [38, 46].

The wind turbine configuration, airfoil aerodynamic coefficients, dynamic stall data, and wind field data are required for the DMS model. In this thesis, the performance and dynamic response of each concept under turbulent wind conditions are studied, whose wind field data are generated by the “Turbsim” program [34]. Due to the same 5MW Darrieus rotor on the short spar, deep spar, and Spar-Torus Combination, all the settings in this DMS model of each concepts are identical. Finally, the DLL is a critical link between DMS model and RIFLEX model, which can pass the information from each other.

3.4. Environmental conditions

In this study, normal operating conditions are considered for all concepts. A set of environmental conditions were chosen for simulating the dynamic response of all the floating structures [14]. The turbulent wind fields were generated from a Kaimal turbulence model in the Turbsim program according to IEC 61400-1 Class C, which also determines the turbulence intensity TI. The JONSWAP spectrum with significant wave height H_s and peak period T_p was used for describing the irregular wave condition. These loading cases are based on the calculation of correlated wind and waves at the Statfjord site in the Northern North Sea. In this area, a joint distribution for wind and wave proposed by Johannessen et al. is adopted according to the measurements from 1973 to 1999 as shown in the equation below [50].

$$f_{U_{10}H_sT_p}(u_{10}, h_s, t_p) = f_{U_{10}}(u_{10}) \cdot f_{H_s|U_{10}}(h_s|u_{10}) \cdot f_{T_p|H_sU_{10}}(t_p|h_s, u_{10})$$

The joint distribution is the product of a marginal distribution for wind, a conditional distribution of H_s for given U_{10} , and a conditional distribution of T_p for given H_s and U_{10} . Here U_{10} is defined as the 1-hour mean wind speed at 10m height. In this study, the wind speed U_w at a reference height of 79.78m in the range of cut-in and cut-out is considered; hence, the corresponding U_{10} can be found through the power of law as introduced in Section 2.1.

The conditional distribution of significant wave height H_s for given U_{10} is described as a 2-parameter Weibull distribution. The expected value of significant wave height is given as follow. Here α and β are the shape and scale parameters, respectively.

$$E(H_s) = \beta \Gamma\left(\frac{1}{\alpha} + 1\right)$$

$$\text{Shape: } \alpha = 2 + 0.135 \times u_{10}$$

$$\text{Scale: } \beta = 1.8 + 0.1 \times u_{10}^{1.322}$$

Johannessen et al. [50] recommended that a log-normal distribution is suitable for the conditional distribution of spectral peak period T_p for given H_s and U_{10} in this site. The expected value can be derived as the following formula. Additionally, the wind and waves are aligned and correlated for all loading cases. The overall environmental conditions are listed in Table 3.13.

$$E(T_p) = (4.883 + 2.68h_s^{0.529}) \left[1 - 0.19 \left(\frac{u_{10} - (1.764 + 3.426h_s^{0.78})}{1.764 + 3.426h_s^{0.78}} \right) \right]$$

For each loading case in all floating VAWT models, five sets of independent 4600-second simulation with random seeds were performed to express the turbulent wind and irregular wave conditions, and the mean values were derived from the time series data to reflect the stochastic variations. The 4600-second simulation can represent a one-hour duration since the startup effect in the first 1000 seconds has been eliminated.

Table 3.13. Environmental loading for the normal operating condition [14]

Load case	U_w [m/s]	TI [-]	H_s [m]	T_p [s]
LC1	5	0.224	2.10	9.74
LC2	10	0.157	2.88	9.98
LC3	14	0.138	3.62	10.29
LC4	18	0.127	4.44	10.66
LC5	22	0.121	5.32	11.06
LC6	25	0.117	6.02	11.38

Note:

The wind speed is the mean speed at the reference height of 79.78 m above MWL.

4. DYNAMIC ANALYSIS OF SPAR VAWTS

The dynamic response of spar VAWTs was calculated through time domain nonlinear fully coupled analysis, which includes the natural periods of the spar, platform motion, structural response, the tension of the mooring lines, and power production. Additionally, the comparison of the dynamic analysis between the deep spar and the short spar VAWT were studied under different environmental conditions. The application of the short spar VAWT in moderate water depth was discussed. The content in this chapter covers the most part of simulations from **Paper 1** [51].

4.1. Initial position of the dynamic model

Basically, the static analysis is critical to ensure the initial equilibrium of a numerical model, and the body could undergo a permanent deformation during the static equilibrium. For the simplicity, the induced static effect is neglected in the following simulation. The boundary condition of the original point to the spar body in both deep and short spar models is assigned to be fixed in all directions under static condition, then it will be released during dynamic simulation. Therefore, the whole system will remain at the original positions before running the dynamic analysis. The initial position of the dynamic model to the short spar is listed in the table below.

Table 4.1. Initial positions of all bodies in the short spar VAWT

Body	X _{glob} [m]	Y _{glob} [m]	Z _{glob} [m]	PHI [°]	THETA [°]	PSI [°]
Spar	0	0	0	0	0	2.5×10^{-6}
Hub	-2.5	0	79.78	0	0	2.5×10^{-6}

Note:

1.The static outputs are extracted from “stadmod.res” of RIFLEX.

4.2.Natural period of spar VAWTs

The natural periods of the short spar and deep spar VAWTs are presented in Table 4.2. Free decay tests were applied to identify the natural periods of the short spar VAWT as shown in Figure 4.1, and the natural periods of the deep spar VAWT can refer to Cheng et al. [33]. In general, free decay tests were carried out in calm water. The wind turbine was parked without any aerodynamic loads on the rotor, and one specified force was

acted in each of six degrees of direction with a very short period (200 seconds) to simulate its dynamic response.

For surge and sway, the natural periods of both spars are quite long. The natural period of the short spar is smaller than that of the deep spar, since the restoring stiffness of the short spar is larger due to the stiffer and shorter mooring lines. In heave, both spars are close to the upper limit of the wave periods. The short spar has a larger waterline area, and its natural period is smaller than that of the deep spar. For roll and pitch, the natural periods of both spars locate outside the range of wave periods; hence, the wave-induced resonant motions may not be substantial. However, both spars are situated inside the range of wave periods in yaw motion. A significant motion may be expected to occur in the yaw direction.

Table 4.2. Natural period of short and deep spar VAWTs

Motion	Deep Spar ^{1*} [s]	Short Spar [s]
Surge/Sway	130.8	89.8
Heave	27.3	21.6
Roll/Pitch	34.5	32.5
Yaw	8.5	7.1

Note:

1. The natural period of the deep spar was derived from Cheng et al. [33].

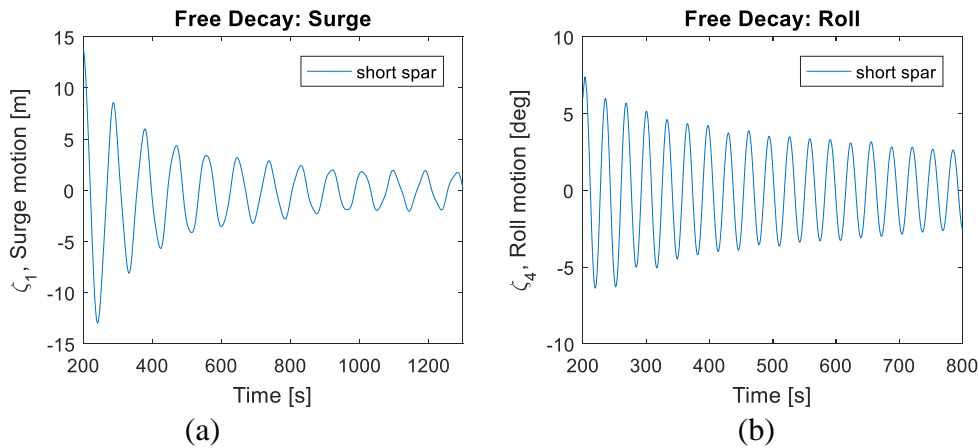


Figure 4.1. Free decay tests for the short spar VAWT: (a) Surge; (b) Roll.

4.3. Wind turbine performance

At a start-up stage, the rotor speed is accelerated initially to a higher operational speed depending on the controller before it reaches to rated rotational speed as shown in

Figure 4.2. However, this consequence could result in a larger variation of the structural dynamic force and the aerodynamical force. To avoid the unrealistic effect, all the simulation result will filter out the first 1000 seconds. Therefore, the dynamic simulation will be performed in a one-hour duration (1000 to 4600 seconds). Figure 4.2 shows that there is no significant difference in rotor speed between the short spar and the deep spar, since the same VAWTs are applied for both these two spar models.

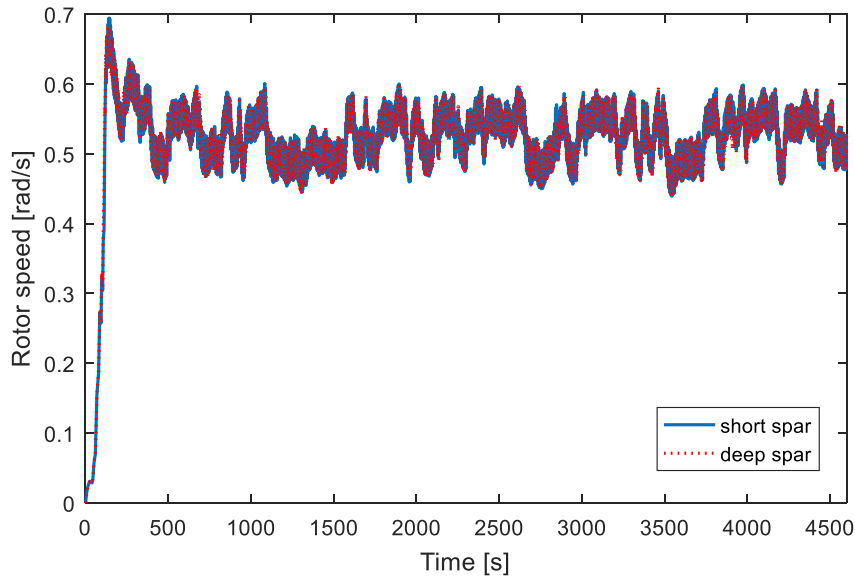


Figure 4.2. Comparison of time series in rotor speed for short spar and deep spar under LC3 with $U_w=14\text{m/s}$, $H_s=3.62\text{m}$, $T_p=10.29\text{s}$

The rotor speed of the short spar VAWT and deep spar VAWT under all loading cases are plotted in Figure 4.3 and summarized in Table 4.3. A good agreement on rotor speed between the short and deep spar VAWT are shown Figure 4.3. The rotor speed principally increases as the wind speed increases, but the rotor speed starts to decrease with the rising wind velocity after it reaches the rated speed. This mechanism can be explained by the fact that a PI generator controller is employed to decrease the rotational speed in order to keep the power approximately constant [14].

Table 4.3. Mean rotor speed for all loading cases

Load case	Mean rotor speed ¹ [rad/s]	2P frequency ² [rad/s]	2P period [s]
LC1	0.462	0.925	6.79
LC2	0.551	1.102	5.70
LC3	0.528	1.056	5.95
LC4	0.472	0.944	6.66
LC5	0.435	0.870	7.23
LC6	0.410	0.819	7.67

Note:

1. The mean rotor speed can represent the 1P frequency for each load cases.
2. 2P frequency is twice the 1P frequency and is the inverse of the 2P period.

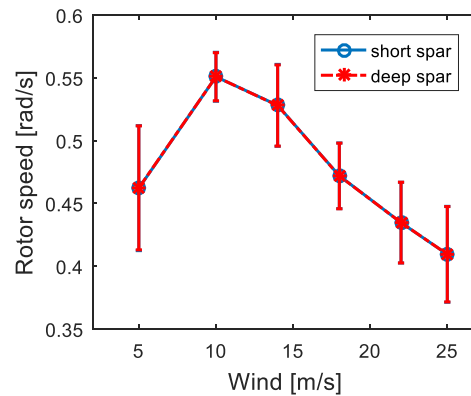


Figure 4.3. Mean rotor speed for the short spar VAWT and deep spar VAWT with error bar representing the standard deviation.

The rotor rotation causes the aerodynamic loads on the spar VAWTs. One of the most prominent dynamic loads in VAWTs is the 2P loading. The blade shadowing effect and the variation in torque lead to 2P loading, which is a periodic loading. The 2P frequency is twice the 1P frequency since the Darrieus wind turbine has two blades. The 2P loading can be decomposed into thrust and lateral force which are respectively parallel and normal to the wind flow direction, and it can be calculated from the integration of each aerodynamic load on the blade element.

A snapshot of the comparison between the 2P loading in the short spar VAWT and deep spar VAWT under rated speed (LC3) from 2000 to 2020 seconds is shown in Figure 4.4. Generally, the amplitudes of thrust and lateral force are similar. The mean value of lateral force is approximately zero, but the thrust fluctuates between zero and double the mean value. In addition, the amplitude of the short spar VAWT is almost the same as that of the deep spar VAWT in both thrust and lateral force, but the phase among these two spars is different. The average periods of thrust and lateral force are each around 6 seconds, which correspond to the 2P frequency.

Figure 4.5 displays the statistical comparisons of the thrust and lateral force for both spars under all loading cases. For simplicity, the results are plotted with the mean wind speed only even the loading includes the turbulent wind and irregular waves simultaneously. Both the comparisons indicate a good agreement between the short and deep spar VAWTs. The mean values and standard deviations of the thrust and lateral force increase separately as the wind speed increases.

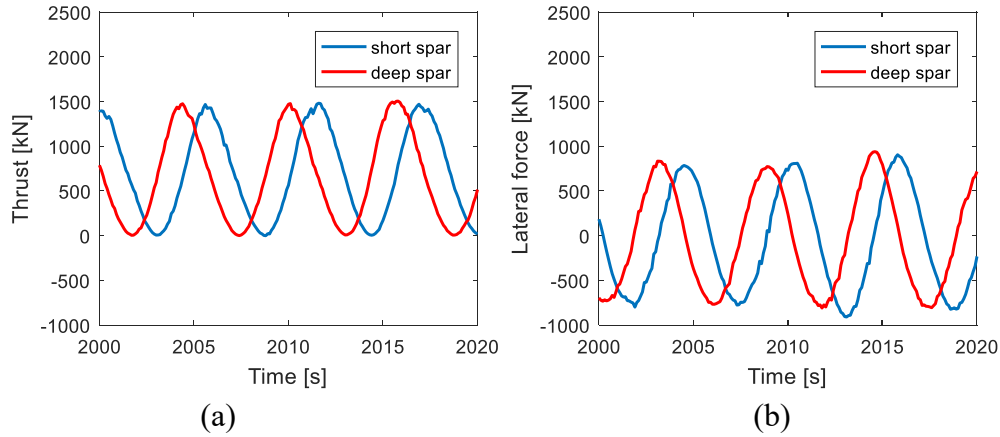


Figure 4.4. Comparison of time series in 2P loading for short and deep spar VAWTs under LC3 with $U_w = 14$ m/s, $H_s = 3.62$ m, $T_p = 10.29$ s: (a) Thrust; (b) Lateral force.

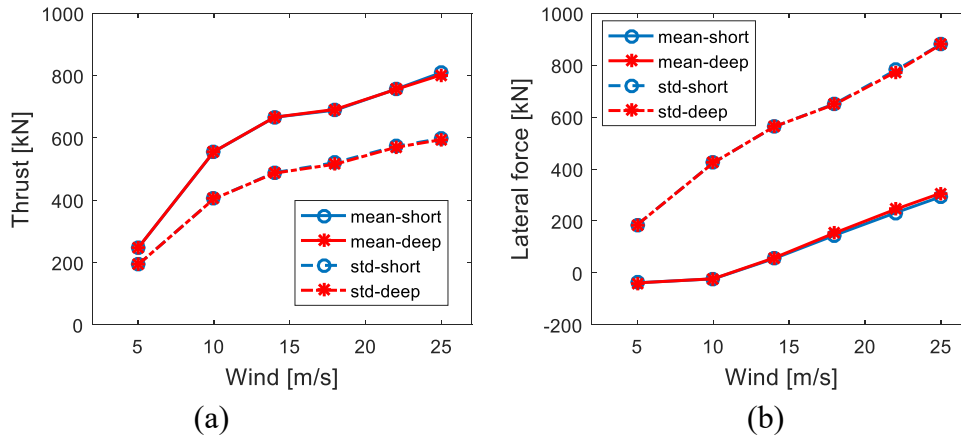


Figure 4.5. Comparison of mean values and standard deviations of the 2P loading for the short and deep spar VAWTs under all loading cases: (a) Thrust; (b) Lateral force.

The generator power production of the short and deep spar VAWT under all environmental conditions is plotted in Figure 4.6. This power curve shows the mean generator power production with the error bar indicating the standard deviations of the mean values. The short spar curve has a good agreement with the deep spar performance. The power production of both the short and deep spar VAWTs increases as the wind speed increases. While the wind speed exceeds the rated speed (14 m/s), the mean power production will be higher than 5 MW but remain approximately a constant value. The cause of this fact is that a PI-based generator torque controller is implemented to maintain an approximately constant generator power when the rated operation point is reached [15].

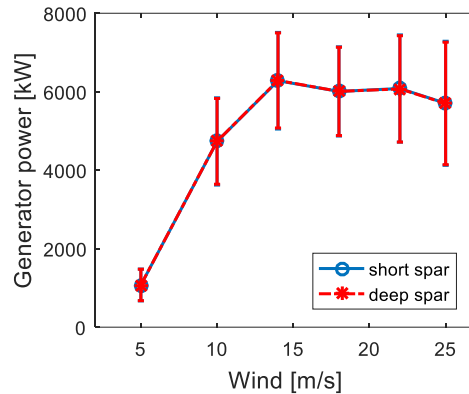


Figure 4.6. Mean power production for the short and deep spar VAWT with error bar representing the standard deviation.

4.4. Platform motion

The platform motion can be normally divided into six degrees of freedom, which includes surge, sway, heave, roll, pitch, and yaw motions. In this thesis, the heave is defined in global coordinates with the Z axis along the axial direction of the spar, and the surge is in the X axis which is parallel to the wind and wave direction (Figure 3.2).

The time series in global platform motions of the short and deep spar VAWT under rated wind speed with $U_w=14\text{m/s}$, $H_s=3.62\text{m}$, $T_p=10.29\text{s}$, are presented in Figure 4.7. Generally, both short spar and deep spar behave the similar trend, but the deep spar shows larger displacements than the short spar in surge and yaw direction. The comparisons of the mean values and standard deviations of the global motions under different environmental conditions between the short and deep spar VAWTs are shown in Figure 4.8. Similarly, the mean global motion is shown with error bars indicating the standard deviations of the mean values. Generally, the mean values of the global motions increase as the wind speed increases. Since more powerful wind will cause larger thrust and lateral force (Figure 4.5), stronger motions will be easily induced.

In comparing the two models in pitch and roll motions, the mean values of the short spar have good agreement with those of the deep spar. The standard deviations of the short spar are a little larger than those of the deep spar. The mean values and standard deviations of surge motion of the deep spar VAWT are significantly larger than those of the short spar VAWT. Since the surge motions were derived at the mean water level, a lower center of gravity (COG) of the deep spar VAWT with the same pitch angle could lead to larger motion in surge. However, the mean values of the deep spar VAWT in yaw motion give more significant responses than those of the short spar VAWT. This

could be the reason that the natural periods of the deep spar VAWT in yaw motion are much closer to the dominating wave energy.

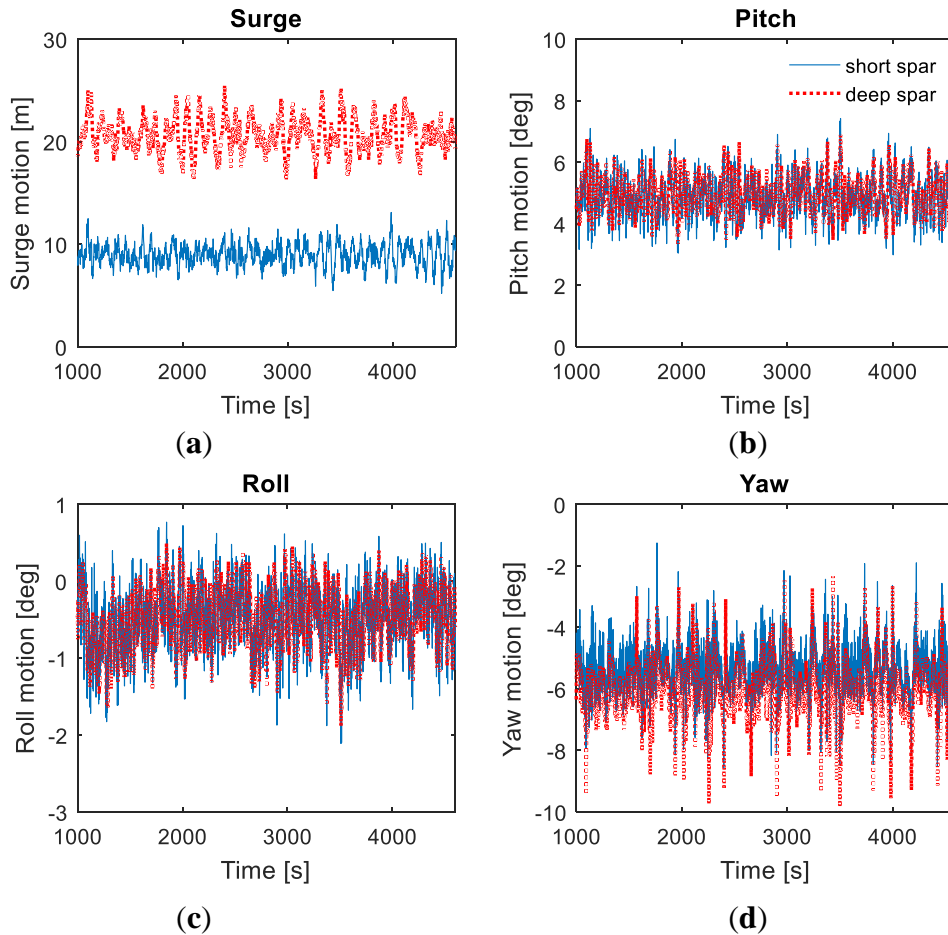


Figure 4.7. Comparison of time series in surge, pitch, roll, and yaw motions for the short and deep spar VAWT under LC3 with $U_w=14\text{m/s}$, $H_s=3.62\text{m}$, $T_p=10.29\text{s}$: (a) Surge; (b) Pitch; (c) Roll; (d) Yaw.

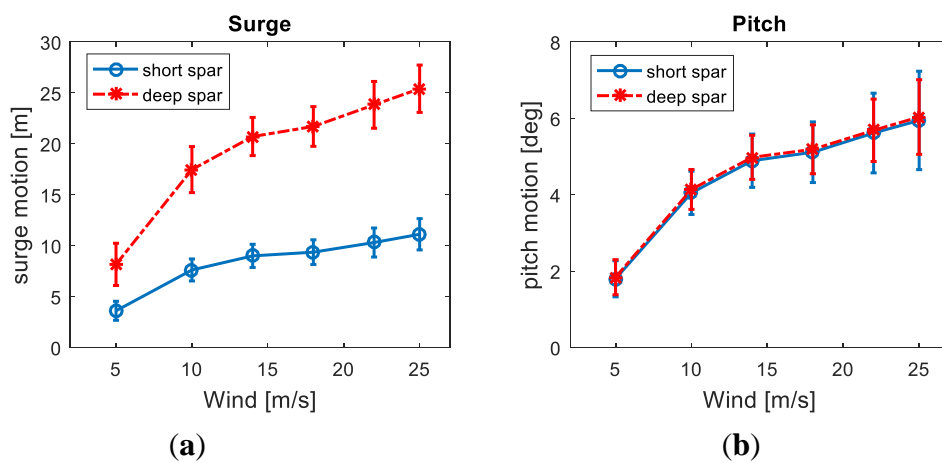


Figure 4.8. Comparison of mean values with error bar indicating the standard deviation in surge, pitch, roll, and yaw motions for the short and deep spar VAWT: (a) Surge; (b) Pitch; (c) Roll; (d) Yaw.

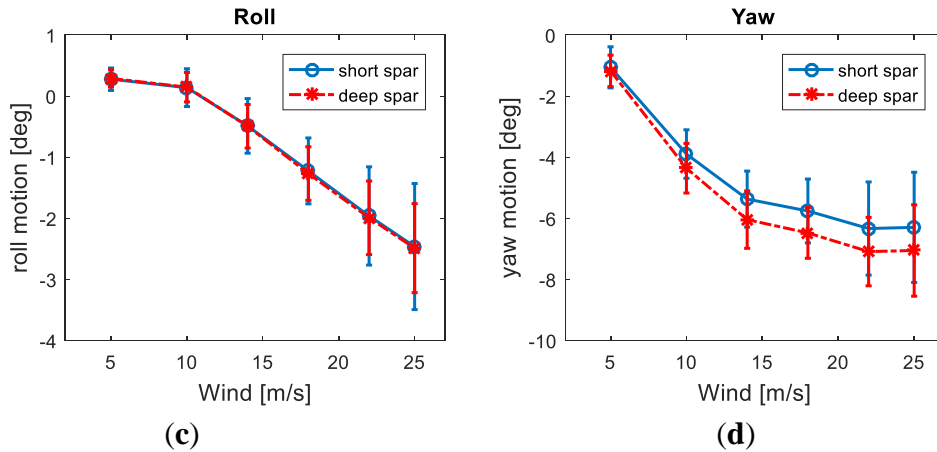


Figure 4.8. Continued.

The power spectra are used to analyze the time series of physical motions, which can reveal the frequency contributions in the standard deviation. A parzen window function is of benefit to filter or smooth the variation of the spectra in the frequency domain. The comparison of power spectra in six degrees of freedom between the short and deep spar under rated wind speed (LC3) can be found in Figure 4.9. Basically, these dynamic responses are mainly controlled by the resonant frequency, wave frequency, and 2P frequency. The short spar VAWT and deep spar VAWT have similar spectra distribution except in the heave motion. The heave motions of deep spar VAWT are dominated by its resonant response, whereas the wave-frequency-induced heave response is more prominent in the short spar.

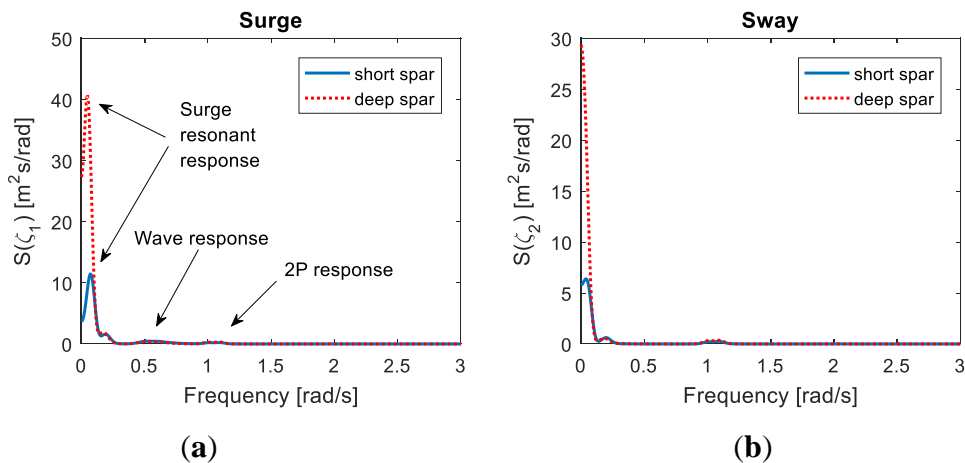


Figure 4.9. Comparison of power spectra in six degrees of freedom for the short and deep spar VAWT under LC3 with $U_w = 14$ m/s, $H_s = 3.62$ m, $T_p = 10.29$ s: (a) Surge; (b) Sway; (c) Heave; (d) Roll; (e) Pitch; (f) Yaw.

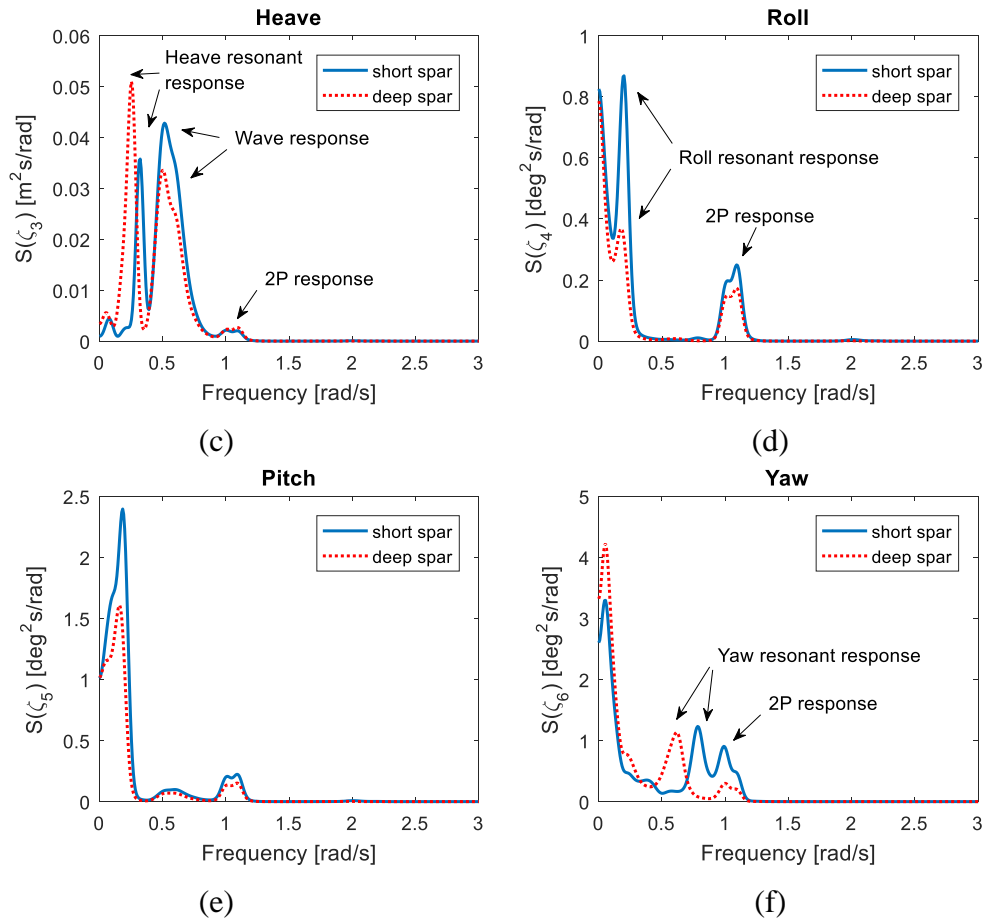


Figure 4.9. Continued.

The power spectra of the short and deep spar VAWTs in surge under each environmental loading are plotted in Figure 4.10. It can be found that the low frequency induced by turbulent wind responses is dominating when the wind speed is below the rated speed (LC3). The surge resonant response dominates when the wind speed is above the rated speed and is larger than the wave response and 2P response. Overall, the dominating spectra values in the deep spar VAWT are higher than those of the short spar VAWT, and the larger standard deviations of the deep spar in surge motion can also be found in Figure 4.8(a).

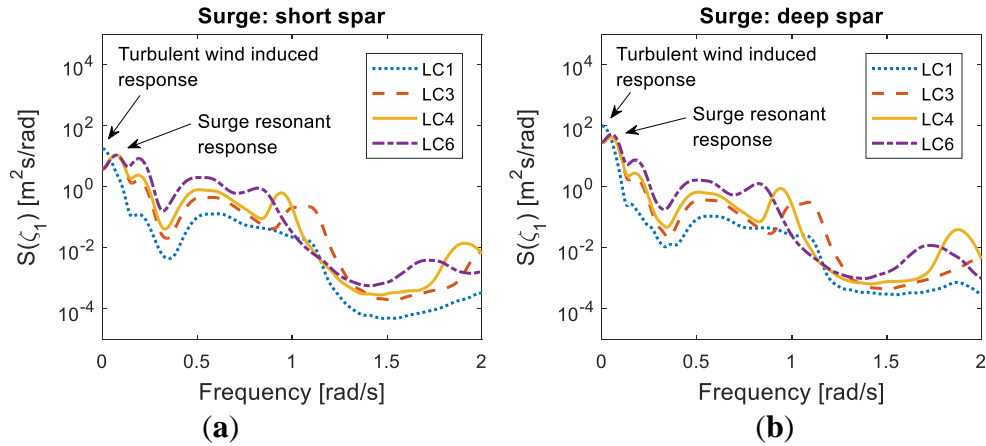


Figure 4.10. Power spectra in surge under all loading cases: (a) Short spar; (b) Deep spar.

The power spectra of yaw motions under all loading cases are plotted in Figure 4.11. The yaw spectra of the short and deep spar are mainly controlled by the low-frequency response and 2P response. The wave frequency response becomes more prominent for the deep spar under a severe environment, since its natural frequency in yaw motion is closer to the ocean wave frequency. In general, the 2P response dominates most loading cases in the yaw motion spectra, which highly correlates with rotor's rotation.

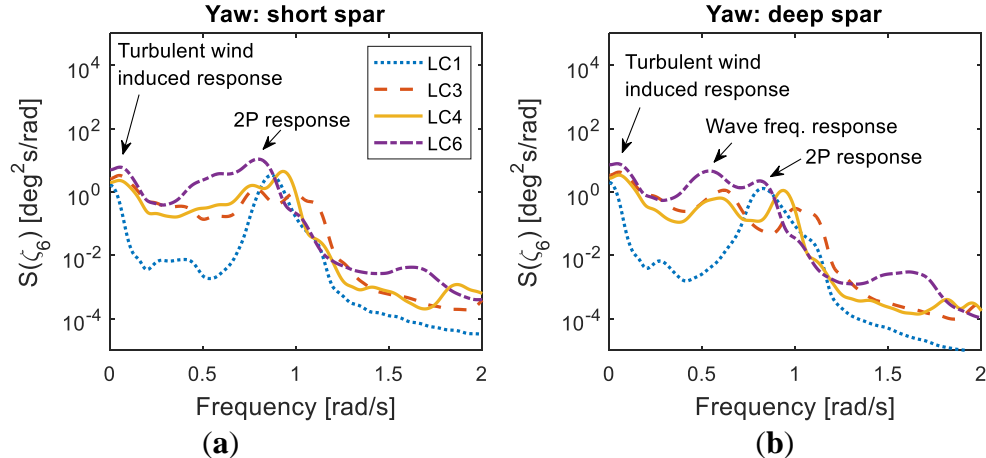


Figure 4.11. Power spectra in yaw under all loading cases: (a) Short spar; (b) Deep spar.

4.5. Tower base bending moments

The tower base bending moment is considered in this study. The bending moment is mainly induced by the aerodynamic force on the rotor and the downward gravity force of its self-weight owing to the tilted tower. The fore–aft and side–side bending moments are important indices to assess the structural performance of the wind turbine, as the aerodynamic forces vary with the azimuthal angle and cause large variation on these bending moments [14]. The fore–aft is parallel to the wind flow direction, and side–side is perpendicular to the wind flow. The time history of the bending moment for the short and deep spar VAWTs in fore–aft and side–side under rated speed (LC3) is shown in Figure 4.12.

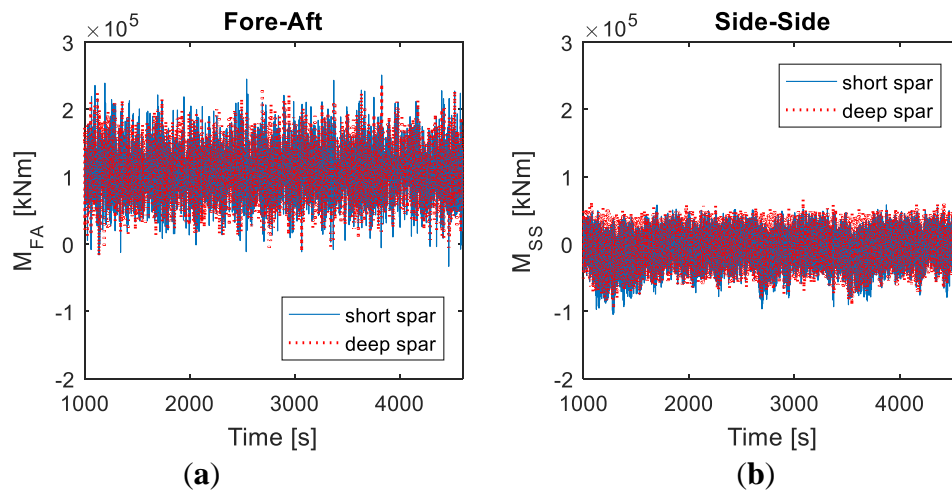


Fig 4.12. Time series of tower base bending moment for the short and deep spar under LC3 with $U_w=14\text{m/s}$, $H_s=3.62\text{m}$, $T_p=10.29\text{s}$: (a) Fore–aft; (b) Side–side.

Figure 4.13 compares the respective mean values, maximal values, and the standard deviations of fore–aft and side–side bending moments for the short and deep spar VAWTs. In this study, the maximum value in each loading case was derived from the mean of maximal numbers for each random seed simulation in the time domain. Overall, the comparison shows a good agreement between the short spar and deep spar. The mean, maximum, and standard deviations of the bending moment in both fore–aft and side–side directions increase as wind velocity increases.

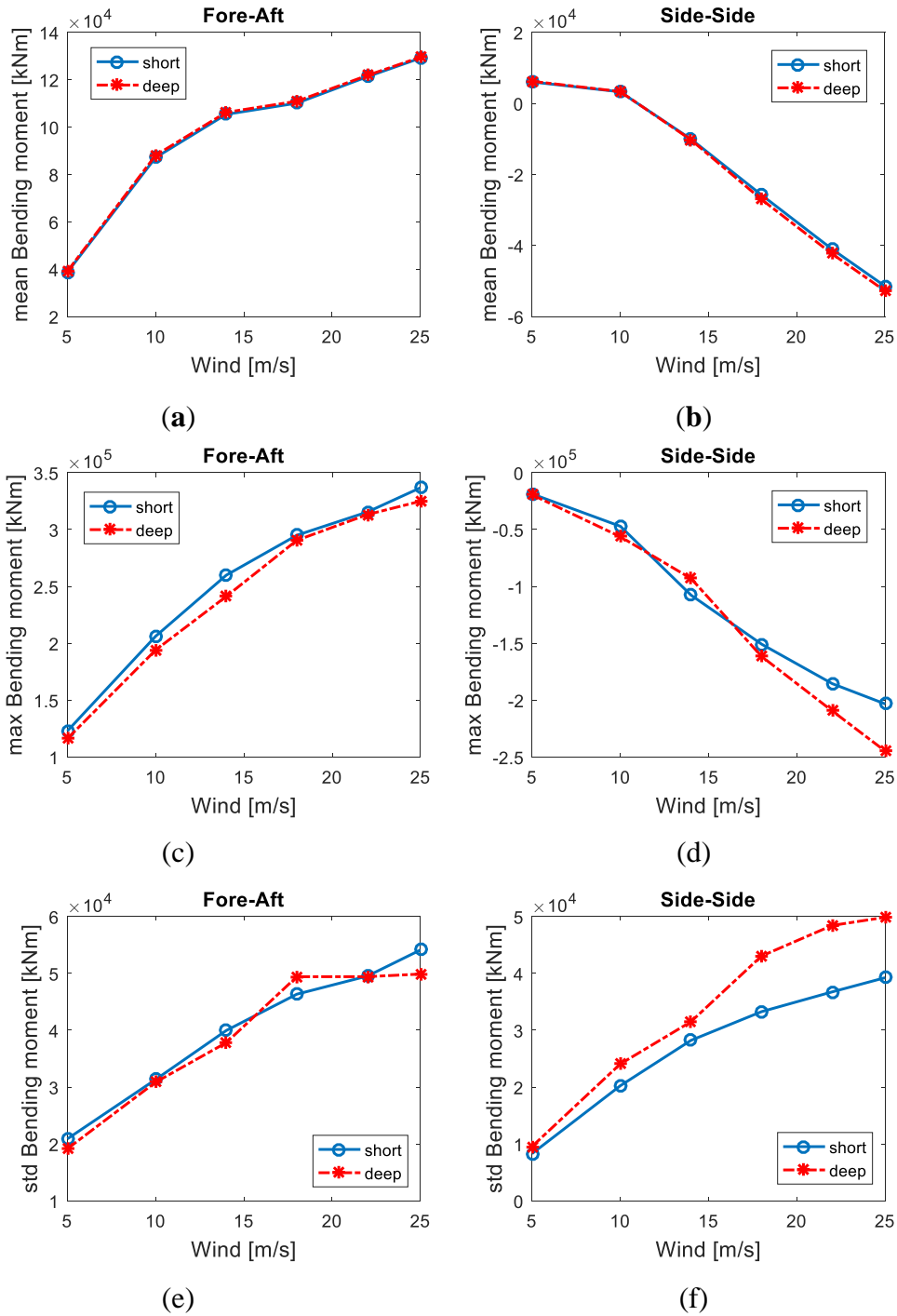


Figure 4.13. Statistics of tower base bending moment for the short spar and deep spar VAWTs: (a) Mean values in fore–aft; (b) Mean values in side–side; (c) Maxima values in fore–aft; (d) Maxima values in side–side; (e) Standard deviations in fore–aft; (f) Standard deviations in side–side.

The power spectra of the tower base bending moment under all environmental conditions for the short and deep spar VAWTs are shown in Figure 4.14. Whether in the short spar VAWT or the deep spar VAWT, 2P responses are almost dominating for all

loading conditions. A response close to 1.68 rad/s will become significant when the wind speed is above the rated speed (LC4 to LC6). A possible reason shows that the excitation may result from the structural resonance under a stronger loading condition [45]. The corresponding maxima spectra values for each loading case increase as wind velocity increases. The 2P responses of the deep spar VAWT in the tower base side–side bending moment are larger than those of the short spar VAWT, as are 2P responses in the tower base fore–aft bending moment for most loading cases. An exception is LC6 with $U_w = 25$ m/s and $H_s = 6.02$ m, under which the 2P responses of the short spar VAWT are larger than the corresponding values of the deep spar VAWT in the tower base fore–aft bending moments.

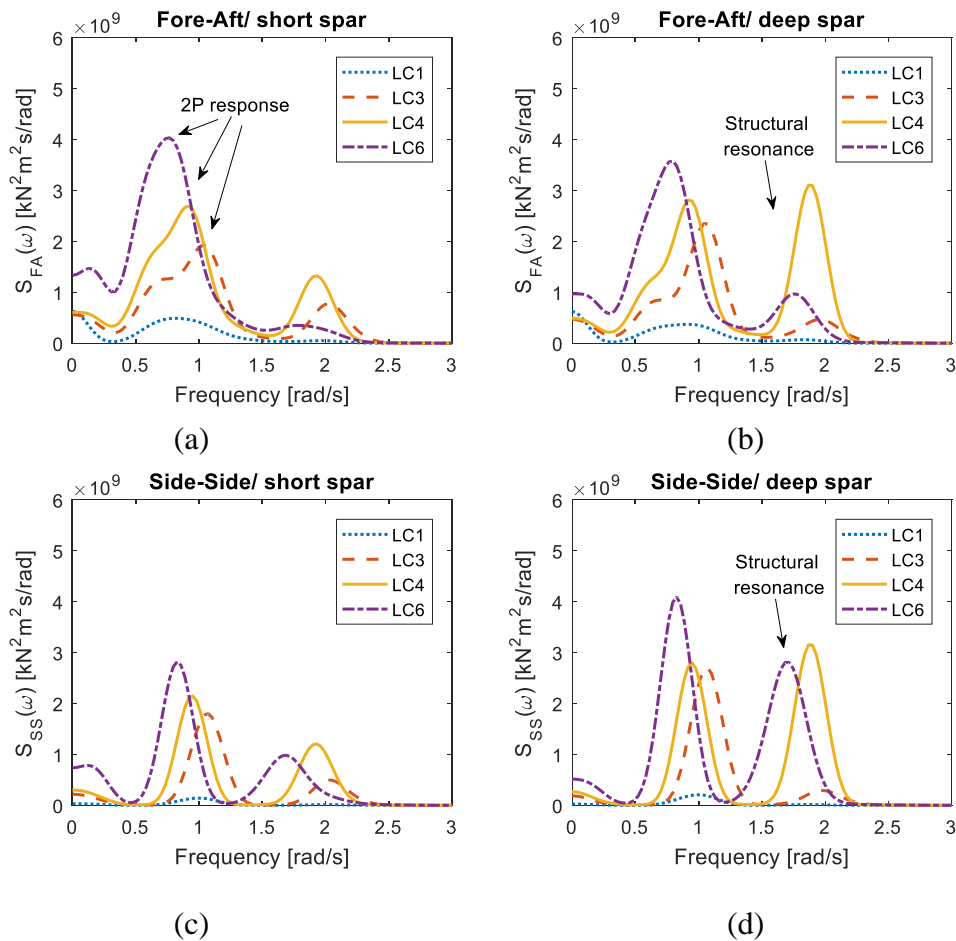


Figure 4.14. Power spectra of tower base bending moment under all loading cases: (a) Short spar in fore–aft direction; (b) Deep spar in fore–aft direction; (c) Short spar in side–side direction; (d) Deep spar in side–side direction.

4.6. Mooring line tension

The catenary mooring system is used for both the short and deep spar VAWTs. The main purpose of the mooring system is to maintain the floater in the proper position, and the delta line can provide yaw stiffness. For a conservative design approach, the turbulent wind and irregular waves are aligned in the same direction (+X global motion) in this study; hence, Mooring Line 1 will have the main role in withstanding most of the external force (Figure 3.2). The tension of Mooring Line 1 is measured at the anchor point and is the sum of tension in the upper line, clump mass, and lower line. The detailed mooring layout can be referred to Section 3.1. The time history of the tension in Mooring Line 1 for the short and deep spar under rated wind speed (LC3) are recorded in Figure 4.15. This figure indicates that each tension of mooring line in the short spar has a larger variation than in the deep spar.

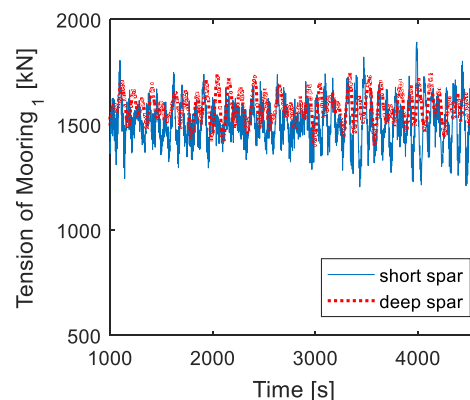


Figure 4.15. Time series of the tension in Mooring Line 1 under LC3 with $U_w=14\text{m/s}$, $H_s=3.62\text{m}$, $T_p=10.29\text{s}$.

Figure 4.16 presents the mean values, maximal values, and standard deviations of Mooring Line 1 for the short and deep spar VAWTs under all environmental conditions. Generally, the mean, maximal values and standard deviations increase as the wind speed and significant wave height increase. The mean values of tension for the deep spar VAWT are larger than those of the short spar VAWT, but the maxima values and standard deviations of the deep spar VAWT are smaller.

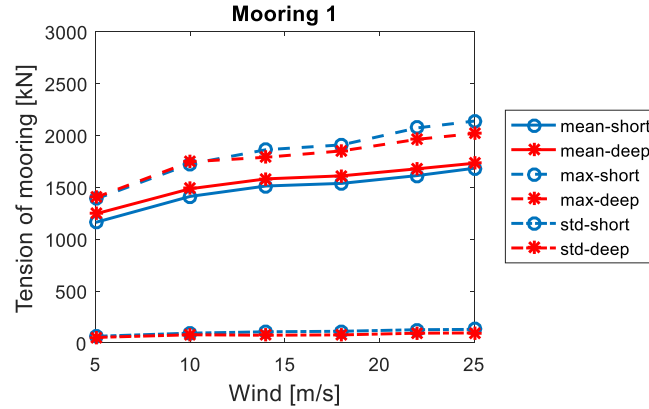


Figure 4.16. Statistics of the tension of Mooring Line 1 for the short spar and deep spar VAWTs.

Figure 4.17 compares the respective spectra of tension in Mooring Line 1 between the short spar and deep spar VAWTs under all the loading cases. Overall, the distribution of tension spectra in Mooring Line 1 for the short spar VAWT agrees well with that of the deep spar VAWT. The similarity between the short and deep spar VAWTs in the tension spectra is that the dominating wind-induced response increases as the wind speed and irregular wave state increase. However, the dominating spectra values of the short spar VAWT are significantly higher, as are the standard deviations of the tension of Mooring Line 1.

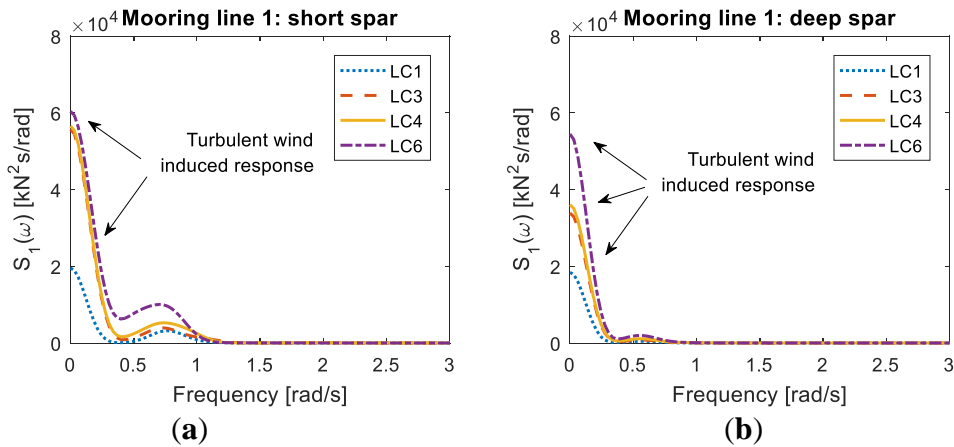


Figure 4.17. Power spectra of the tension in Mooring Line 1 under all loading cases: (a) Short spar VAWT; (b) Deep spar VAWT.

5. DYNAMIC ANALYSIS OF STC VAWT

This chapter deals with the dynamic analysis of Spar-Torus combination (STC) VAWT concept. Five set of environmental conditions listed in Table 3.13 are applied to the dynamic simulation in the time domain. The coupled heave motion between the torus and the spar in the STC is firstly addressed. The power performance of the STC, which incorporates wave and wind energy, are discussed. The dynamic response of the aerodynamics, hydrodynamics, floater motion, tower base bending moment, and mooring line tension is studied. The torus effect on the whole system is also investigated. All the outcomes of the STC VAWT model are compared with the spar-type VAWT by Cheng et al. [33] and presented in this chapter.

5.1. Coupled motion of torus and spar

This first part mainly addresses the coupled motion in heave, since the rest of directions are restrained by the bearing system as mentioned in Section 3.2.3. The capacity of power production from the wave energy converter relies on the coupled heave motion between the torus and the spar, as they move vertically with different phase angle. The wave energy absorption could be derived from a conversion of their relative motion and introduced as follow. The coupled motion in the simulation is presented in Figure 5.1.

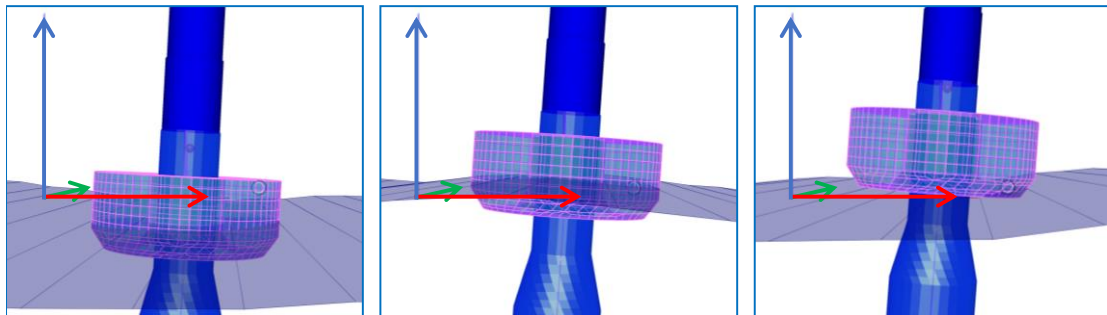


Figure 5.1. The coupled motion between the torus and the spar in the combined concept.

The heave motion of both torus and spar is excited by the incoming wave. The vertical wave excitation force acts on the bottom wet surface of a floating structure, which is the integration of the dynamic water pressure with respect to the area. Since the dynamic water pressure declines exponentially with the water depth, an extremely small value of the vertical wave excitation force on the bottom of the structure is expected in deep water. A smaller draft and a larger bottom area should lead to larger vertical wave excitation force on the torus. A comparison of the first order wave force in vertical

component at 2400s to 2600s under loading case LC3 between the spar and the torus is plotted in Figure 5.2. Obviously, the torus shows larger variations of the first order wave force in the vertical direction than the spar of the STC system. In addition, a phase difference of π between the torus and the spar in the vertical first order wave force can be roughly observed, which could be caused by the interior coupled connection.

A snapshot of the comparison of the heave motion between the spar and the torus under loading case LC3 from 2400 to 2600s is plotted in Figure 5.3. Basically, both the spar and the torus move together in heave with a small phase difference. That is, the reaction of the torus in heave motion is slightly earlier than the spar. The variations of torus motion in heave are more significant than that of the spar, whereas their difference is smaller than 3m due to the deployment of the end stop system. A similar phenomenon can also be found in the heave velocity of the torus and the spar under LC3 with the same period as shown in Figure 5.4. The above findings indicate that the torus with larger external loads carries the spar through the coupled connections and generates systemic motions in heave direction.

The heave velocity of the torus relative to the spar can be derived from the individual motion of these two bodies. The relative velocity between the torus and the spar under LC3 from 2400 to 2600s is plotted in Figure 5.5. Since a relative heave motion is found among these two bodies, a coupled force could also exist in this system. The coupled force is correlated to the PTO system, which is simplified with a linear spring and a linear damper in this model. The damping force in the PTO system is proportional to the relative velocity in heave direction between the torus and the spar due to a linear damper. The relationship between the damping force and the relative velocity is formulated in the equation below. As a constant damping $B_{PTO}=8000$ kNs/m is determined in this study, the damping force can be easily obtained.

$$F_{PTO,damp} = B_{PTO} \times V_{rel}$$

The wave energy is absorbed through the wave energy converter (WEC) and only related to the coupled force of the damper; hence, the wave power production can be calculated from the following equation. A time series of the wave power production from 2250 to 2750s under LC3 is plotted in Figure 5.6(a). The generator power production of VAWT can be directly loaded data from RIFLEX outcome, and a comparison of wind and wave power production is shown in Figure 5.6(b). Generally, the captured wind energy is higher than the wave energy, but the additional wave power production can increase the total amount of power generation of the whole system.

$$P_{WEC} = F_{PTO,damp} \times V_{rel}$$

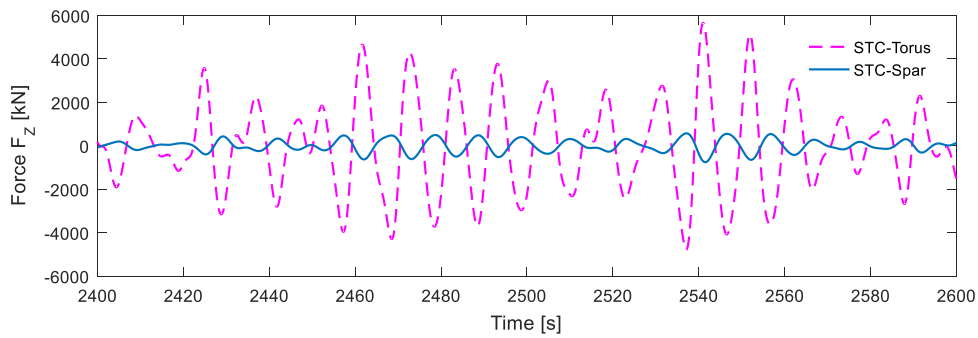


Figure 5.2. First order wave force in the vertical component of the torus and the spar under LC3 with $U_w=14\text{m/s}$, $H_s=3.62\text{m}$, $T_p=10.29\text{s}$.

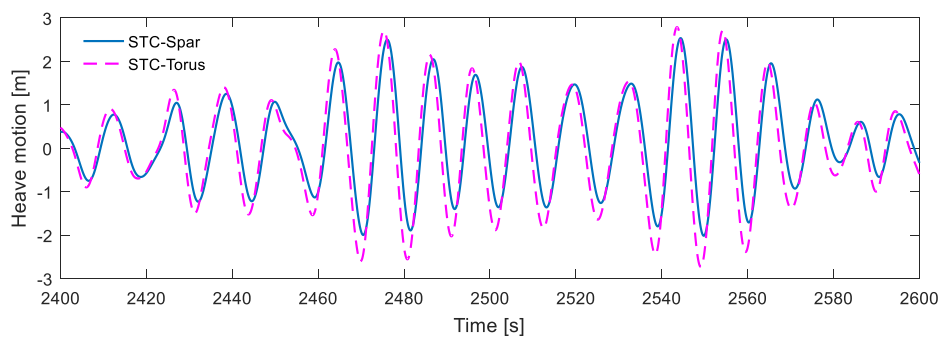


Figure 5.3. The heave motion of the torus and the spar under loading case LC3 with $U_w=14\text{m/s}$, $H_s=3.62\text{m}$, $T_p=10.29\text{s}$.

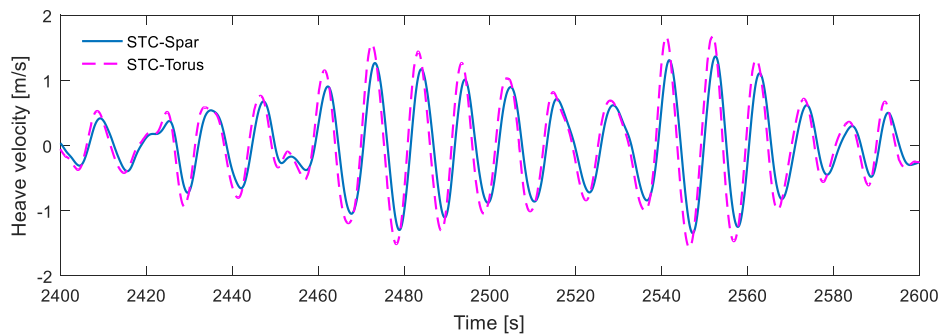


Figure 5.4. The heave velocity of the torus and the spar under loading case LC3 with $U_w=14\text{m/s}$, $H_s=3.62\text{m}$, $T_p=10.29\text{s}$.

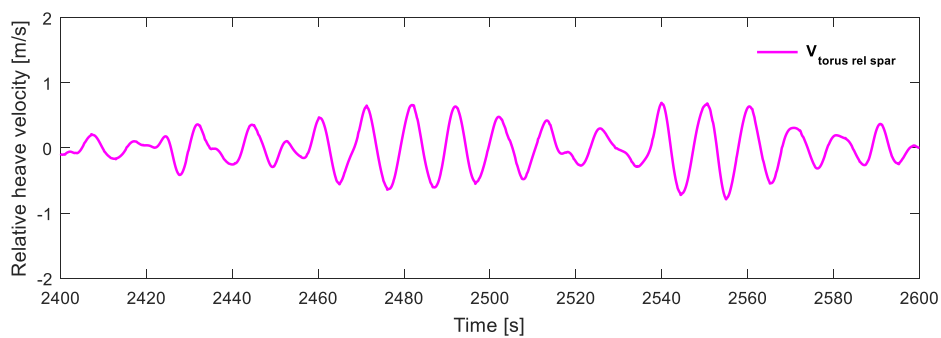


Figure 5.5. The velocity in heave of the torus relative to the spar under LC3 with $U_w=14\text{m/s}$, $H_s=3.62\text{m}$, $T_p=10.29\text{s}$.

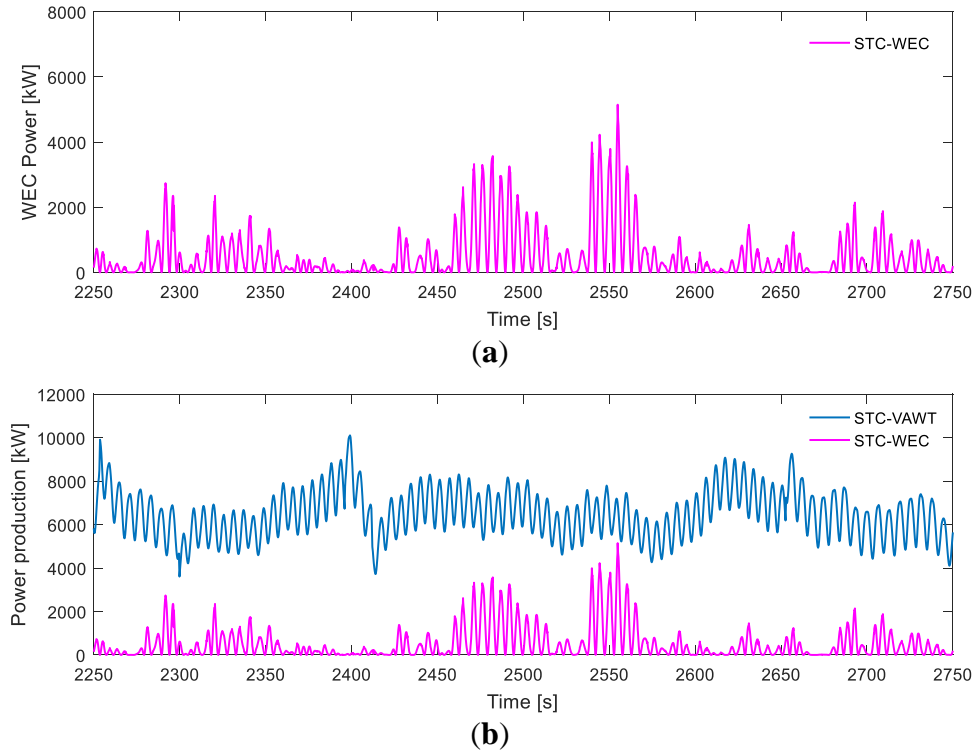


Figure 5.6. The power production of the STC VAWT concept under LC3 with $U_w=14\text{m/s}$, $H_s=3.62\text{m}$, $T_p=10.29\text{s}$: (a) Wave power production; (b) Wind power production.

5.2. Power performance

The generator power production from the VAWT of the system and the absorbed wave power through the wave energy converter (WEC) are compared and discussed in this section. Since the efficiency of the power generation from WEC is controlled by the PTO system, the optimum PTO parameters are determined in the first step and then applied to the following simulations. The additional torus effect on the wind turbine performance is also investigated and given as follows.

5.2.1 Optimum analysis of PTO parameters

The absorbed wave energy is dominated by the PTO system. In this study, the PTO system is simplified with one linear spring and one linear damping in the numerical model. To perform maxima power generation from the WEC, the optimum parameters of the PTO system need to define. The linear stiffness K_{PTO} and linear damping B_{PTO} of the PTO system are sensitive to the wave energy absorption and then become the top priority to determine. Moreover, the wave energy production is directly related to environmental conditions. A bigger wave should release more wave energy. The

optimum parameters of the PTO system are investigated in an operational condition, which is listed in Table 3.13. The wave power production with different parameters is compared under each loading case and displayed in the Figure 5.7.

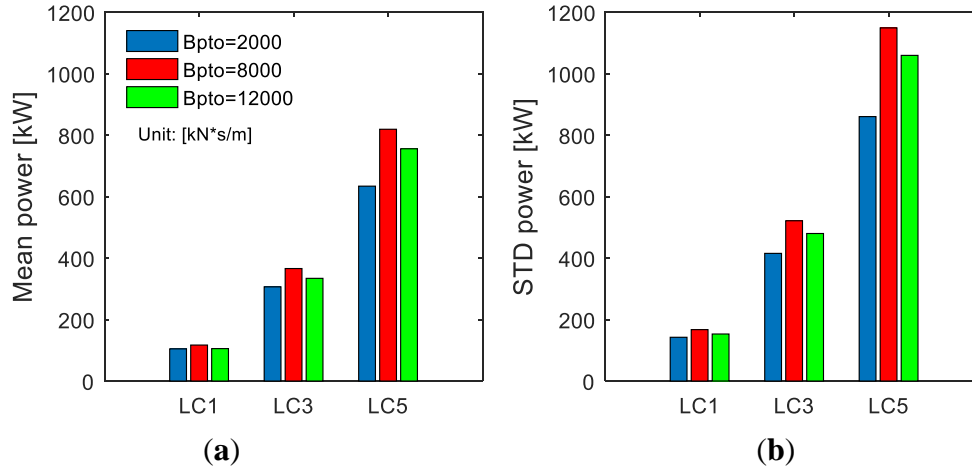


Figure 5.7. The optimum analysis of PTO parameters under different loading cases: (a) Mean wave power production; (b) Standard deviation of wave power production.

The linear spring and linear damper of the PTO system dominate the relative heave motion between the torus and the spar. For a stiff spring, the torus and the spar will behave like a whole rigid body and perform synchronous motions in heave. An appropriate stiffness of spring is necessary, and the damping term controls the power absorption. Figure 5.7 demonstrates the power production with a fixed stiffness $K_{PTO}=10$ kN/m and variable damping $B_{PTO}=2000$ to 12000 kNs/m under loading case LC1, LC3 and LC5. The result indicates that a higher damping could generate larger power, whereas it could also limit the relative heave motion and decrease the power absorption. The set of parameters with linear damping $B_{PTO}=8000$ kNs/m and linear stiffness $K_{PTO}=10$ kN/m could arouse the optimum performance in both mean and standard deviation of the wave power under such cases. The optimum parameters will be adopted for further simulations in this study.

5.2.2 Power production of the VAWT

The generator power production of the VAWT is related to the rotor speed, torque, and the control system. The rotor speed of the STC VAWT concept under all loading cases is plotted in the Figure 5.8 and compared with that of the spar-type VAWT by Cheng et al. [33]. Figure 5.8 displays the mean power of the VAWT with the error bar accounting for its standard deviations. A good agreement between STC VAWT and spar-type VAWT can be found from Figure 5.8, since both carry the same Darrieus rotor. A summarized of the mean rotor speed and 2P frequency of the STC VAWT under all

loading cases are listed in Table below.

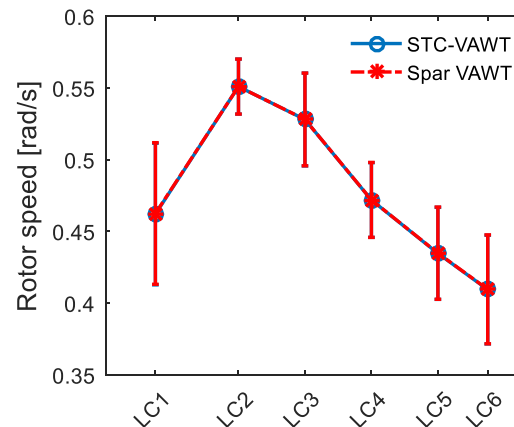


Figure 5.8. Mean rotor speed for the STC VAWT and the spar-type VAWT with error bar representing the standard deviation.

Table 5.1. Mean rotor speed of the STC VAWT for all loading cases

Load case	Mean rotor speed ¹ [rad/s]	2P frequency ² [rad/s]	2P period [s]
LC1	0.462	0.924	6.80
LC2	0.551	1.102	5.70
LC3	0.528	1.056	5.95
LC4	0.472	0.944	6.66
LC5	0.435	0.869	7.23
LC6	0.409	0.819	7.67

Note:

1. The mean rotor speed can represent the 1P frequency for each load cases.
2. 2P frequency is twice the 1P frequency and is the inverse of the 2P period.

The wind power production of the STC VAWT under all loading cases is shown in Figure 5.9. The mean power production increases with the wind speed until it reaches the rated speed (LC3), whereas it maintains an approximately constant power as the wind speed is higher than the rated speed. A PI generator torque controller, which has been introduced in Section 2.5, leads to this effect. Figure 5.8 and 5.9 also verified that the rotor speed decreases with the wind speed to keep the power approximately constant at wind speed above the rated speed.

In addition, a comparison of the wind power production between the STC VAWT and the spar-type VAWT is also given in Figure 5.9. The good agreements in mean and standard deviation of the wind power for both concepts can be detected in Figure 5.9; hence, it implies that the torus effect on the STC VAWT system does not make a significant contribution in the wind power production.

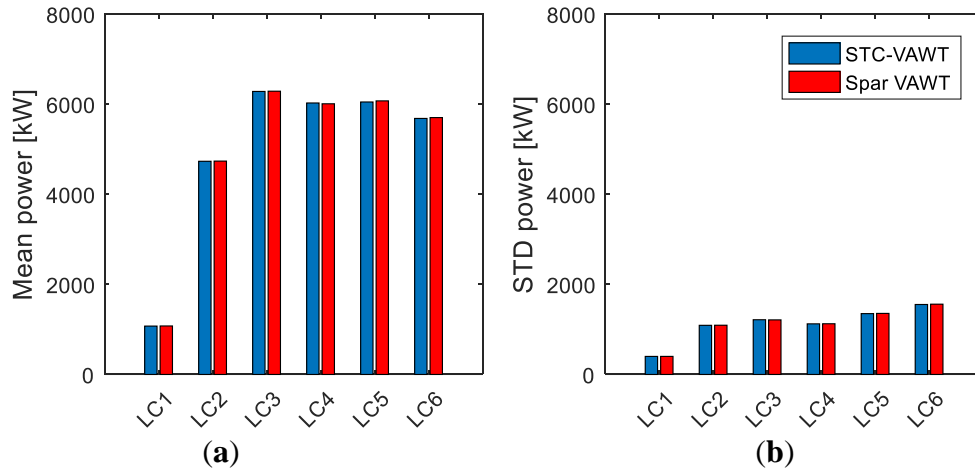


Figure 5.9. Power production of the STC VAWT and spar-type VAWT under all loading cases: (a) Mean wind power production; (b) Standard deviation of wind power production.

5.2.3 Power production of the WEC

A comparison of wave and wind power production in the STC VAWT system is one of the key points in this investigation. Figure 5.10 displays the mean power and standard deviation of power productions under all loading cases between the wave energy converter (WEC) and vertical axis wind turbine (VAWT) in this STC VAWT system. The variation of wind power production is determined through the control system as mentioned earlier. A positive correlation is found between the wave power production and environmental variations. Both mean and standard deviation of wave energy production increases as the significant wave height increases. In general, the VAWT can produce much more power than the WEC in the whole system. However, the total amount of power generation in the STC VAWT system still has been raised due to the contribution from the wave energy converter.

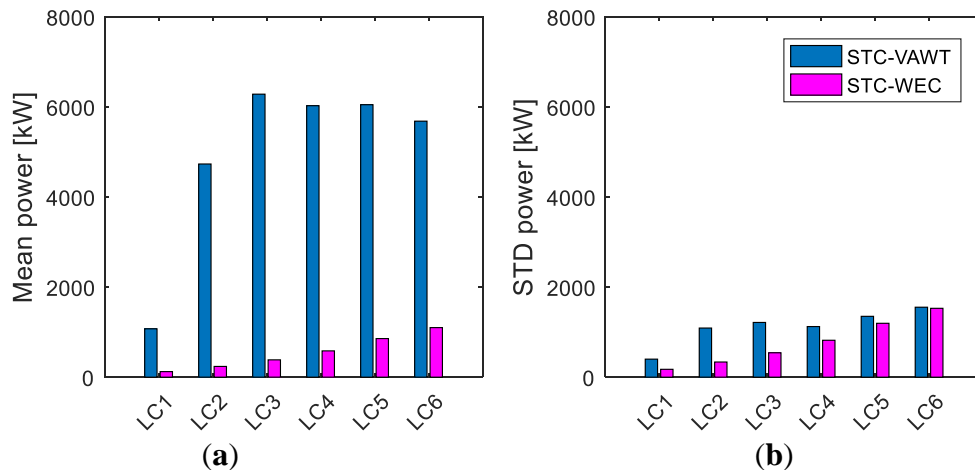


Figure 5.10. A comparison between wave and wind power production in the STC

VAWT system under all loading cases: (a) Mean power production; (b) Standard deviation of power production.

5.2.4 Estimation of annual power production

The characteristic of stochastic wind speed variations should be considered for computing the annual power production in the STC VAWT system, which could be roughly estimated through the distribution of mean wind speed and power production. A probability density function is usually used to model the distribution of wind speed. At the selected site in the North Sea, a two parameters Weibull distribution is utilized to describe the marginal distribution of 1-hour mean wind speed at 10m height, u_{10} , as shown in the equation below [50].

$$F(u_{10}) = 1 - \exp\left\{-\left(\frac{u_{10}}{\beta}\right)^\alpha\right\}$$

where $\alpha = 1.708$ and $\beta = 8.426$ are the shape and scale parameter, respectively. The wind speeds at reference height 79.78m in the range of cut-in and cut-out are given in Table 3.13, and its probability distribution can be derived through the power of law as mentioned in Section 2.1 and the transformations of the above formula.

$$\left\{ \begin{array}{l} \text{Power of law : } u_{10}(u_{ref}) = u_{ref} \cdot \left(\frac{z_{10}}{z_{ref}}\right)^\gamma \\ \text{PDF of 1-hr mean speed, } u_{ref} : f(u_{ref}) = F'(u_{10}(u_{ref})) \times u'_{10}(u_{ref}) \end{array} \right.$$

The annual power production can be obtained by the summation of the product of mean power and the corresponding probability of mean wind speed within one year. Since the wind and waves are inherently correlated, the above formula can be applied to estimate the annual wind and wave power production simultaneously in this combined concept.

Figure 5.11 compares the annual power production performance of the spar-type VAWT and the STC VAWT. Generally, the estimated result shows a good agreement between the only spar-type VAWT and the wind power production in the combined concept. The annual power production of the wave energy converter of the STC concept is about 2.2 GWh. Overall, an increment of the annual power production of the STC VAWT due to the extra wave energy is approximately 7% compared to the pure spar-type VAWT.

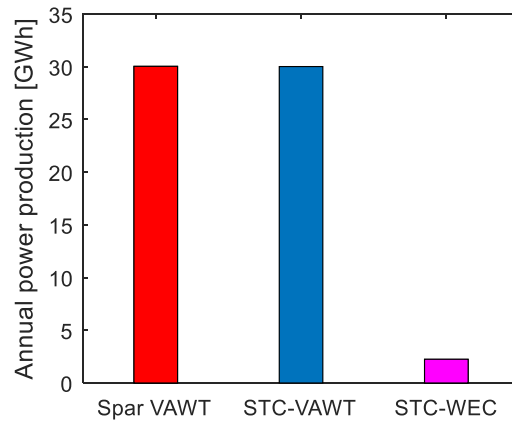


Figure 5.11. The prediction of annual power production for the spar-type VAWT and the combined concept.

5.3. Natural period of STC

Identifying the natural period of a system is the first step to study its dynamic behavior. In this study, the natural period of the STC VAWT is determined through free decay tests, which dynamic responses are assessed by applying a specified force at COG of the STC VAWT to each degree of freedoms with a duration of 200 seconds. Free decay tests are implemented in a calm weather which indicates a parked wind turbine and a tiny wave with 40 seconds peak period. The outcome of free decay tests is plotted in the Figure 5.12, and the natural periods of the STC VAWT are summarized in Table 5.2.

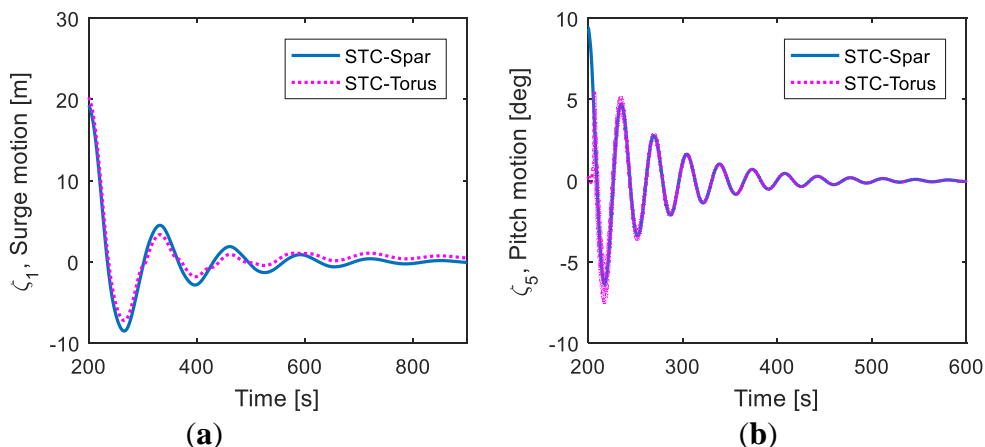


Figure 5.12. Free decay tests for the STC VAWT concept: (a) Surge; (b) Pitch.

The comparisons of the natural periods between the spar-type VAWT and STC VAWT are also listed in this table. Both concepts perform very long period in surge/sway. Even both concepts are governed by the same mooring system, the STC VAWT with larger total mass results in longer natural periods in surge/sway. For heave motion, the coupled

connection between the spar and the torus could affect the overall behavior of the combined concept. The water plane area of the STC VAWT is much larger due to the torus; hence, its natural period is smaller than the spar-type VAWT and is in the range of ocean wave periods. Although a resonant response in heave may occur during operation, the STC VAWT could be benefited from this effect and extract more wave energy. In roll and pitch, both concepts situate the outside range of ocean wave periods. An additional torus effect increases both the mass moment of inertia I_r and the rotational stiffness K_r of the STC VAWT system, thus its natural period is still close to that of the spar-type VAWT concept. Finally, the spar and the torus in the STC VAWT system move individually in yaw due to the lack of restriction in the yaw direction. The yaw stiffness of the spar and the torus in the STC VAWT system are controlled by the delta line and the empirical hydrostatic stiffness, respectively. The natural period of the torus shows a short period in yaw. For the spar in the STC VAWT system, its natural period in yaw locates within the range of ocean wave periods and is similar to the result of the spar-type VAWT.

Table 5.2. Natural periods of the spar-type VAWT and the STC VAWT

Motion	Spar-type VAWT ^{1*} [s]	STC VAWT [s]
Surge/Sway	130.8	139.3
Heave	27.3	12.2
Roll/Pitch	34.5	34.6
Yaw	8.5	7.9 (Spar) 3.1 (Torus)

Note:

1. The natural period of the spar-type VAWT was derived from Cheng et al. [33].

5.4. Aerodynamic load

The prominent aerodynamic loads on the vertical axis wind turbine (VAWT) involve thrust, lateral force and torque. The combination of thrust and lateral force is also called 2P loading, which is a periodic load. For a two blades Darrieus rotor, the aerodynamic loads vary twice per revolution due to a variation of the angle of attack with different azimuthal angles. The direction of thrust and lateral force is parallel and normal to the wind flow, respectively. The magnitude of the generator torque directly determines the wind power production from the VAWT. The thrust, lateral force and generator torque of the STC VAWT model under all loading case are plotted in Figure 5.13. The expression of loading case in X axis includes the combinations of the turbulent wind

and irregular waves as mentioned in Table 3.13. In principle, all these aerodynamic loads increase as the wind speed increases.

The statistical comparisons of aerodynamic loads between the STC VAWT and the spar-type VAWT are also shown in Figure 5.13. Whether it refers to the mean values or standard deviations, the good agreements between the STC VAWT and the spar-type VAWT exist. This outcome is expectable since the same VAWT is implemented in both concepts. The result also directly leads to the identical generator power output of both the STC VAWT and the spar-type VAWT as mentioned earlier in Figure 5.9.

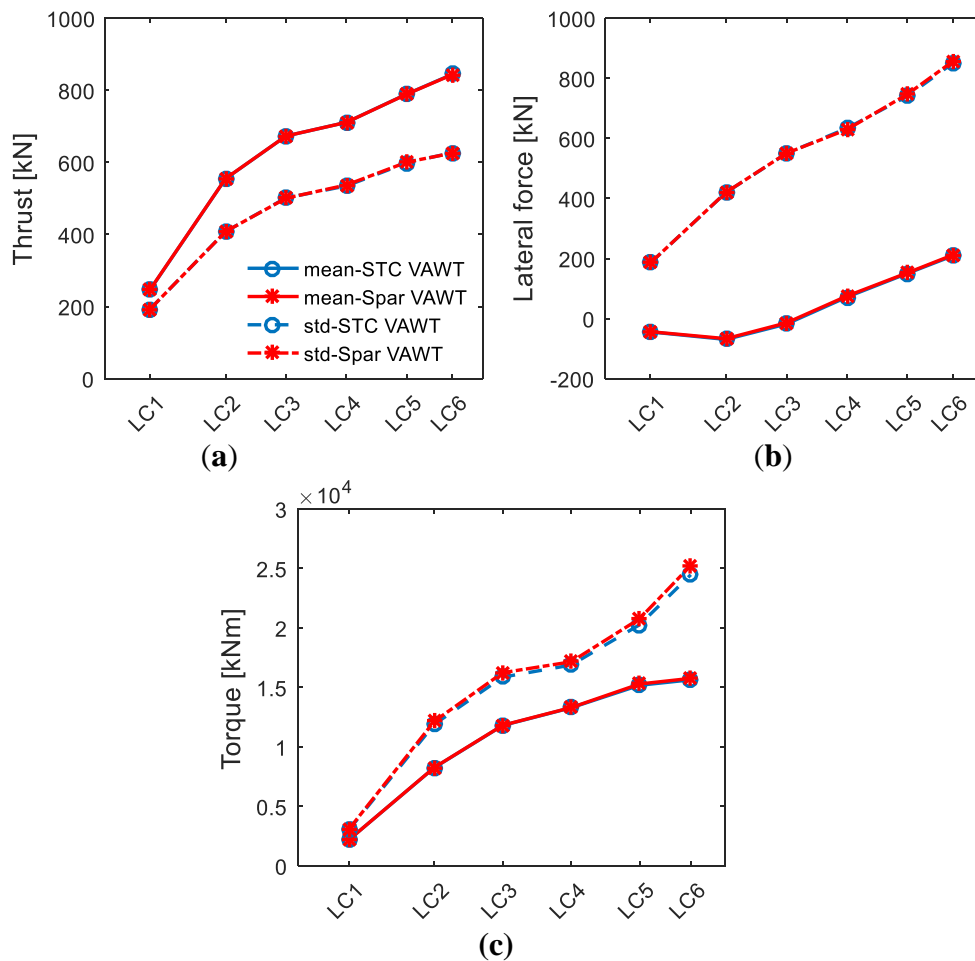


Figure 5.13. Statistical comparisons of aerodynamic loads between the STC VAWT and the spar-type VAWT under all loading cases: (a) Thrust; (b) Lateral force; (c) Torque.

5.5. Hydrodynamic load

The hydrodynamic load is also called wave excitation force in this study, which applies to the torus and the spar. The hydrodynamic load integrates the first order wave force and the second order drift force. However, the second order drift force is only considered in the horizontal plane, since it is estimated through the far field integration. Here +Z is specified to the vertical direction in the global coordinate of the model, and +X direction is parallel to the wind flow and the incoming waves which is also defined as fore–aft direction. Figure 5.14 gives a comparison in time series of the vertical first order wave force at 2250s to 2750s under loading case LC4 between the spar and the torus. Significantly larger variations of the vertical first order wave force are found in the torus.

Figure 5.15(a) gives the first order wave force in the fore–aft direction between the torus and the spar under LC4 at the same duration. The torus presents really smaller variations of the first order wave force in fore–aft than the spar of the STC, which could result from a smaller tangential wet surface of the torus. Overall, the torus displays much larger variations of the first order wave force in vertical than that of the fore–aft direction. Furthermore, the second order drift force in fore–aft for both the torus and the spar of the STC under LC4 at the identical period is given in Figure 5.15(b). Similarly, the smaller variations of the second order drift force in fore–aft are observed in the torus. Basically, the value of the second order drift force is always on the positive side, which implies it follows the direction with the first order wave force due to the numerical solution. Compared with the first order wave force, the variations of the second order drift force is much smaller.

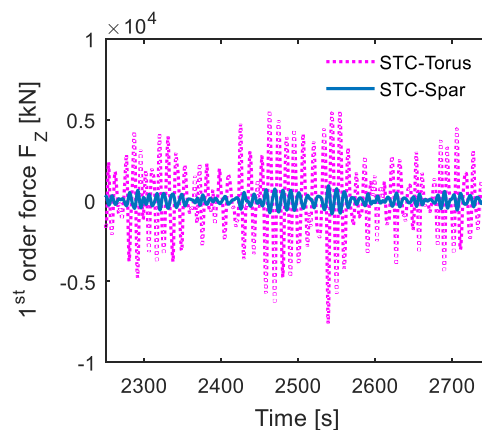


Figure 5.14. The first order wave force in the vertical direction between the torus and the spar under LC4 with $U_w=18\text{m/s}$, $H_s=4.44\text{m}$, $T_p=10.66\text{s}$.

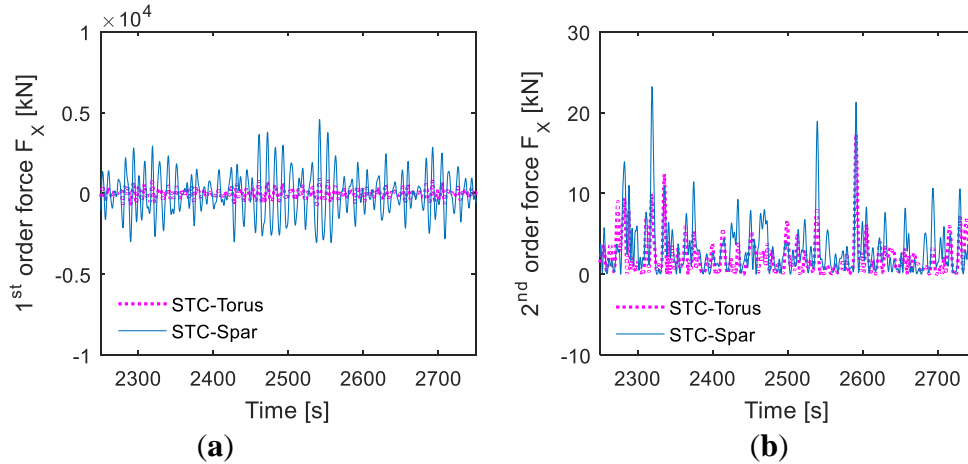


Figure 5.15. The wave excitation force in fore–aft direction between the torus and the spar under LC4 with $U_w=18\text{m/s}$, $H_s=4.44\text{m}$, $T_p=10.66\text{s}$: (a) First order wave force; (b) Second order drift force.

Power spectrum analyses are performed for the first order wave force and second order drift force in fore–aft for both the torus and the spar under LC4, which are shown in the Figures 5.16(a) and 5.16(b). Generally, the spar of the STC gives larger envelope area of spectra than the torus, which also implies the larger variations of wave excitation force in fore–aft on the spar. In the first order wave force spectra, the spar spectrum properly covers the main region of the wave frequency from 0.5 to 1.0 rad/s. The second order force spectra concentrate at the low frequency within 0.5 rad/s, which indicates the drift force induced response at low frequency should not be ignored.

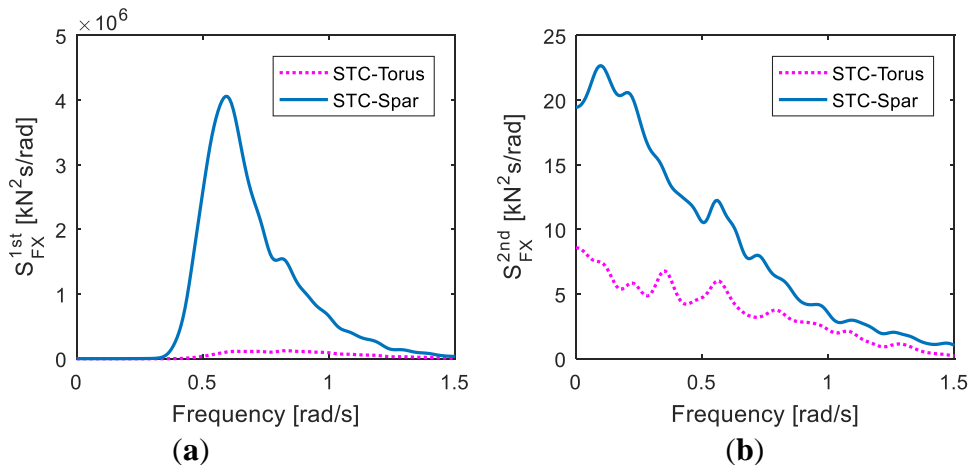


Figure 5.16. Spectral analysis of wave excitation force in fore–aft for the torus and the spar under LC4 with $U_w=18\text{m/s}$, $H_s=4.44\text{m}$, $T_p=10.66\text{s}$: (a) Power spectrum of first order wave force; (b) Power spectrum of second order drift force.

The resultant of wave excitation force on the STC system can be considered as the summation of first order wave force and second order drift force in the time domain. Figure 5.17 presents the resultant force at $t=2250\text{s}$ to 2750s under LC4 in both fore–aft and vertical directions. A comparison of resultant wave excitation force between the

STC and the spar-type VAWT is also shown in Figure 5.17. In general, the variations of wave excitation force on the STC are larger than the spar-type VAWT due to the additional torus effect, especially in the vertical direction.

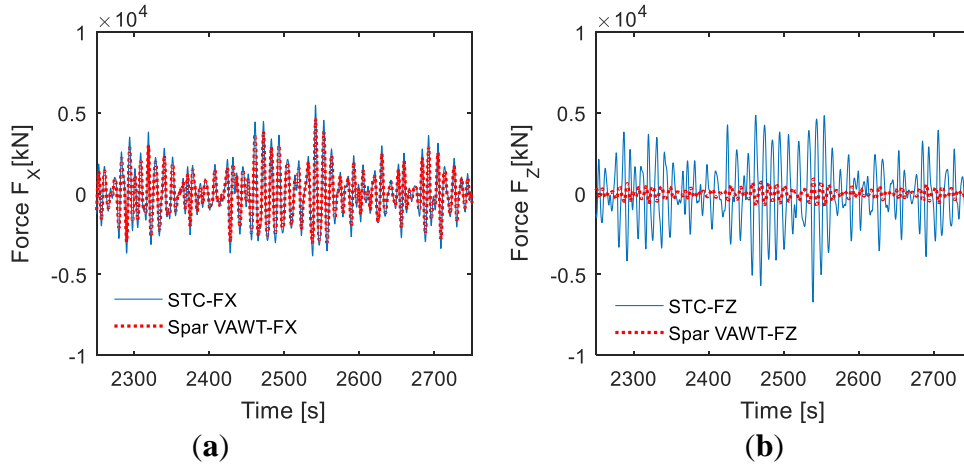


Figure 5.17. Comparisons of resultant wave excitation force between the STC and the spar-type VAWT under LC4 with $U_w=18\text{m/s}$, $H_s=4.44\text{m}$, $T_p=10.66\text{s}$: (a) Wave excitation force in fore–aft; (b) Wave excitation force in vertical.

Once again, the torus effect can be observed through the comparisons of resultant wave excitation force in fore–aft with mean values and standard deviations under LC4 to LC6 between the STC and the spar-type VAWT in Figure 5.18. Even a small discrepancy of mean values for both concepts is found in Figure 5.18(a), the STC presents much larger standard deviations of the resultant wave excitation force in fore–aft than the spar-type VAWT as shown in Figure 5.18(b).

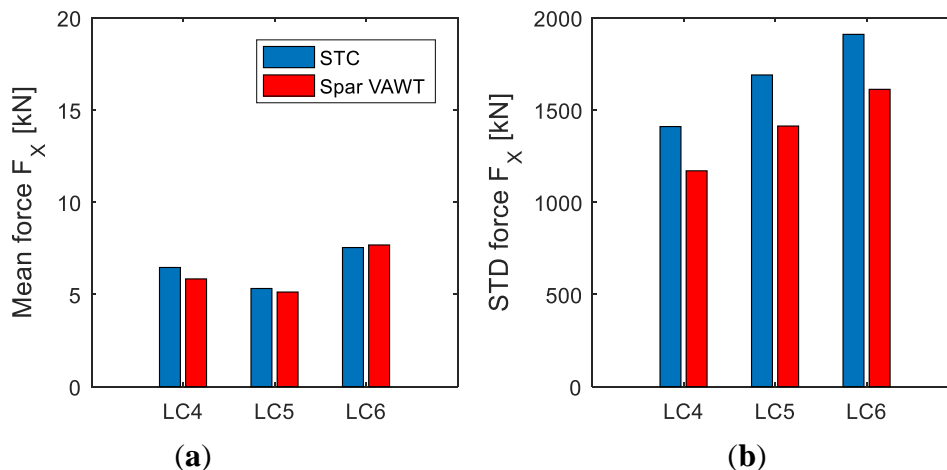


Figure 5.18. Comparative resultant wave excitation force in statistic under LC4 to LC6 between the STC and the spar-type VAWT: (a) Mean of wave excitation force in fore–aft; (b) Standard deviations of wave excitation force in fore–aft.

5.6. Floater motion

The motion of a floating system can be disassembled into six degrees of freedom, and the surge is defined as the direction along the X axis in the global coordinate system which is parallel to the wind and waves direction in this study. In the STC VAWT system, a coupled connection links the torus and the spar so that both move together except for heave motion. The motions of the spar and the torus in the STC VAWT under all loading cases in the time domain are investigated and given with statistical result in the Figure 5.19. This figure indicates that the surge motion of the spar coincides with the torus motion due to the bearing system effect as mentioned in section 3.2. In heave motion, the mean of both the spar and the torus are close to zero accounting for the dynamic balance of the whole system in the vertical direction. The standard deviations of the heave motion for both increase with the rising turbulent wind and irregular waves, and the torus presents more significant variations to allow more wave energy absorption.

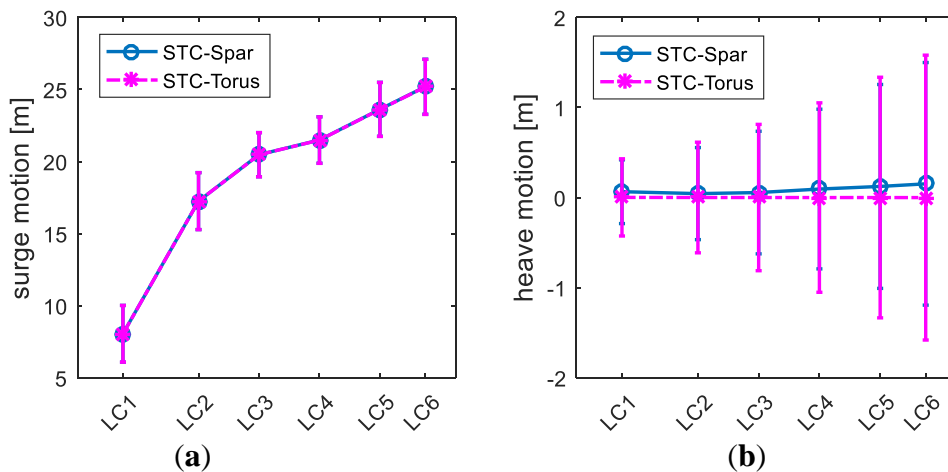


Figure 5.19. The mean floater motion of the spar and the torus with the error bars representing the standard deviations in the STC VAWT system: (a) Surge; (b) Heave.

A statistical comparison of the floater motion in time domain under all loading cases between the spar in the STC and spar-type VAWT is shown in Figure 5.20. The discrepancy of both concepts is insignificant in surge, sway and pitch. A general trend shows that the mean motion increases as the wind and waves increase, and the mean pitch motion of the STC is smaller. The standard deviations of the spar in STC are smaller than that of the spar-type VAWT, which implies the STC VAWT behaves a better performance in the stability. The reduction of the standard deviations of the floater motion in surge, sway and pitch for the STC system is caused by the additional torus effect. The torus experiences larger resistance near the mean water level and provides an additional damping effect for the whole system to mitigate its responses. In

heave motion, the spar in the STC performs much larger variation. This situation could be induced by the wave frequency response, since the heave natural period of the STC VAWT situates in the range of wave periods. However, this significant variations in heave drive the WEC to extract more wave energy.

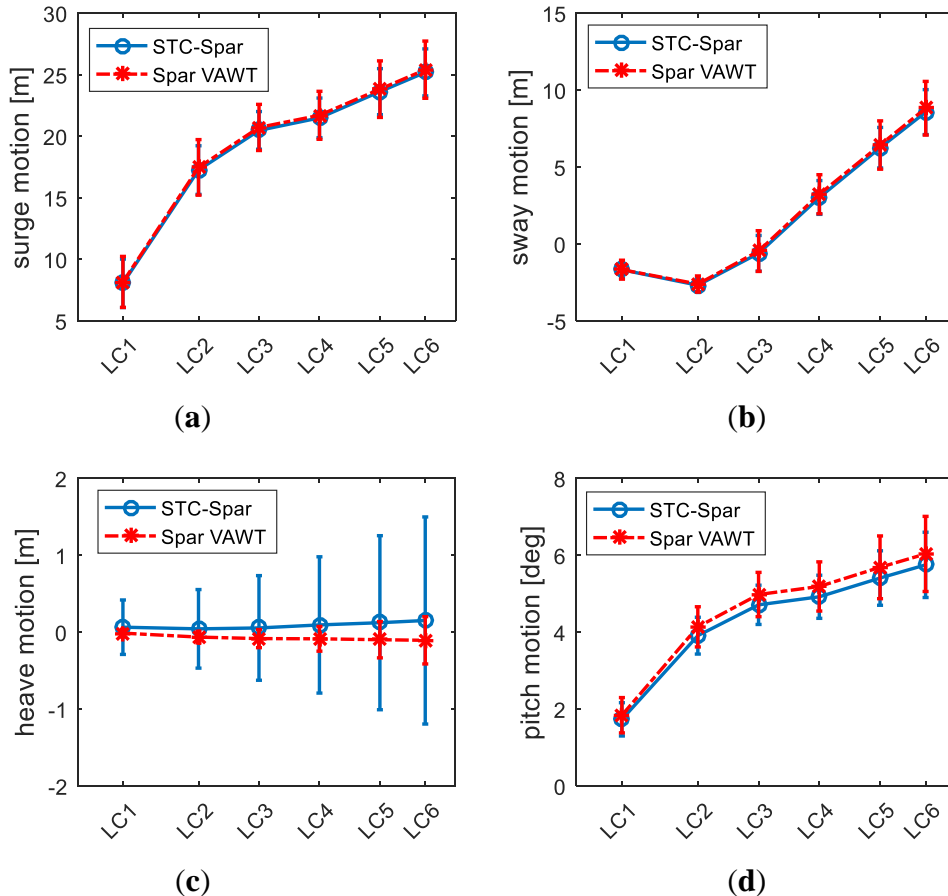


Figure 5.20. A comparative floater motion with mean values and standard deviations under all loading cases between the spar in the STC and the spar-type VAWT: (a) Surge; (b) Sway; (c) Heave; (d) Pitch.

The power spectrum analysis in the frequency domain is used to understand various combinations of time series of physical signals with different periods. Figure 5.21 displays the spectral analysis of the spar and the torus in the STC VAWT system under loading case LC3. Both the spar and the torus in the STC VAWT have identical spectral distribution, which is governed by the surge resonant response, wave response and 2P response. In heave spectrum, both the spar and the torus are dominated by the wave response and the heave resonant response, since the natural period of the STC VAWT in heave are inside the range of ocean wave periods. At mean water level, a larger wet surface of the torus may result in larger wave excitation force. Thus, a significant heave response may occur. The peak spectrum value of the torus is larger than the spar in the

STC system, and a more marked heave variation of the torus could also be found in Figure 5.19(b).

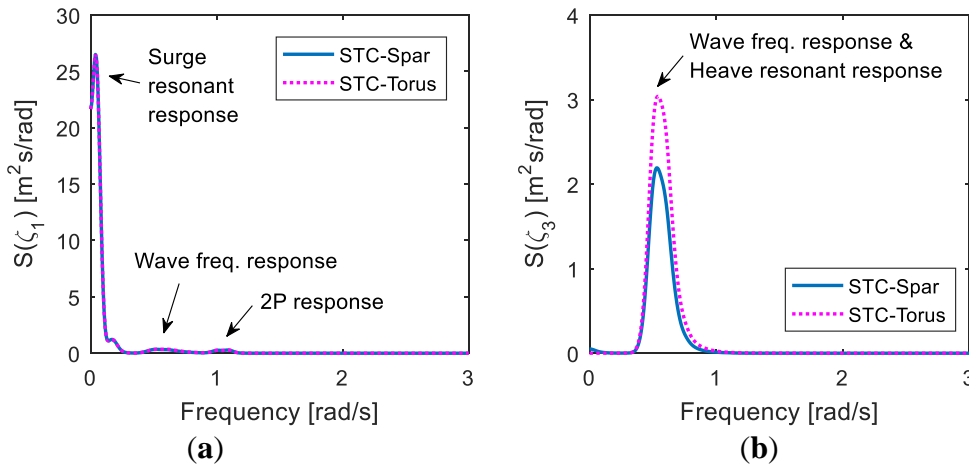


Figure 5.21. The spectral analysis of the spar and the torus in the STC VAWT under LC3 with $U_w=14\text{m/s}$, $H_s=3.62\text{m}$, and $T_p=10.29\text{s}$: (a) Surge; (b) Heave.

In addition, the comparisons of heave spectrum between the spar and the torus in the STC VAWT under LC3 and LC5 are plotted in the Figures 5.22(a) and 5.22(b), respectively. Generally, the heave spectrum remains the same distribution with different loading cases. The peak values also increase with the rising wind and wave for both the spar and the torus in the STC system.

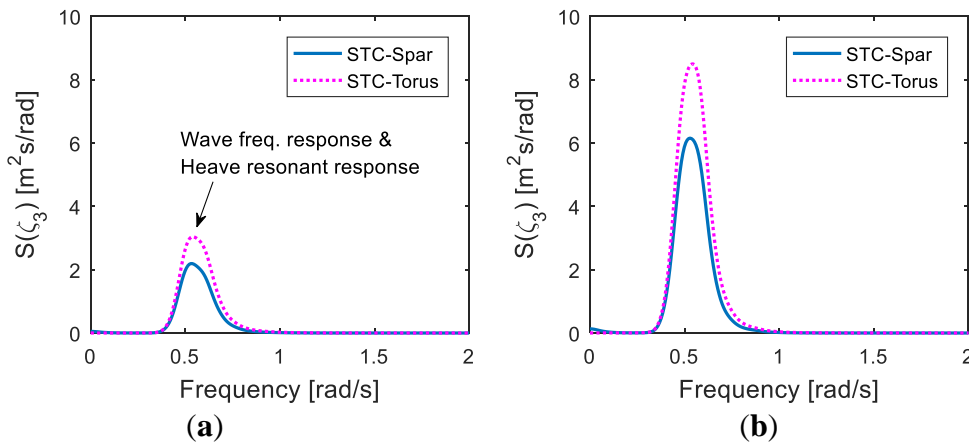


Figure 5.22. Comparisons of heave spectrum between the spar and the torus in the STC VAWT under different loading cases: (a) LC3 with $U_w=14\text{m/s}$, $H_s=3.62\text{m}$, and $T_p=10.29\text{s}$; (b) LC5 with $U_w=22\text{m/s}$, $H_s=5.32\text{m}$, and $T_p=11.06\text{s}$.

The additional torus can be also addressed by the comparison of the floater motion spectrum between the spar in the STC and the spar-type VAWT under loading case LC3 in Figure 5.23. The peak motion spectra values of the spar in the STC in surge, sway and pitch are smaller than the pure spar-type VAWT, which implies the torus in the STC

acts as a damper to reduce the corresponding responses and increase the robustness for the whole system. Regarding the heave spectrum, the spar in the STC and the spar-type VAWT differ significantly. The heave resonant frequency of the spar in the STC is much closer to the ocean wave frequency, and its peak spectrum value is extremely prominent compared with the spar-type VAWT. The torus provides additional heave stiffness and changes the heave eigenfrequency of the STC system. Thus, the wave-induced resonant response in heave could be substantial. However, this situation could be beneficial to the whole system so that the WEC could absorb more wave energy.

Figure 5.24 displays the comparisons of pitch motion spectrum between the spar in the STC and spar-type VAWT under different loading cases, both of which follow a similar distribution in principle. This figure indicates that the discrepancy in pitch resonant response increases as the weather condition enhances. The peak value of the STC VAWT in the pitch motion spectrum is much less than the spar-type VAWT, and the benefit of the torus in the whole system is also magnified under LC5.

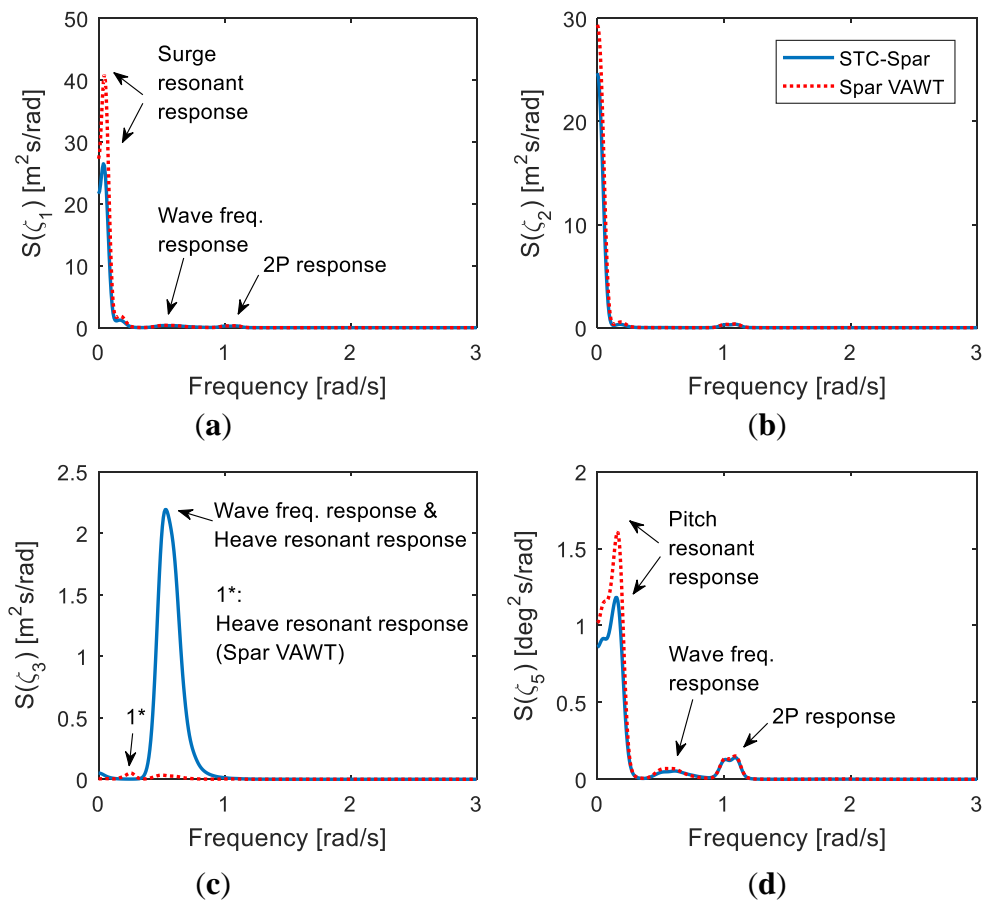


Figure 5.23. Comparative spectrum of floater motion between the spar in the STC and the spar-type VAWT under loading case LC3 with $U_w=14\text{m/s}$, $H_s=3.62\text{m}$, and $T_p=10.29\text{s}$: (a) Surge; (b) Sway; (c) Heave; (d) Pitch.

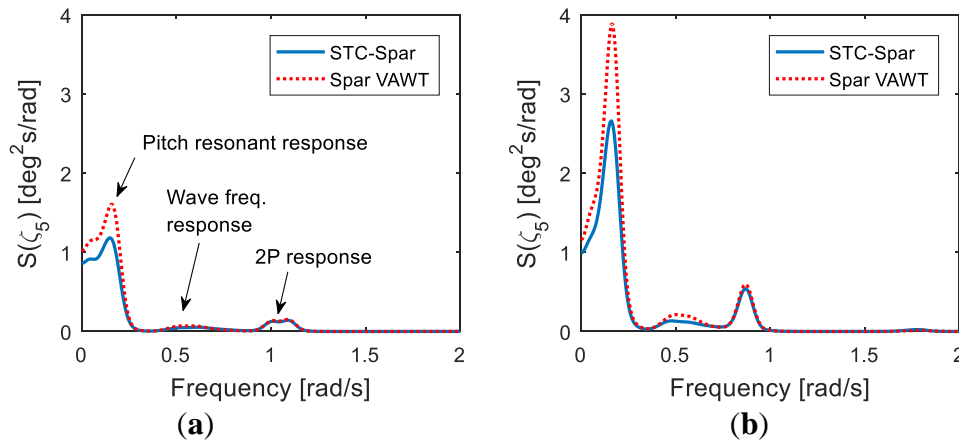


Figure 5.24. Comparisons of pitch spectrum between the spar in the STC and spar-type VAWT under different loading cases: (a) LC3 with $U_w=14\text{m/s}$, $H_s=3.62\text{m}$, and $T_p=10.29\text{s}$; (b) LC5 with $U_w=22\text{m/s}$, $H_s=5.32\text{m}$, and $T_p=11.06\text{s}$.

5.7. Tower base bending moments

The tower base bending moment are mainly caused by the aerodynamic loads on the rotor, self-weight of the floater in a tilting condition, and the wave excitation loads acting on the platform. The fore–aft and side–side bending moments, which are parallel and perpendicular to the wind flow, are considered in this study. The comparative statistics of tower base bending moment in fore–aft and side–side direction under all loading cases between the STC and the spar-type VAWT are summarized in Figure 5.25. The mean values show in a good agreement between the STC and the spar-type VAWT in both fore–aft and side–side direction.

However, the STC gives larger standard deviations of tower base bending moment than the spar-type VAWT for both fore–aft and side–side direction. Since both withstand identical aerodynamic loads, this considerable difference may result from the self-weight effect and wave excitation force. Additional bending moments of the STC system at the tower base may be induced by the gravity force of the torus in an inclined condition. Moreover, the torus of the STC system at mean sea level also generates additional wave excitation loads on itself compared to the pure spar-type VAWT. The significant variations of the tower base bending moment for the STC can be expected due to the torus effect.

Figure 5.26 displays the fore–aft and side–side moment spectra for both STC and spar-type VAWT under different loading cases. It can be clearly found that both tower base bending moment spectra are dominated by the 2P response, which is mainly induced

by periodic 2P loading. For a stronger wind and wave condition, a response close to 1.68 rad/s becomes prominent as shown in Figures 5.26(b) and 5.26(d). A possible explanation implies that the structural resonance of the rotor could be excited [14, 45]. An optimized Darrieus rotor, which can mitigate this structural resonance, is recommended for adoption according to Cheng et al. [45]. Overall, the STC presents more considerable variations of the tower base bending moment spectrum than the spar-type VAWT due to the additional torus effect.

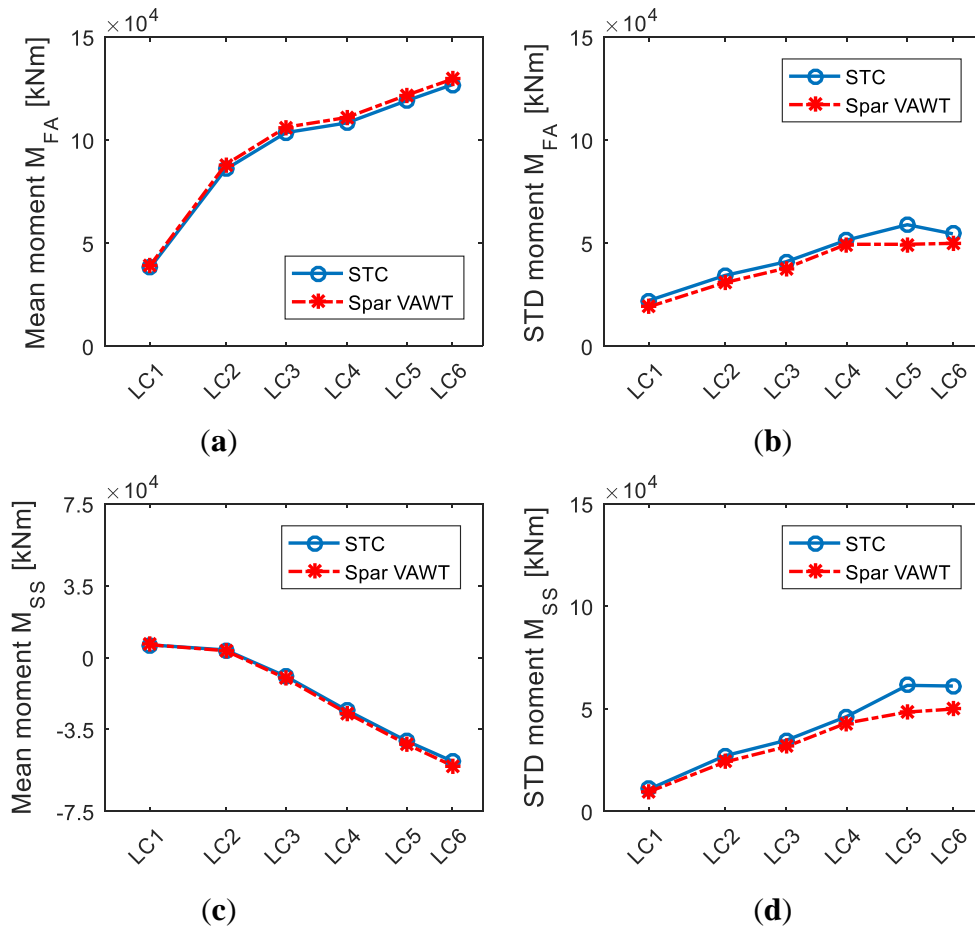


Figure 5.25. Comparative statistics of the tower base bending moment under all loading cases between the STC and the spar-type VAWT: (a) Mean values in fore-aft; (b) Standard deviations in fore-aft; (c) Mean values in side-side; (d) Standard deviations in side-side.

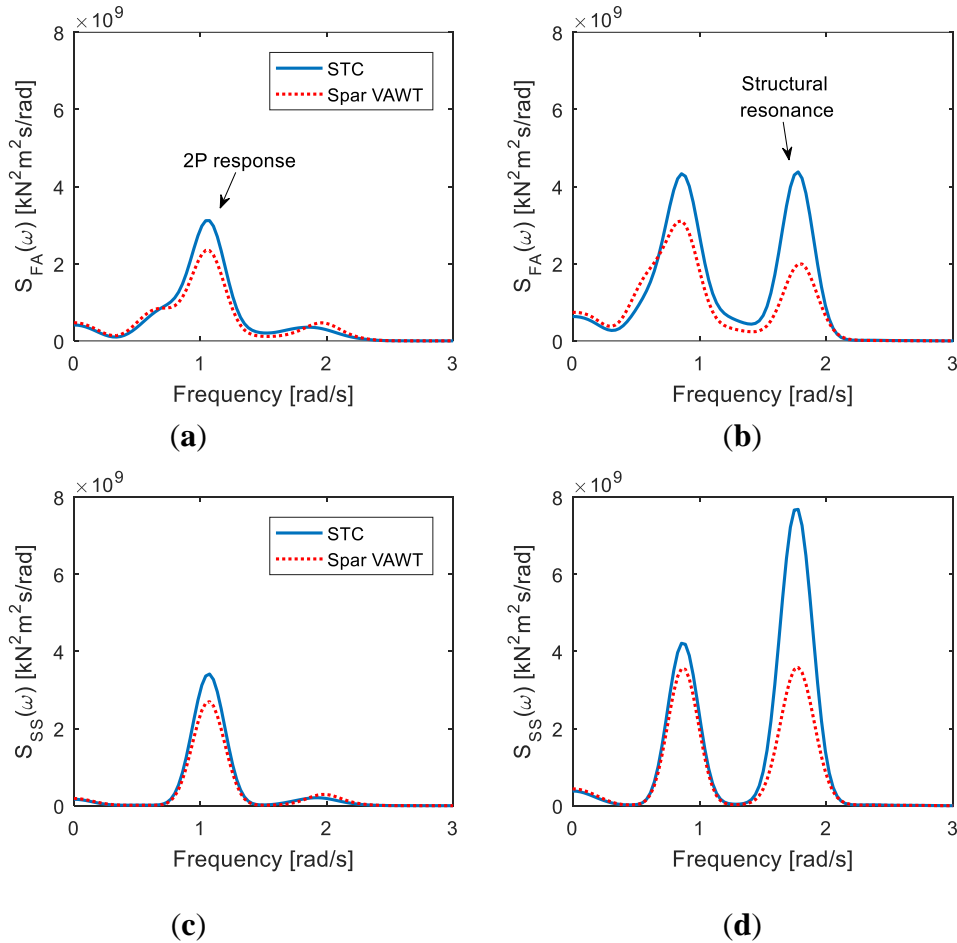


Figure 5.26. Comparisons of moment spectra between the STC and the spar-type VAWT under different loading cases: (a) Fore–aft moment spectrum under LC3; (b) Fore–aft moment spectrum under LC5; (c) Side–side moment spectrum under LC3; (d) Side–side moment spectrum under LC5.

5.8. Mooring line tension

In the catenary mooring system of the STC concept, Mooring line 1 is aligned with the turbulent wind and irregular wave direction. The Mooring line 1 is then expected to withstand the largest tension and becomes the focus of attention in the study. In addition, the identical mooring system is applied to both the STC and the spar-type VAWT. The comparisons of the tension of Mooring 1 in statistics under all loading cases for both these concepts are given in Figure 5.27. The STC displays a good agreement in the mean tension of Mooring 1 with the spar-type VAWT. The slightly larger standard deviations of the Mooring 1 tension could be observed in the STC concept. This small discrepancy may be contributed from the variations in heave motion of the STC.

The additional torus effect in the STC could be also presented through the power spectra

of the tension in Mooring 1. Comparisons of the respective spectra between the STC and spar-type VAWT under different loading cases are given in Figure 5.28. The tension spectra in Mooring 1 of the STC are mainly dominated by the low frequency due to the turbulent wind and drift force induced response. The torus of the STC can mitigate low-frequency response compared to the spar-type VAWT, since the torus plays as a damper against the surge/sway motion. However, the wave frequency response in the tension spectrum of the STC is also magnified, which could be caused by the inherent property of the STC in heave motion as mentioned in Figure 5.23(c).

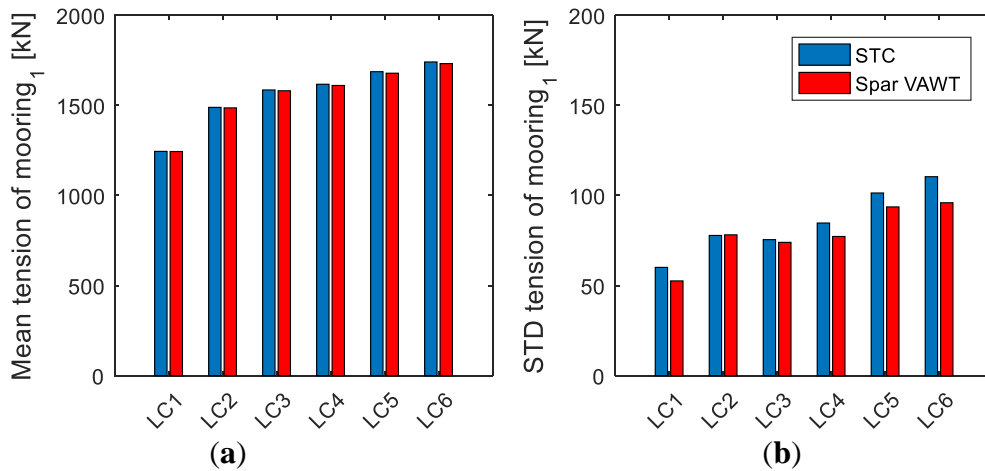


Figure 5.27. Comparisons of the tension of Mooring 1 in statistics between the STC and the spar-type VAWT under all loading cases: (a) Mean tension; (b) Standard deviations of tension.

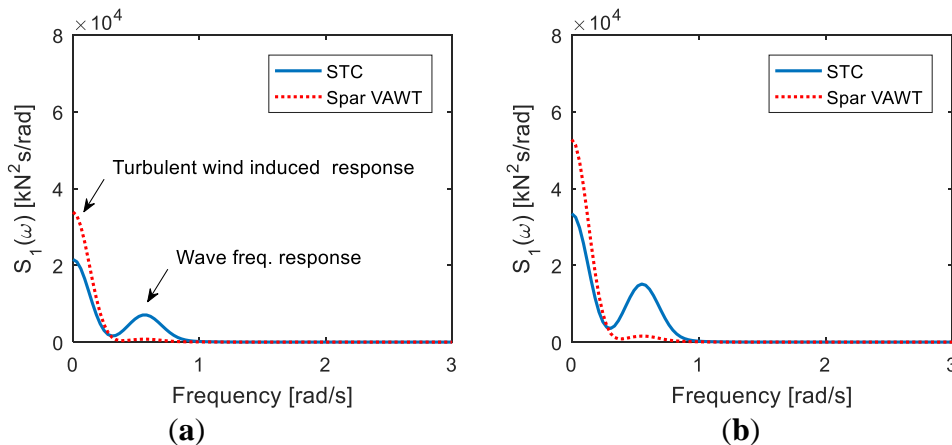


Figure 5.28. Power spectra of the tension in Mooring 1 for both the STC and the spar-type VAWT under different loading cases: (a) LC3 with $U_w=14\text{m/s}$, $H_s=3.62\text{m}$, and $T_p=10.29\text{s}$; (b) LC5 with $U_w=22\text{m/s}$, $H_s=5.32\text{m}$, and $T_p=11.06\text{s}$.

6. CONCLUSIONS

This first topic presents a comparative study of the dynamic response of the short spar and deep spar VAWTs at the different water depths through a fully coupled SIMO-RIFLEX-DMS simulation tool. The results indicate that the short spar VAWT is a feasible concept at moderate water depths 150 m. Several main conclusions in this study are given below.

- The 2P loading and the generator power production of the Short Spar VAWT agree well with those of the Deep Spar VAWT for all loading conditions. Both the 2P loading and power production increase as the wind speed increases, but the power production will remain an approximately constant value when the rated speed is reached. We conclude that the Short Spar VAWT at moderate water depth exhibits as good a performance in power generation as does the Deep Spar VAWT in deep water.
- In general, the tendency to the distribution of platform motions for both spar VAWTs is similar. However, the mean value and standard deviations of surge and sway for the Deep Spar VAWT are significantly larger than those of the Short Spar VAWT. The lower center of gravity of the Deep Spar VAWT results in larger responses in surge and sway.
- The comparison of the tower base bending moment shows a good agreement between the short spar VAWT and the deep spar VAWT. The mean, maximal values, and standard deviations of bending moments in both fore–aft and side–side directions increase as wind speed increases. Both spar VAWTs are dominated by the 2P response in bending moment spectra.
- The tension of Mooring Line 1 is designed to withstand most of the external loading in this study, since its layout aligns in the same direction as the wind and waves. The turbulence wind-induced response is particularly prominent for both spar VAWTs. The Short Spar VAWT displays higher standard deviations in the tension of Mooring Line 1, and its response spectra values are substantially larger than those of the Deep Spar.

The second study introduced the power performance and dynamic response of the Spar Torus Combination (STC) VAWT. The strength and weakness of this novel concept were discussed and analyzed in comparison with the spar-type VAWT by Cheng et al. [33]. Basically, the STC VAWT concept is applicable in operational stage, whereas further investigations should be done to verify its feasibility in the future. The main conclusions of this study are summarized and given as follows.

- The STC VAWT can simultaneously produce power through a wind turbine and a wave energy converter. The torus, which takes larger wave excitation force at the bottom, carries the spar in heave motion. The relative heave motion between the torus and the spar drives the PTO system to absorb wave energy and produce power.
- The generator power production induced by the wind between the STC VAWT and the spar-type VAWT differs insignificantly. However, the WEC from the STC provides extra wave power generation and increases the total amount of mean power production. An increment of annual power production in the combined concept due to the WEC is around 7% compared to the pure spar-type VAWT.
- The statistics on the aerodynamic loads show a good agreement between the STC VAWT and the spar-type VAWT, since both concepts carry the identical Darrieus rotor. In hydrodynamics, the torus excites additional wave loads on the STC system. The STC gives much larger standard deviations of wave excitation force than the spar-type VAWT, especially in the vertical direction.
- Regarding the floater motion, the torus acts as a damper to mitigate the low-frequency responses of the whole system in horizontal motion; hence, the STC performs smaller standard deviations of surge/sway/pitch motions. However, significant variations of heave motion can be found in the STC. The torus carries considerable wave excitation force, and the natural period of the STC in heave coincides with the ocean wave period. A notable heave response of the STC is expectable, whereas it could be beneficial for the wave power production.
- The spectral analysis of tower base bending moment in fore–aft and side–side indicates that the 2P response dominates the moment spectrum for both the STC and spar-type VAWT. The STC presents larger variations of tower base bending moment due to the additional torus effect. The induced bending moments from the torus are caused by its self-weight in an inclined condition and the extra lateral wave excitation force acting on its wet surface.

- Mooring 1 in the STC aligns with wind and wave direction so it withstands the largest tension. The STC shows slightly larger standard deviations of tension in Mooring 1 compared to the spar-type VAWT. The power spectrum of the tension in Mooring 1 also implies that the torus could decrease the low-frequency response in comparison with the spar-type VAWT. However, its wave frequency response could also be magnified due to the relatively fluctuating motion in heave with respect to the STC.

7. RECOMMENDATIONS FOR FUTURE WORK

The application of the short spar in a moderate water depth by using a fully coupled simulation method was discussed in the first study. Overall, the dynamic response of the short spar is acceptable. However, a more robust short spar can be expected to explore in the future. Several aspects to improve or expand the existing model are proposed in the following.

- The preliminary simulation shows that the short spar VAWT concept exhibits substantial variations in the tension of mooring line and a larger response value in its spectrum. An optimized design for the mooring system can be the target for the next step. The fairlead position, properties of the components, length of the mooring line and the anchoring point could affect the overall performance. A smaller variation of the mooring tension is expected in the future.
- Currently, the conceptual option of VAWT in moderate water depth has been studied and discussed. It is also interesting to explore the potential of the VAWT in shallow water. A bottom fixed foundation such as a monopile or jacket-type could be the solution. The dynamic behavior of a bottom fixed VAWT at shallow water under various environmental conditions deserve a further investigation.

In the second study, the advantages and the disadvantages of the STC VAWT concept in the operational condition have been evaluated in comparison with the spar-type VAWT. The weakness of the STC VAWT is suggested to carry out an improvement. The performance of the STC VAWT in the harsh environments is also interesting to know. Several recommendations for future work in related to the second topic are summarized as follow.

- The spectral analysis of tower base bending moment shows that the 2P response of the STC is larger than that of the spar-type VAWT. The 2P loading may be reduced by changing the blade geometry and increasing the structural strength. Cheng et al. [45] indicated that a semisubmersible with an optimized rotor could mitigate the 2P frequency response. The combination of STC VAWT and an optimized rotor could be an alternative way to decrease the variation of the tower base bending moment and should be done with further verifications.

- The STC gives larger standard deviations of mooring line tension, which could be induced by the heave motion of the torus. Too large variation of tension may cause the fatigue issue on the mooring system. A detailed design of the mooring system is recommended to conduct and make sure its reliability in ULS, ALS and FLS state. The performance of the mooring tension is also expected to be improved in the future design work.
- The current study shows that the STC VAWT is applicable in the operational mode. The stability of the STC VAWT in extreme weather condition should become the key point in next stage. The strategy of the wave energy converter in a harsh environment needs to be determined. Whether a locked mode or submerged mode could be applied to the WEC, which has been introduced by Ren et al. [32] in terms of the STC HAWT. The parameters of the power take-off system, which incorporate the stiffness and the damping term, should be assessed again. The feasibility of the STC VAWT in survival mode is recommended to pursue extensive investigations.
- So far, the dynamic responses of the STC VAWT have been only considered in the combinations of wind and wave. Due to the inherent characteristic of the spar structure, a large area of itself may expose to the current force. The current may arouse vortex induced vibration on the spar. Strakes on the hull may reduce this effect, whereas the additional added mass and drag force on the spar also need to be considered. DNV suggests that a check against the VIV should be carried out [4]. It is essential to analyze its dynamic behavior in a current condition.
- An integration of different concepts seems an efficient way to deploy the ocean energy, which can save the cost and increase the power production. Although the spar structure may encounter current force due to its deep draft, it also implies that converting current energy into electricity is highly potential. An integrated offshore renewable energy concept by Li et al. [52, 53], which incorporates the spar-type HAWT, a wave energy converter, and current turbines, could increase the total power production up to 22 to 45% based on the environmental conditions compared to the only spar HAWT. Therefore, the combination of the STC VAWT and the current turbine is another innovative topic and could be considered to do further studies.

REFERENCES

- [1] Global Wind Energy Council. Global statistics, 2017. Available online: <https://gwec.net/global-figures/graphs/> (accessed on 1 May 2018).
- [2] Urban Wind Engineering. Turbine Options: Vertical Axis vs. Horizontal Axis. Available online: [https://sites.google.com/a/temple.edu/urbanwind /services/turbine-options-and-specifications](https://sites.google.com/a/temple.edu/urbanwind/services/turbine-options-and-specifications) (accessed on 1 May 2018).
- [3] DNV GL AS. *Global Performance Analysis of Deepwater Floating Structures*; Recommended practice, DNVGL-RP-F205; DNV GL AS: Oslo, Norway, 2017.
- [4] Det Norske Veritas. *Design of floating wind turbine structures*, DNV-OS-J103; DNV AS: Norway, 2013.
- [5] JWPA. Offshore Wind Power Development in Japan, 2017. Japan Wind Power Association. Available online: <https://jwpa.jp> (accessed on 7 September 2017).
- [6] Equinor. Hywind—the world’s leading floating offshore wind solution, 2017. Available online: <https://www.equinor.com/en/what-we-do/hywind-where-the-wind-takes-us.html> (accessed on 14 June 2018).
- [7] Karimirad, M.; Moan, T. Feasibility of the Application of a Spar-type Wind Turbine at a Moderate Water Depth. *Energy Procedia* **2012**, *24* (Suppl. C), 340–350.
- [8] Karimirad, M.; Moan, T. Comparative Study of Spar-Type Wind Turbines in Deep and Moderate Water Depths. In Proceedings of the ASME 2012 31st International Conference on Ocean, Offshore and Arctic Engineering, Rio de Janeiro, Brazil, 1–6 July 2012; pp. 551–560.
- [9] Bauer, J. Future floating wind turbine technology. National Renewable Energy Laboratory, 2003. Available online: <https://www.nrel.gov/news/program/2017/nrel-market-report-finds-us-offshore-wind-industry-poised-multigigawatt-surge.html> (accessed on 5 December 2017).
- [10] Paulsen, U.S.; Pedersen, T.F.; Madsen, H.A.; Enevoldsen, K.; Nielsen, P.H.; Hattel, J.H.; Zanne, L.; Battisti, L.; Brighenti, A.; Lacaze, M. Deepwind—An Innovative Wind Turbine Concept for Offshore. In Proceedings of the European Wind Energy Association (EWEA) Annual Event, Brussels, Belgium, 14–17 March 2011.
- [11] GWIND. Spinwind1—Prototype Launch 2013. Available online: <http://www.gwind.no/?p=212> (accessed on 20 December 2017).
- [12] Paulsen, U.S.; Madsen, H.A.; Hattel, J.H.; Baran, I.; Nielsen, P.H. Design Optimization of a 5 MW Floating Offshore Vertical-axis Wind Turbine. *Energy Procedia* **2013**, *35*, 22–32.

- [13] Paulsen, U.S.; Vita, L.; Madsen, H.A.; Hattel, J.; Ritchie, E.; Leban, K.M.; Berthelsen, P.A.; Carstensen, S. 1st DeepWind 5 MW Baseline design. *Energy Procedia* **2012**, *24*, 27–35.
- [14] Wang, K. Modeling and Dynamic Analysis of a Semi-Submersible Floating Vertical Axis Wind Turbine. Ph.D. Thesis, Norwegian University of Science and Technology, Trondheim, Norway, 2015.
- [15] Cheng, Z. Integrated Dynamic Analysis of Floating Vertical Axis Wind Turbines. Ph.D. Thesis, Norwegian University of Science and Technology, Trondheim, Norway, 2016.
- [16] Ugochukwu, I.J. Structural Dynamic Analysis of Semi-submersible Floating Vertical Axis Wind Turbines. Master's Thesis, University of Stavanger, Stavanger, Norway, 2016.
- [17] Liu, L.; Guo, Y.; Jin, W.; Yuan, R. Motion Performances of a 5 MW VAWT Supported by Spar Floating Foundation With Heave Plates. In Proceedings of the ASME 2017 36th International Conference on Ocean, Offshore and Arctic Engineering, Trondheim, Norway, 25–30 June 2017; pp. V010T09A086, doi:10.1115/OMAE2017-62625.
- [18] Sandia National Laboratories. Innovative Offshore Vertical-Axis Wind Turbine Rotors. Available online: <http://energy.sandia.gov/energy/renewable-energy/wind-power/offshore-wind/innovative-offshore-vertical-axis-wind-turbine-rotors/> (accessed on 1 December 2017).
- [19] Falcão, A. F. d. O. Wave energy utilization: A review of the technologies. *Renewable and Sustainable Energy Reviews* **2010**, *14* (3), 899-918.
- [20] French, M. J. On the difficulty of inventing an economical sea wave energy converter: A personal view. Proceedings of the Institution of Mechanical Engineers, Part M: *Journal of Engineering for the Maritime Environment* **2006**, *220* (3), 149-155.
- [21] Babarit, A.; Hals, J.; Muliawan, M. J.; Kurniawan, A.; Moan, T.; Krokstad, J. Numerical benchmarking study of a selection of wave energy converters. *Renewable Energy* **2012**, *41*, 44-63.
- [22] Jaya Muliawan, M.; Gao, Z.; Moan, T.; Babarit, A., Analysis of a Two-Body Floating Wave Energy Converter With Particular Focus on the Effects of Power Take-Off and Mooring Systems on Energy Capture. *Journal of Offshore Mechanics and Arctic Engineering* **2013**, *135* (3), 031902-031902-12.
- [23] Langlee Wave Power AS. Langlee WEC. Available online: <http://renews.biz/64116/langlee-signs-ey-as-wingman/> (accessed on 1 May 2018).
- [24] MARINA Platform. Available online: <http://msp-platform.eu/projects/marina-platform> (accessed on 1 February 2018).

- [25] Michailides, C.; Gao, Z.; Moan, T. Experimental and numerical study of the response of the offshore combined wind/wave energy concept SFC in extreme environmental conditions. *Marine Structures* **2016**, *50*, 35-54.
- [26] Michailides, C.; Luan, C.; Gao, Z.; Moan, T. Effect of Flap Type Wave Energy Converters on the Response of a Semi-Submersible Wind Turbine in Operational Conditions. In Proceedings of the ASME 2014 33rd International Conference on Ocean, Offshore and Arctic Engineering, San Francisco, USA, 8–13 June 2014; pp. V09BT09A014, doi: 10.1115/OMAE2014-24065.
- [27] Muliawan, M. J.; Karimirad, M.; Moan, T.; Gao, Z. STC (Spar-Torus Combination): A Combined Spar-Type Floating Wind Turbine and Large Point Absorber Floating Wave Energy Converter — Promising and Challenging. In Proceedings of the ASME 2012 31st International Conference on Ocean, Offshore and Arctic Engineering, Rio de Janeiro, Brazil, 1–6 July 2012; pp. 667–676, doi:10.1115/OMAE2012-84272.
- [28] Aubault, A.; Alves, M.; Sarmiento, A. n.; Roddier, D.; Peiffer, A., Modeling of an Oscillating Water Column on the Floating Foundation WindFloat. In Proceedings of the ASME 2011 30th International Conference on Ocean, Offshore and Arctic Engineering, Rotterdam, The Netherlands, 19–24 June 2011; pp. 235–246, doi:10.1115/OMAE2011-49014.
- [29] Wan, L.; Gao, Z.; Moan, T.; Lugni, C. Experimental and numerical comparisons of hydrodynamic responses for a combined wind and wave energy converter concept under operational conditions. *Renewable Energy* **2016**, *93*, 87-100.
- [30] Muliawan, M. J.; Karimirad, M.; Gao, Z.; Moan, T. Extreme responses of a combined spar-type floating wind turbine and floating wave energy converter (STC) system with survival modes. *Ocean Engineering* **2013**, *65*, 71-82.
- [31] Muliawan, M. J.; Karimirad, M.; Moan, T. Dynamic response and power performance of a combined Spar-type floating wind turbine and coaxial floating wave energy converter. *Renewable Energy* **2013**, *50*, 47-57.
- [32] Ren, N.; Gao, Z.; Moan, T.; Wan, L. Long-term performance estimation of the Spar–Torus-Combination (STC) system with different survival modes. *Ocean Engineering* **2015**, *108*, 716-728.
- [33] Cheng, Z.; Wang, K.; Gao, Z.; Moan, T. Dynamic Response Analysis of Three Floating Wind Turbine Concepts with a Two-Bladed Darrieus Rotor. *J. Ocean Wind Energy* **2015**, *2*, 213–222.
- [34] Jonkman, B.J.; Kilcher, L. *TurbSim User's Guide: Version 1.06.00*; National Renewable Energy Laboratory: Golden, CO, USA, 2012.
- [35] IEC. International standard 61400-1, Wind turbines, Part 1: Design requirements, 2005.

- [36] SINTEF Ocean. *SIMO 4.10.1 Theory Manual*; SINTEF Ocean: Trondheim, Norway, 2017.
- [37] Paraschivoiu, I. *Wind turbine design : with emphasis on Darrieus concept*. Polytechnic International Press: Montréal, 2002.
- [38] Wang, K.; Hansen, M.O.L.; Moan, T. Model improvements for evaluating the effect of tower tilting on the aerodynamics of a vertical axis wind turbine. *Wind Energy* **2015**, *18*, 91–110.
- [39] Falinsen, O. M. *Sea loads on ships and offshore structures*. Cambridge University Press: Cambridge, UK, 1990.
- [40] Journée, J. M. J.; Massie, W. W. *OFFSHORE HYDROMECHANICS*; Delft University of Technology: The Netherlands, 2001.
- [41] Det Norske Veritas. *Environmental conditions and environmental loads*, DNV-RP-C205; DNV AS: Norway, 2010.
- [42] Gudmestad, O. T. *Marine technology and operations : theory & practice*. WIT Press: Southampton, 2015.
- [43] Merz, K. O.; Svendsen, H. G., A control algorithm for the deepwind floating vertical-axis wind turbine. *Journal of Renewable and Sustainable Energy* **2013**, *5* (6), 063136.
- [44] Cheng, Z.; Madsen, H.A.; Gao, Z.; Moan, T. A fully coupled method for numerical modeling and dynamic analysis of floating vertical axis wind turbines. *Renew. Energy* **2017**, *107*, 604–619.
- [45] Cheng, Z.; Wang, K.; Ong, M. C. Assessment of performance enhancement of a semi-submersible vertical axis wind turbine with an optimized Darrieus rotor. *Engineering Structures* **2018**, *167*, 227-240.
- [46] Wang, K.; Moan, T.; Hansen, M.O.L. A Method for Modeling of Floating Vertical Axis Wind Turbine. In Proceedings of the 32nd International Conference on Ocean, Offshore and Arctic Engineering, Nantes, France, 9–14 June 2013; pp. V008T09A016, doi:10.1115/OMAE2013-10289.
- [47] SINTEF Ocean. *SIMO 4.10.1 User Guide*; SINTEF Ocean: Trondheim, Norway, 2017.
- [48] WIKIPEDIA. List of Moments of Inertia. Available online: https://en.wikipedia.org/wiki/List_of_moments_of_inertia (accessed on 3 November 2017).
- [49] SINTEF Ocean. *RIFLEX 4.10.1 User Guide*; SINTEF Ocean: Trondheim, Norway, 2017.
- [50] Johannessen, K.; Meling, T.S.; Haver, S. Joint Distribution for Wind and Waves in the Northern North Sea. In Proceedings of the Eleventh International Offshore and Polar Engineering Conference, Stavanger, Norway, 17–22 June

- 2001.
- [51] Wen, T.R.; Wang, K.; Cheng, Z.; Ong, M.C. Spar-Type Vertical-Axis Wind Turbines in Moderate Water Depth: A Feasibility Study. *Energies*, **2018**, *11* (3), 555.
- [52] Li, L.; Cheng, Z.; Yuan, Z.; Gao, Y. Short-term extreme response and fatigue damage of an integrated offshore renewable energy system. *Renewable Energy* **2018**, *126*, 617-629.
- [53] Li, L.; Gao, Y.; Yuan, Z.; Day, S.; Hu, Z. Dynamic response and power production of a floating integrated wind, wave and tidal energy system. *Renewable Energy* **2018**, *116*, 412-422.

Appendix A

Paper 1

Spar-type vertical-axis wind turbines in moderate water depth: A feasibility study

Ting Rui Wen, Kai Wang, Zhengshun Cheng and Muk Chen Ong

Published in *Energies* 2018, 11(3), 555

Article

Spar-Type Vertical-Axis Wind Turbines in Moderate Water Depth: A Feasibility Study

Ting Rui Wen ¹, Kai Wang ^{2,*}, Zhengshun Cheng ^{3,4} and Muk Chen Ong ¹

¹ Department of Mechanical and Structural Engineering and Materials Science, University of Stavanger, 4036 Stavanger, Norway; tr.wen@stud.uis.no (T.R.W.); muk.c.ong@uis.no (M.C.O.)

² Aker Solutions AS, 1366 Lysaker, Norway

³ Department of Marine Technology, CeSOS and AMOS, Norwegian University of Science and Technology, 7491 Trondheim, Norway; zhengshun.cheng@gmail.com

⁴ Key Laboratory of Hydraulic Engineering Simulation and Safety, Tianjin University, Tianjin 300072, China

* Correspondence: wangkai.ntnu@gmail.com; Tel.: +47-94-122726

Received: 10 February 2018; Accepted: 1 March 2018; Published: 5 March 2018

Abstract: The applications of floating vertical-axis wind turbines (VAWTs) in deep water have been proposed and studied by several researchers recently. However, the feasibility of deploying a floating VAWT at a moderate water depth has not yet been studied. In this paper, this feasibility is thoroughly addressed by comparing the dynamic responses of spar-type VAWTs in deep water and moderate water depth. A short spar VAWT supporting a 5 MW Darrieus rotor at moderate water depth is proposed by following the deep spar concept in deep water. A fully coupled simulation tool, SIMO-RIFLEX-DMS code, is utilized to carry out time domain simulations under turbulent wind and irregular waves. Dynamic responses of the short spar and deep spar VAWTs are analyzed and compared, including the natural periods, wind turbine performance, platform motions, tower base bending moments, and tension of mooring lines. The statistical characteristics of the thrust and power production for both spars are similar. The comparison of platform motions and tower base bending moments demonstrate a good agreement for both spars, but the short spar has better performance in surge/sway motions and side–side bending moments. The 2P response dominates the bending moment spectra for both spars. A significant variation in tension of Mooring Line 1 and a larger corresponding spectrum value are found in the short spar concept. The results indicate that the application of short spar VAWTs is feasible and could become an alternative concept at moderate water depth.

Keywords: offshore wind; vertical axis wind turbine; dynamic response; spar; moderate water depth

1. Introduction

The demand for and development of global wind power energy have both significantly increased in the past decades. Wind power can be captured and converted into electricity through the use of wind turbines. Wind turbines are mainly classified into horizontal-axis wind turbines (HAWTs) and vertical-axis wind turbines (VAWTs) with regard to the direction of the rotating axis. As the aerodynamic efficiency of HAWTs is generally better than that of VAWTs, nowadays the application of HAWTs with higher commercial values is mainstream in the wind energy industry.

Since greater wind resources and potential could be explored in deeper seas, wind farms are moving towards deep water in recent years. Floating offshore wind turbines have become an available solution which could be widely used in deep water. Spar, semisubmersible, and tension-leg platform (TLP)—which have been utilized in the oil and gas industry for a long time—are three primary types of floating structures for offshore wind turbines. The dynamic responses of these floating structures in the presence of the marine environment are crucial for their design purpose. The natural period of a floater

is a critical index to represent its dynamic behavior. Typically, a spar is characterized by small heave motion, and its natural periods in surge/sway are usually higher than 100 s [1]. Additionally, several prototypes of floating HAWTs have been developed, such as a catenary moored spar in the Hywind project in Norway, a semisubmersible in the WindFloat demo in Portugal, and a spar-type floating wind turbine in Japan's Minister of Environment (MOE) project at Kabashima [2]. A commercial floating wind farm, i.e., the Hywind Scotland by Statoil, started production in 2017. The feasibility of spar-type HAWTs at different water depths has been studied by Karimirad and Moan [3,4]. Their research indicates that the short spar HAWT in moderate water depth exhibits good performance in dynamic responses and maintains almost the same power production as the deep spar HAWT in deep water.

Floating VAWTs are a promising alternative to floating HAWTs due to their potential for cost-of-energy reduction and maintenance. Additionally, the structural scalability and the heavier components at the base of the structure allow a bigger rotor diameter for the VAWT to capture more energy. For the evolution of rotor size, floating VAWTs are more competitive. However, the development of floating VAWTs is still at an early stage. Some floating VAWT concepts have been proposed to explore their feasibility, such as a spar buoy with a two-bladed Darrieus rotor in the DeepWind project [5], and a Spinwind-1 prototype with a helical Darrieus rotor and a floater from the Gwind project [6], etc. Moreover, the DeepWind project was later extended for further investigation to include a 5 MW baseline rotor and an optimized blade design with less weight and higher stiffness [7,8]. Several researchers have contributed mass efforts to floating VAWT studies in deep water conditions. Wang developed a fully coupled method (SIMO-RIFLEX-DMS code) for dynamic analysis and applied it to a semisubmersible VAWT [9]. Cheng developed another fully integrated method for VAWT numerical modeling (SIMO-RIFLEX-AC code), and studied the dynamic response for various concepts, such as the dynamic analysis of spar, TLP, and semisubmersible VAWTs, etc. [10]. Ugochukwu analyzed the structural dynamic responses of a 5 MW baseline floating VAWT and a 5 MW optimized floating VAWT with the DeepWind Darrieus rotor under steady and turbulent wind conditions [11]. Liu et al. presented a motion study of a 5 MW floating VAWT composed of a truss spar floating foundation with heave plates under decay tests, wind only, regular wave and wind, and irregular wind and wave cases [12]. Overall, most of the available floating VAWT concepts have been evaluated in deep water, whereas the feasibility of deploying a floating VAWT at a moderate water depth has not yet been discussed.

In this paper, a short spar VAWT with catenary mooring lines carrying a 5 MW Darrieus rotor in a moderate water depth (150 m) is proposed by following the deep spar concept. The methodology and modeling for both the spar VAWTs are introduced in Section 2. The dynamic response of the spar-type structure with the VAWT is analyzed through the fully coupled SIMO-RIFLEX-DMS code. Various combinations of irregular wind and wave for operating conditions are utilized to assess the response and performance of both the spar VAWTs. Section 3 presents dynamic response analysis of the short spar and deep spar VAWTs. The power performances for both the spar VAWTs are compared and evaluated. A comparative study of platform motions, tower base bending moments, and tension of mooring lines between the short spar VAWT in moderate water and deep spar VAWT in deep water is discussed. Finally, a summary of this study is shown in Section 4. The feasibility of the short spar concept in moderate water conditions is addressed.

2. Methodology and Modeling

2.1. Specifications of Deep Spar and Short Spar VAWTs

A comparison of dynamic responses between the deep spar VAWT and short spar VAWT is studied in this paper. The schematic layouts of the deep spar and short spar model are shown in Figure 1. A Darrieus 5 MW wind turbine is used for both models, and its specifications are listed in Table 1. The deep spar VAWT is a feasible concept of a catenary moored spar-type VAWT which was introduced by Cheng et al. [13]. The model of the short spar VAWT mainly follows the concept of the

spar HAWT from Karimirad and Moan [3,4], but most of details have been modified. The floater of the short spar VAWT consists of two different parts of cylinders, and heavy ballast is placed on the bottom. The dimension of the short spar and configuration of the ballast are determined through the following criteria: (a) the water depth; (b) the static equilibrium of the self-weight, buoyancy force, and the tension of mooring; and (c) the typical requirement of the initial stability.

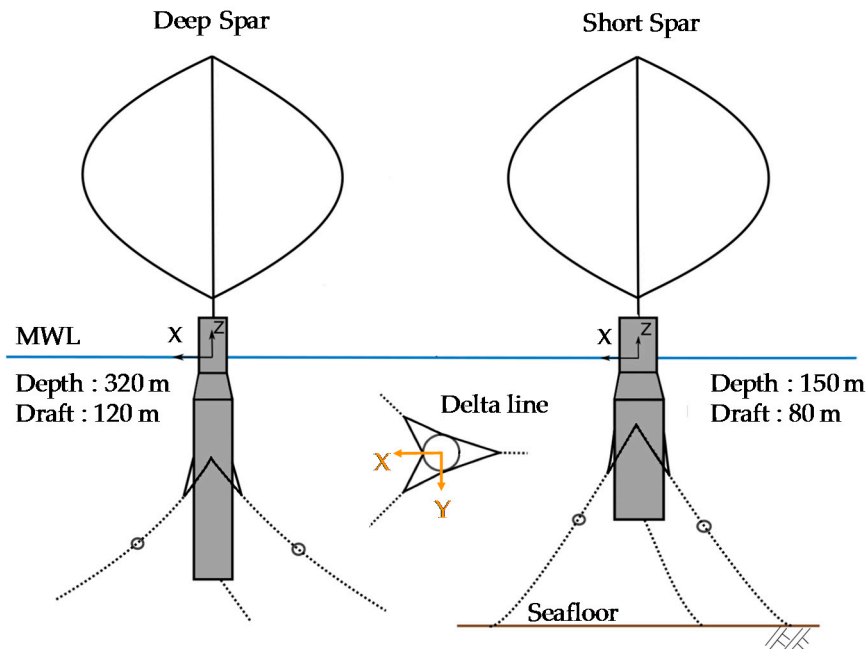


Figure 1. The diagram of the deep spar and short spar vertical-axis wind turbines (VAWTs) in deep and moderate water. Here MWL means mean water level.

Table 1. Specifications of the Darrieus 5 MW wind turbine [13].

Item	Unit	Value
Rated power	(MW)	5
Rotor height, root to root	(m)	129.56
Rotor radius	(m)	63.74
Chord length	(m)	7.45
Airfoil section	(-)	NACA 0018
Cut-in, rated, cut-out wind speed	(m/s)	5, 14, 25
Rated rotational speed	(rpm)	5.26
Total mass, incl. rotor and tower	(kg)	754,226
Center of mass	(m)	(0, 0, 75.6)

Table 2 lists the properties of the deep spar and short spar VAWTs, respectively. In principle, the water depth could limit the application of the spar in shallow water conditions. At a moderate water depth, the draft needs to be reduced so that it can achieve an adequate design. The short spar model shows that its depth is reduced to 80 m, but the diameter is increased to maintain the relevant displacement and buoyancy with the deep spar. The total mass (structural and ballast) of the short spar is 1.1% heavier than that of the deep spar. The variation of the depth of the short spar leads to a smaller mass moment of inertia in the roll and pitch directions, but the wider diameter causes a larger mass momentum in the yaw direction.

Table 2. Properties of the Deep Spar and Short Spar.

Item	Unit	Deep Spar	Short Spar
Water depth	(m)	320	150
Draft	(m)	120	80
Waterline diameter	(m)	6.5	9
Diameter at bottom	(m)	9.4	12
Hull mass, including ballast and generator	(ton)	7308.3	7962.8
COM location below MSL ¹	(m)	−89.76	−62.86
COG location below MSL ²	(m)	−74.29	−50.88
Displacement	(m ³)	8027	8642
COB location below MSL ³	(m)	−62.06	−41.68
Mass moment of inertia in roll and pitch, I _{XX} and I _{YY}	(ton·m ²)	3.362 × 10 ⁷	3.599 × 10 ⁷
Mass moment of inertia in yaw, I _{ZZ}	(ton·m ²)	1.588 × 10 ⁵	1.889 × 10 ⁵

¹ Center of Mass (COM) of floater only includes spar, ballast, and generator. ² Center of Gravity (COG) of floater includes turbine, rotor, tower, and spar (ballast). ³ COB represents the center of buoyancy; MSL refers to the mean seawater level.

The spread mooring system includes three sets of mooring lines connected with the fairlead position of the spar structure. Each mooring line has four segments which are the two delta lines, upper line, clump mass, and lower line. The delta lines can provide yaw stiffness. The water depth will govern the total length of the mooring lines. Generally, the stiffness of the mooring line in moderate water depth is stronger than that in deep water. The properties of the mooring components follow Cheng et al. [13], and the length of the mooring line in the short spar is shortened to find a sufficient design for moderate water depth. Figure 2 illustrates the layout of the mooring system for both the deep spar and short spar VAWTs. The properties of each component in the mooring system for both spar models are listed in Table 3.

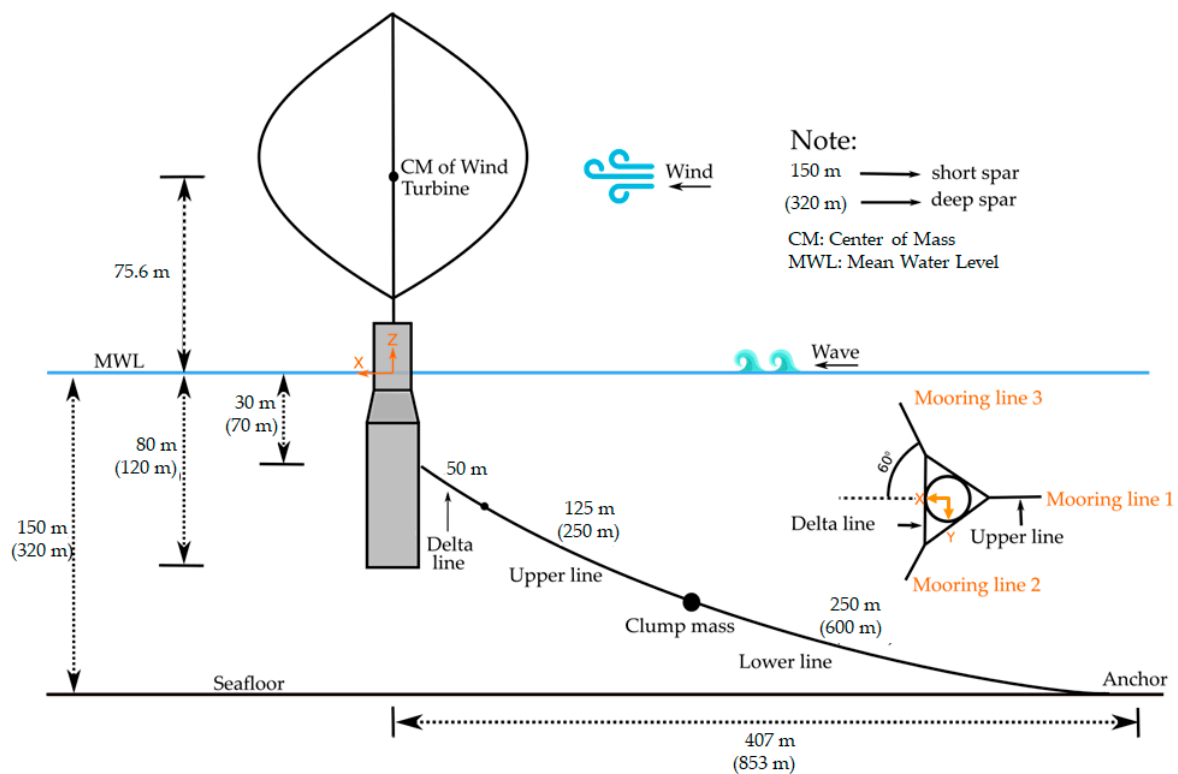


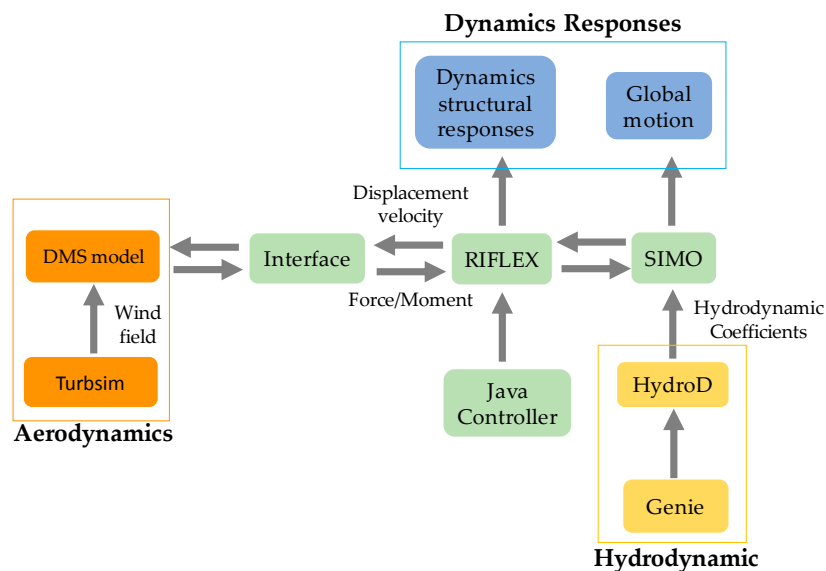
Figure 2. The diagram of the mooring system for the short spar and deep spar VAWTs.

Table 3. The properties of mooring system components.

Type	Component	Length (m)	Mass (kg/m)	Axial Stiffness (kN)
Deep Spar	Delta line	50	42.5	200,000
	Upper line	250	42.5	80,000
	Clump mass	2	17,253	80,000
	Lower line	600	42.5	60,000
Short Spar	Delta line	50	42.5	200,000
	Upper line	125	42.5	80,000
	Clump mass	2	17,253	80,000
	Lower line	250	42.5	60,000

2.2. Coupled Method for Spar VAWTs

A fully coupled simulation tool (SIMO-RIFLEX-DMS) was adopted for dynamic analysis in the time domain of the spar-type VAWTs. The flow chart is shown in Figure 3 [9]. SIMO calculates the hydrodynamic loads on the spar structure; Double-Multiple Streamtube (DMS) computes the aerodynamic loads on the blades according to the improved Double-Multiple Streamtube model; RIFLEX is a nonlinear finite element solver for estimating dynamic structural responses, and also provides links to the DMS code and an external controller. The external controller is a proportional–integral-based generator torque controller written in Java. The controller used by Cheng [10] was utilized in this study. The strategy of the controller involves maximizing the power capture for the wind speed below the rated speed and maintaining approximately constant power production for the wind speed above the rated speed. Verification of this aero-hydro-servo-elastic simulation tool (SIMO-RIFLEX-DMS) has been conducted through a series of code-to-code comparisons (HAWC2, SIMO-RIFLEX-AC) and model-to-model comparisons from Wang [14] and Cheng [15].

**Figure 3.** Computation flow chart for the coupled model (reproduced from Wang [9]).

2.2.1. HydroD Model

The hydrodynamic properties, wave loads, and motion response of the spar structure can be derived from HydroD software. The WADAM (Wave Analysis by Diffraction and Morison Theory), one of module in HydroD, was adopted to obtaining kinetic parameters including hydrostatic data, first-order wave force transfer function, retardation function, second-order wave drift force, etc. The outputs of HydroD were imported into the SIMO model.

2.2.2. SIMO Model

SIMO is a computer program for calculating the hydrodynamic loads on the spar structure [16]. The spar structure was modeled with a rigid body in SIMO, and the hydrodynamic loads mainly include first-order wave loads, second-order wave drift loads, and viscous drag force. The first-order wave loads were derived from the linear potential flow model, and the second-order wave drift loads were estimated through Newman's approximation. The viscous drag forces were calculated from the viscous term of the Morison equation and quadratic drag force coefficient.

2.2.3. RIFLEX Model

The floating VAWT system, including the blades, tower, shaft, and the mooring system, was modeled in the RIFLEX program. RIFLEX was developed as a finite element solver for analysis of mooring lines and other slender structures [17]. For the sizes and settings of the VAWT, we can refer to Wang's Ph.D. thesis [9]. The configurations of three mooring lines in the deep spar and short spar follow the specifications of the spread mooring system mentioned in Section 2.1.

2.2.4. DMS Model

The DMS model provides the aerodynamic loads acting on the blades through an external aerodynamic module. The wind turbine configuration, airfoil aerodynamic coefficients, dynamic stall data, and wind field data are required for the DMS model. The aerodynamic response of the vertical wind axis turbine using the DMS model has been verified and studied by Wang et al. [14,18]. The turbulent wind fields are generated by the "Turbsim" program [19].

2.3. Environmental Conditions

In this paper, normal operating conditions are considered for the spar VAWTs. A set of environmental conditions which were introduced from Wang were chosen for simulating the dynamic response of the spar structure [9]. The turbulent wind fields were generated from a Kaimal turbulence model in the Turbsim program according to IEC 61400-1 Class C. The JONSWAP spectrum with significant wave height (H_s) and peak period (T_p) was used for describing the irregular wave condition. These loading cases are based on the calculation of correlated wind and waves at the Statfjord site in the Northern North Sea [20]. Additionally, the wind and waves are aligned and correlated for all loading cases.

For each loading case in both spar models, five identical 4600 s simulations with random seeds were performed to express the turbulent wind and irregular wave conditions, and the mean values were derived from the time series data to reflect the stochastic variations. The 4600 s simulation can represent a one-hour duration since the first 1000 s have been filtered to eliminate the startup effect.

3. Dynamic Response of Spar VAWTs

The dynamic response of spar VAWTs was calculated through time domain nonlinear fully coupled analysis. The dynamic response includes the natural periods of spar, platform motion, structural response, tension of the mooring lines, and power production. Additionally, the comparison between the dynamic response in the deep spar and short spar VAWT were studied under different environmental conditions listed in Table 4.

Table 4. Environmental loading for normal operating conditions [9].

Load Case (LC)	U_w (m/s) ¹	T_1 (-)	H_s (m)	T_p (s)
LC1	5	0.224	2.10	9.74
LC2	10	0.157	2.88	9.98
LC3	14	0.138	3.62	10.29
LC4	18	0.127	4.44	10.66
LC5	22	0.121	5.32	11.06
LC6	25	0.117	6.02	11.38

¹ The wind speed is the mean speed at the reference height of 79.78 m above MWL.

3.1. Free Decay Tests

The natural periods of the short spar and deep spar are presented in Table 5. For the natural periods of the deep spar VAWT, we can refer to Cheng et al. [13]. Free decay tests were applied to identify the natural periods of the short spar VAWT (Figure 4). Free decay tests were carried out in calm water. The wind turbine was parked without any aerodynamic loads on the rotor, and one specified force acted in each of six degrees of direction with a very short period (200 s) to simulate its dynamic response.

For surge and sway, the natural periods of both spars are quite long. The natural period of the short spar is smaller than that of the deep spar, since the restoring stiffness of the short spar is larger due to the stiffer and shorter mooring lines. In heave, both spars are close to the upper limit of the wave periods. The short spar has a larger waterline area, and its natural period is smaller than that of the deep spar. For roll and pitch, the natural periods of both spars locate outside the range of wave periods; hence, the wave-induced resonant motions may not be substantial. However, both spars are situated inside the range of wave periods in yaw motion. Significant motion may be expected to occur in the yaw direction.

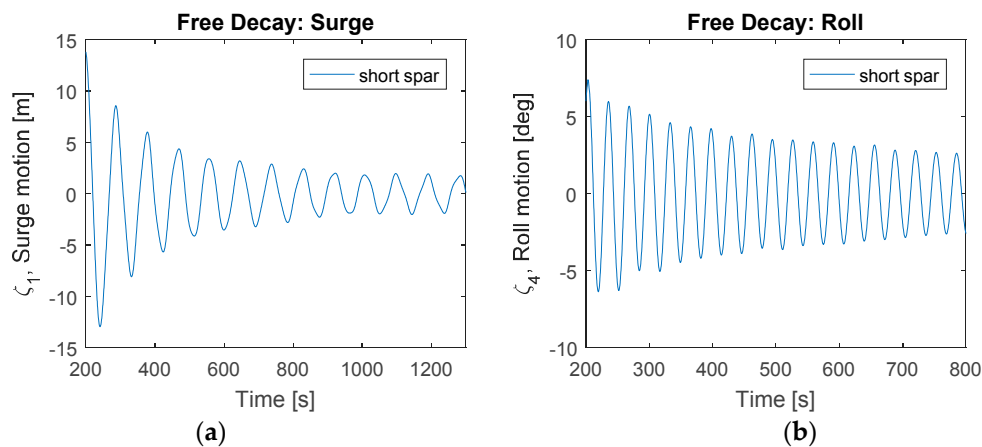


Figure 4. Free decay tests for the short spar VAWT: (a) Surge; (b) Roll.

Table 5. Natural periods of short and deep spar VAWTs.

Motion	Deep Spar ¹ (s)	Short Spar (s)
Surge/Sway	130.8	89.8
Heave	27.3	21.6
Roll/Pitch	34.5	32.5
Yaw	8.5	7.1

¹ The natural periods of the deep spar were derived from Cheng et al. [13].

3.2. Wind Turbine Performance

The rotor speed of the short spar VAWT and deep spar VAWT under all loading cases are plotted in Figure 5 and summarized in Table 6. A good agreement in rotor speed between the short and deep spar are shown in this figure. The rotor speed principally increases as the wind speed increases, but the rotor speed starts to decrease with the rising wind velocity after it reaches the rated speed. This mechanism can be explained by the fact that a Proportional Integral (PI) generator controller is employed to decrease the rotational speed in order to keep the power approximately constant [9].

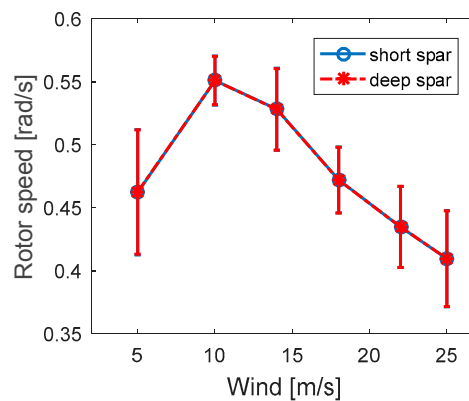


Figure 5. Mean rotor speed for the short spar VAWT and deep spar VAWT with error bar representing the standard deviation.

Table 6. Mean rotor speed for all loading cases.

Load Case	Mean Rotor Speed ¹ (rad/s)	2P Frequency ² (rad/s)	2P Period (s)
LC1	0.462	0.925	6.79
LC2	0.551	1.102	5.70
LC3	0.528	1.056	5.95
LC4	0.472	0.944	6.66
LC5	0.435	0.870	7.23
LC6	0.410	0.819	7.67

¹ The mean rotor speed can represent the 1P frequency for each load cases. ² 2P frequency is twice the 1P frequency and is the inverse of the 2P period.

The rotor rotation causes the aerodynamic loads on the spar VAWTs. One of the most prominent dynamic loads in VAWTs is the 2P loading. The blade shadowing effect and the variation in torque lead to 2P loading, which is a periodic loading. The 2P frequency is twice the 1P frequency since the Darrieus wind turbine has two blades. The 2P loading can decompose into thrust and lateral force which are parallel and normal to the wind flow direction, respectively.

A snapshot of the comparison between the 2P loading in the short spar VAWT and deep spar VAWT under rated speed (LC3) from 2000 to 2020 s is shown in Figure 6. Generally, the amplitudes of thrust and lateral force are similar. The mean value of lateral force is approximately zero, but the thrust fluctuates between zero and double the mean value. In addition, the amplitude of the short spar VAWT is almost the same as that of the deep spar VAWT in both thrust and lateral force, but the phase among these two spars is different. The average periods of thrust and lateral force are each around 6 s, which correspond to the 2P frequency.

Figure 7 displays the statistical comparisons of the thrust and lateral force for both spars under all loading cases. For simplicity, the results are plotted with the mean wind speed only even the loading includes the turbulent wind and irregular wave simultaneously. Both the comparisons indicate a good agreement between the short spar and deep spar. The mean values and standard deviations of the thrust and lateral force increase separately as the wind speed increases.

In addition, the variation of relative speed along the height of the VAWT is included in this simulation. Since both the spar VAWTs carry the same 5 MW Darrieus rotor and withstand the same environmental loadings, the aerodynamic effect of wind turbines in both models could be expected to be similar. Therefore, a further discussion about the aerodynamic effect is not shown in this work.

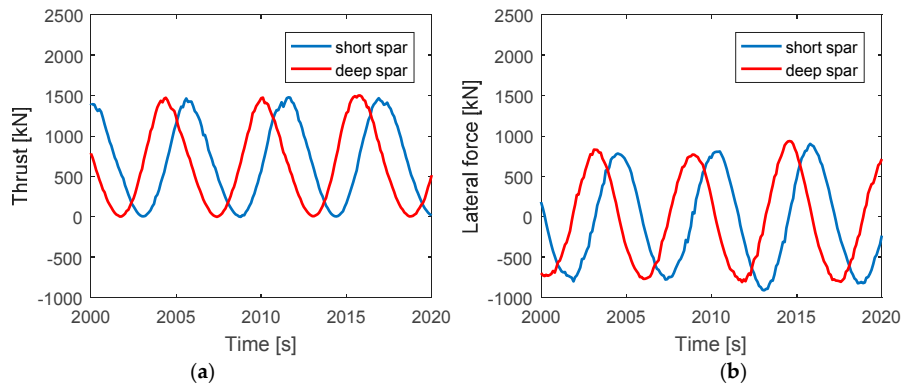


Figure 6. Comparison of time series in 2P loading for short spar and deep spar VAWTs under LC3 with $U_w = 14 \text{ m/s}$, $H_s = 3.62 \text{ m}$, $T_p = 10.29 \text{ s}$: (a) Thrust; (b) Lateral force.

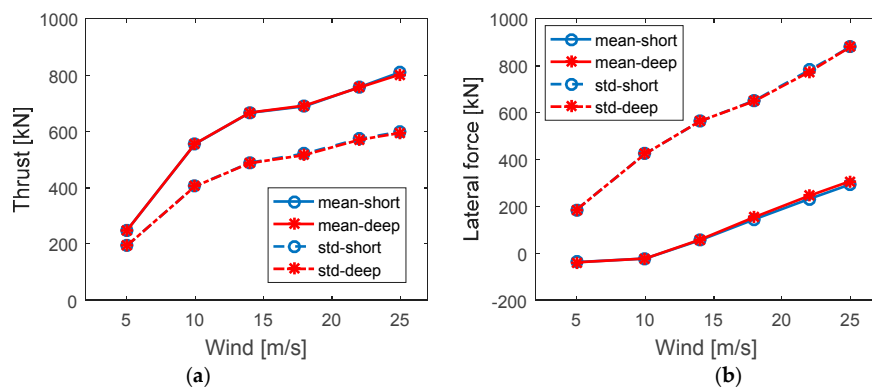


Figure 7. Comparison of mean values and standard deviations of the 2P loading for the short and deep spar VAWTs under all loading cases: (a) Thrust; (b) Lateral force.

The generator power production of the short spar VAWT and deep spar VAWT under all environmental conditions is plotted in Figure 8. This power curve shows the mean generator power production with the error bar indicating the standard deviations of the mean values. The short spar curve has a good agreement with the deep spar performance. The power production of both the short and deep spar VAWTs increases as the wind speed increases. While the wind speed exceeds the rated speed (14 m/s), the mean power production will be higher than 5 MW but remain approximately a constant value. The cause of this fact is that a PI-based generator torque controller is implemented to maintain an approximately constant generator power when the rated operation point is reached [10].

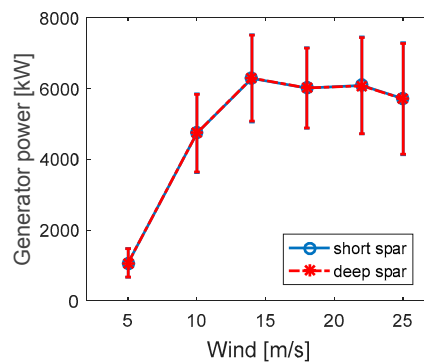


Figure 8. Mean power production for the short spar VAWT and deep spar VAWT with error bar representing the standard deviation.

3.3. Platform Motion

The platform motion can be normally divided into six degrees of freedom, which includes surge, sway, heave, roll, pitch, and yaw motions. In this paper, the heave is defined in global coordinates with the Z axis along the axial direction of the spar, and the surge is in the X axis which is parallel to the wind and wave direction (Figure 2). The comparisons of the mean values and standard deviations of the global motions under different environmental conditions between the short and deep spar VAWTs are shown in Figure 9. Similarly, the mean global motion is shown with error bars indicating the standard deviations of the mean values. Generally, the mean values of the global motions increase as the wind speed increases. Since more powerful wind will cause larger thrust and lateral force (Figure 7), stronger motions will be easily induced.

In comparing the two models in pitch and roll motions, the mean values of the short spar have good agreement with those of the deep spar. The standard deviations of the short spar are a little larger than those of the deep spar. The mean values and standard deviations of surge motion of the deep spar VAWT are significantly larger than those of the short spar VAWT. Since the surge motions were derived at the mean water level, a lower center of gravity (COG) of the deep spar VAWT with the same pitch angle could lead to larger motion in surge. However, the mean values of the deep spar VAWT in yaw motion give more significant responses than those of the short spar VAWT. This could be the reason that the natural periods of the deep spar VAWT in yaw motion are much closer to the dominating wave energy.

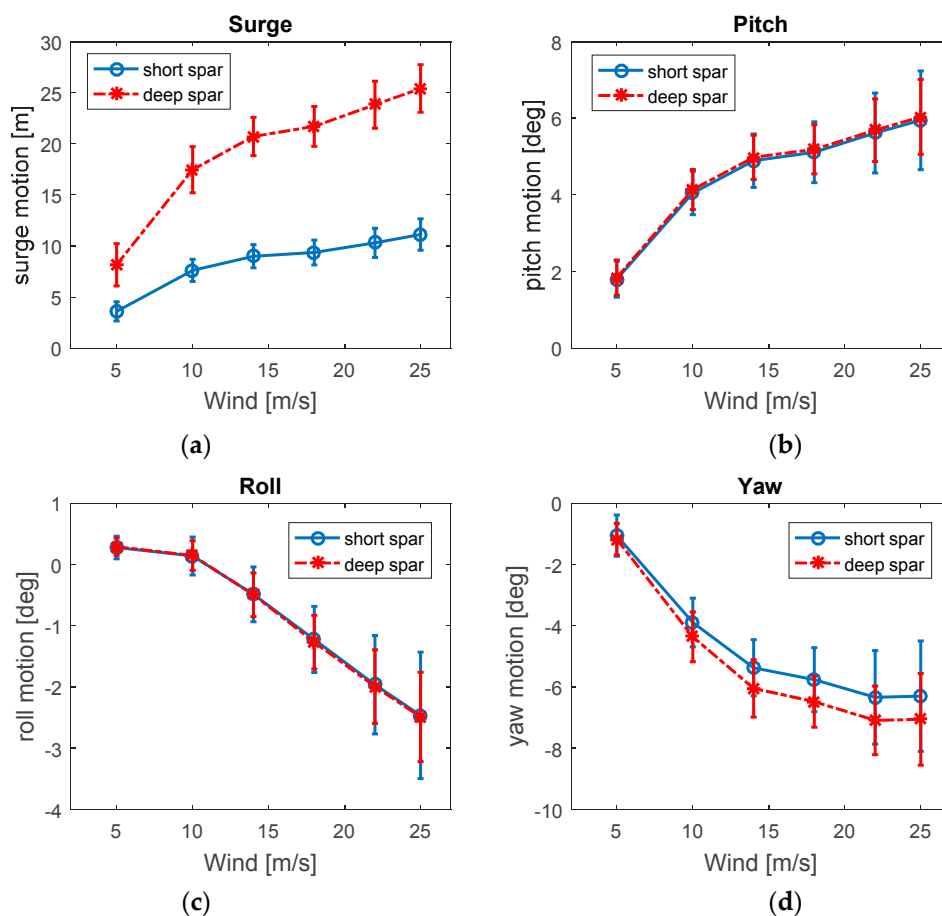


Figure 9. Comparison of mean values with error bar indicating the standard deviation in surge, heave, roll, and yaw motions for the short and deep spar VAWT: (a) Surge; (b) Pitch; (c) Roll; (d) Yaw.

The power spectra are used to analyze the time series of physical motions, which can reveal the frequency contributions in the standard deviation. A parzen window function is of benefit to filter or smooth the variation of the spectra in the frequency domain. The comparison of power spectra in six degrees of freedom between the short and deep spar under rated wind speed (LC3) can be found in Figure 10. Basically, these dynamic responses are mainly controlled by the resonant frequency, wave frequency, and 2P frequency. The short spar VAWT and deep spar VAWT have similar spectra distribution except in the heave motion. The heave motions of deep spar VAWT are dominated by its resonant response, whereas the wave-frequency-induced heave response is more prominent in the short spar.

In surge and sway motion, the deep spar VAWT has much larger resonant response. Typically, the dynamic response is determined through mass of inertia, damping, and stiffness of the system. The viscous damping terms were considered in both spar VAWT models. Owing to less discrepancy between the added mass of both spar VAWTs in surge/sway, the stiffness term becomes the key factor. Since the longer mooring lines of the deep spar VAWT result in softer restoring stiffness in the horizontal direction, a larger spectrum of surge/sway motions occur. In addition, the dominating spectra values of the short spar VAWT in roll, pitch, and yaw motion are larger than those of the deep spar VAWT. Due to a shorter metacenter height and softer restoring stiffness in roll/pitch, the higher standard deviations and larger spectrum values in roll/pitch motion could be expected from the short spar VAWT.

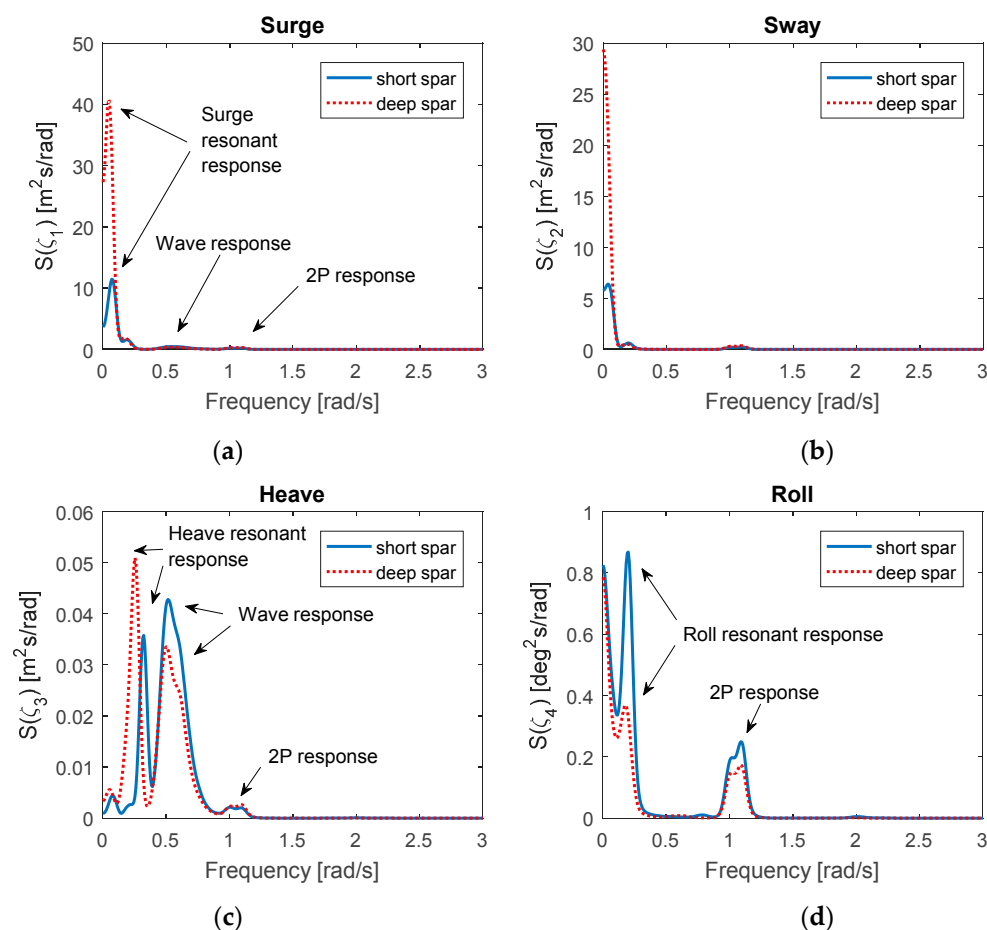


Figure 10. Cont.

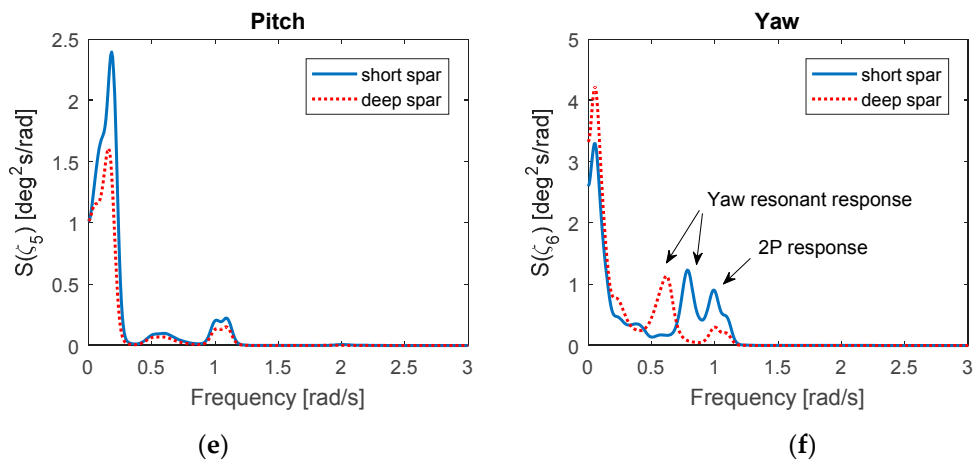


Figure 10. Comparison of power spectra in six degrees of freedom for the short and deep spar VAWT under LC3 with $U_w = 14$ m/s, $H_s = 3.62$ m, $T_p = 10.29$ s: (a) Surge; (b) Sway; (c) Heave; (d) Roll; (e) Pitch; (f) Yaw.

The power spectra of the short and deep spar VAWTs in surge under each environmental loading are plotted in Figure 11. It can be found that the low frequency induced by turbulent wind responses is dominating when the wind speed is below the rated speed (LC3). The surge resonant response dominates when the wind speed is above the rated speed and is larger than the wave response and 2P response. Overall, the dominating spectra values in the deep spar VAWT are higher than those of the short spar VAWT, and the larger standard deviations of the deep spar in surge motion can also be found in Figure 9a.

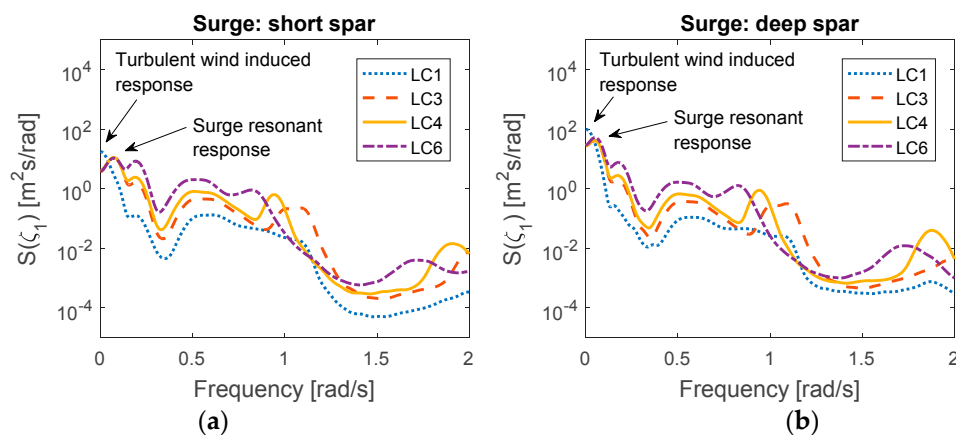


Figure 11. Power spectra in surge under all loading cases: (a) Short spar; (b) Deep spar.

3.4. Tower Base Bending Moments

The tower base bending moment is considered in this study. The bending moment is mainly induced by the aerodynamic force on the rotor and the downward gravity force of its self-weight owing to the tilted tower. The fore–aft and side–side bending moments are important indices to assess the structural performance of the wind turbine, as the aerodynamic forces vary with the azimuthal angle and cause large variation on these bending moments [9]. The fore–aft is parallel to the wind flow direction, and side–side is perpendicular to the wind flow.

Figure 12 compares the respective mean values, maxima values, and the standard deviations of fore–aft and side–side bending moments for the short and deep spar VAWTs. In this study, the maximum value in each loading case was derived from the mean of maximal numbers for each

random seed simulation in the time domain. Overall, the comparison shows a good agreement between the short spar and deep spar. The mean, maximum, and standard deviations of the bending moment in both fore–aft and side–side directions increase as wind velocity increases.

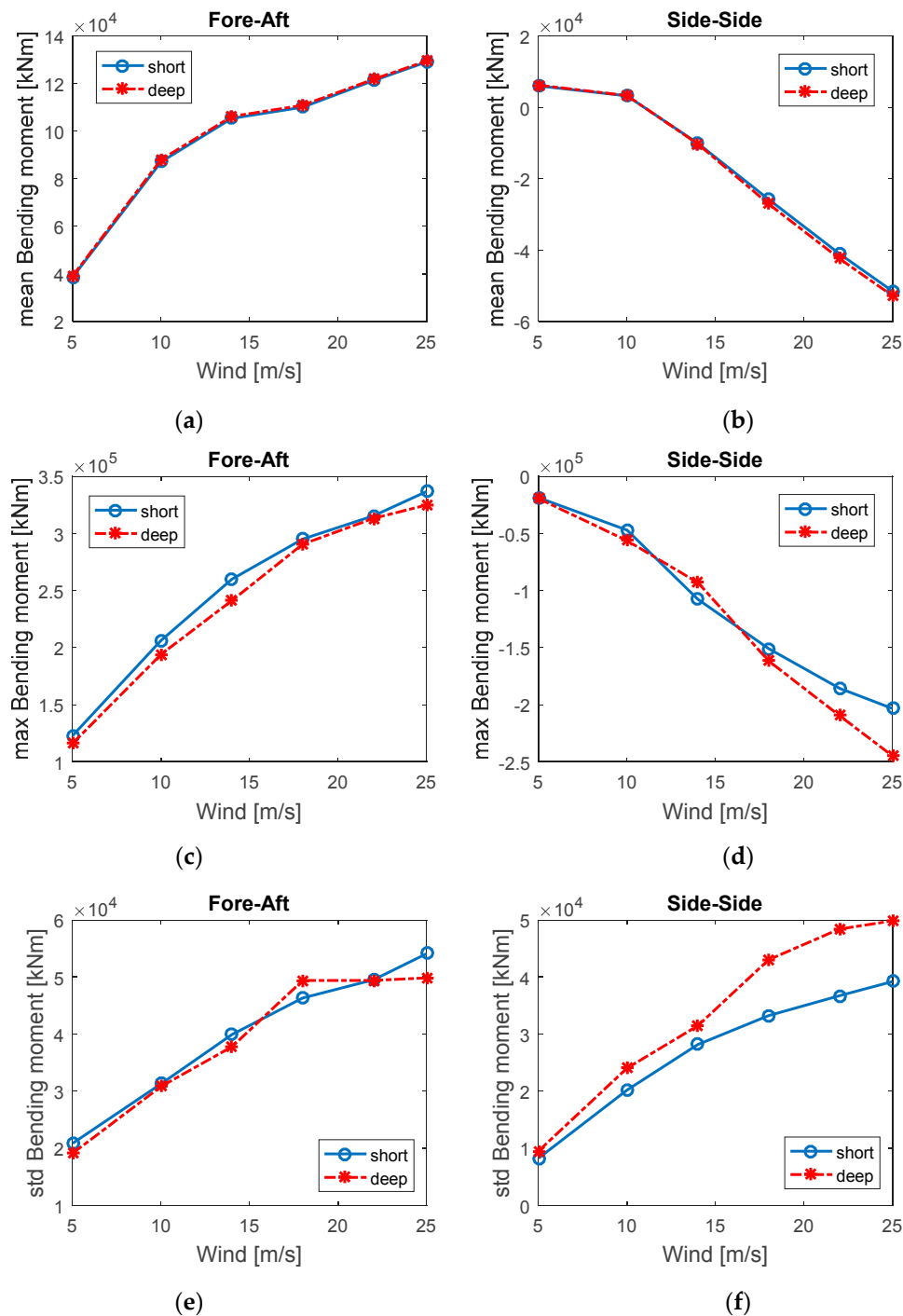


Figure 12. Statistics of tower base bending moment for the short spar and deep spar VAWTs: (a) Mean values in fore–aft; (b) Mean values in side–side; (c) Maxima values in fore–aft; (d) Maxima values in side–side; (e) Standard deviations in fore–aft; (f) Standard deviations in side–side.

The power spectra of the tower base bending moment under all environmental conditions for the short and deep spar VAWTs are shown in Figure 13. Whether in the short spar VAWT or the deep spar VAWT, 2P responses are almost dominating for all loading conditions. The response at 4P frequency

will become significant when the wind speed is over the rated speed (LC4 to LC6). The excitation may result from the structural resonance at 4P frequency when the environmental condition exceeds loading case LC3. The corresponding maxima spectra values for each loading case increase as wind velocity increases. The 2P responses of the deep spar VAWT in the tower base side–side bending moment are larger than those of the short spar VAWT, as are 2P responses in the tower base fore–aft bending moment for most loading cases. An exception is LC6 with $U_w = 25$ m/s and $H_s = 6.02$ m, under which the 2P responses of the short spar VAWT are larger than the corresponding values of the deep spar VAWT in the tower base fore–aft bending moments.

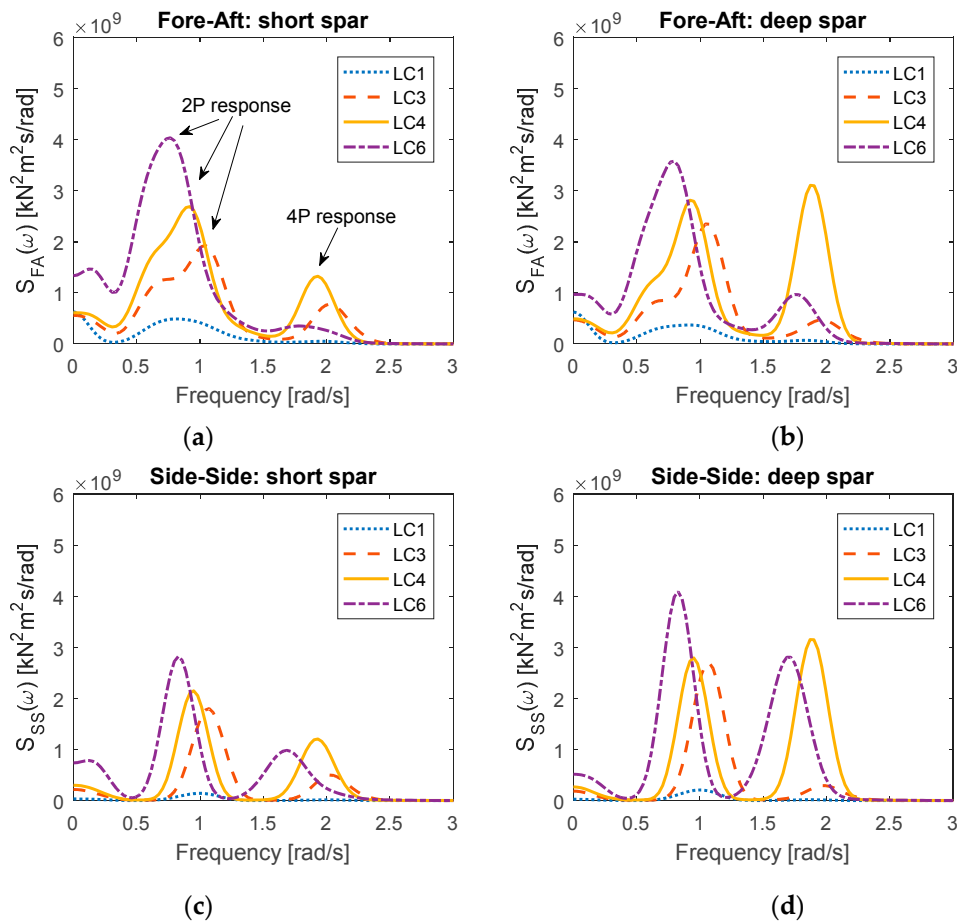


Figure 13. Power spectra of tower base bending moment under all loading cases: (a) Short spar VAWT in fore–aft direction; (b) Deep spar VAWT in fore–aft direction; (c) Short spar VAWT in side–side direction; (d) Deep spar VAWT in side–side direction.

3.5. Mooring Line Tension

The catenary mooring system is used for both the short and deep spar VAWTs. The main purpose of the mooring system is to maintain the floater in the proper position, and the delta line can provide yaw stiffness. For a conservative design approach, the turbulent wind and irregular wave are aligned in the same direction (+X global motion) in this study; hence, Mooring Line 1 will have the main role in withstanding most of the external force (Figure 2). The tension of Mooring Line 1 is measured at the anchor point and is the sum of tension in the upper line, clump mass, and lower line.

Figure 14 presents the mean values, maxima values, and standard deviations of Mooring Line 1 for the short and deep spar VAWTs under all environmental conditions. Generally, the mean, maxima values, and standard deviations increase as the wind speed and significant wave height increase.

The mean values of tension for the deep spar VAWT are larger than those of the short spar VAWT, but the maxima values and standard deviations of the deep spar VAWT are smaller.

Figure 15 compares the respective spectra of tension in Mooring Line 1 between the short spar and deep spar VAWTs under all the loading cases. Overall, the distribution of tension spectra in Mooring Line 1 for the short spar VAWT agrees well with that of the deep spar VAWT. The similarity between the short and deep spar VAWTs in the tension spectra is that the dominating wind-induced response increases as the wind speed and irregular wave state increase. However, the dominating spectra values of the short spar VAWT are significantly higher, as are the standard deviations of the tension of Mooring Line 1.

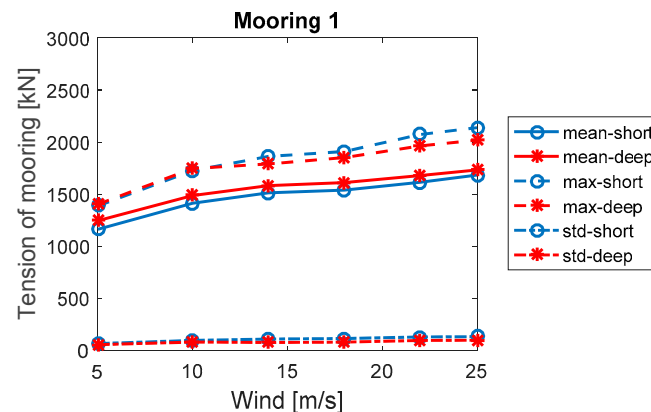


Figure 14. Statistics of the tension of Mooring Line 1 for the short spar and deep spar VAWTs.

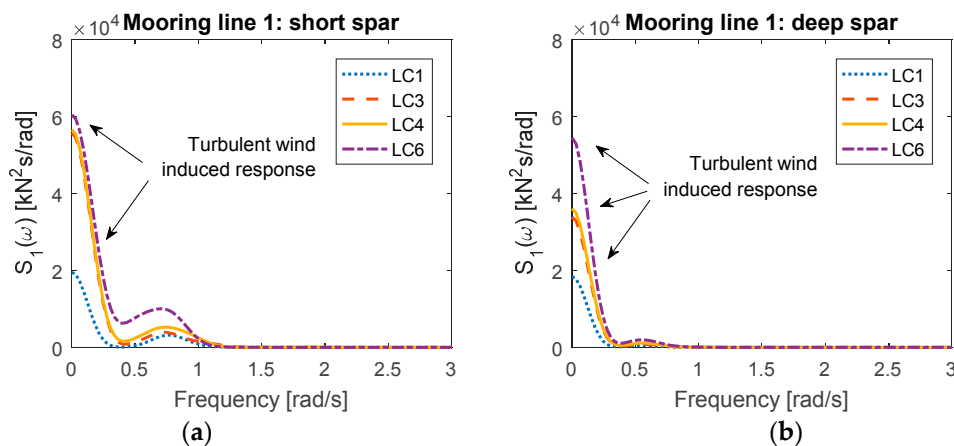


Figure 15. Power spectra of the tension in Mooring Line 1 under all loading cases: (a) Short spar VAWT; (b) Deep spar VAWT.

4. Conclusions

This paper presents a comparative study of the dynamic response of the short spar and deep spar VAWTs at the different water depths through a fully coupled SIMO-RIFLEX-DMS simulation tool. The results indicate that the short spar VAWT is a feasible concept at moderate water depths (150 m). Several main conclusions in this study are given below.

- The 2P loading and the generator power production of the short spar VAWT agree well with those of the deep spar VAWT for all loading conditions. Both the 2P loading and power production increase as the wind speed increases, but the power production will remain an approximately constant value when the rated speed is reached. We conclude that the short spar VAWT at

moderate water depth exhibits as good a performance in power generation as does the deep spar VAWT in deep water.

- In general, the tendency to the distribution of platform motions for both spar VAWTs are similar. However, the mean value and standard deviations of surge and sway for the deep spar VAWT are significantly larger than those of the short spar VAWT. The lower center of gravity of the deep spar VAWT results in larger responses in surge and sway.
- The comparison of the tower base bending moment shows a good agreement between the short spar VAWT and the deep spar VAWT. The mean, maxima values, and standard deviations of bending moments in both fore–aft and side–side directions increase as wind speed increases. Both spar VAWTs are dominated by the 2P response in bending moment spectra.
- The tension of Mooring Line 1 is designed to withstand most of external loading in this study, since its layout aligns in the same direction as the wind and waves. The turbulence wind-induced response is particularly prominent for both spar VAWTs. The short spar VAWT displays higher standard deviations in the tension of Mooring Line 1, and its response spectra values are substantially larger than those of the deep spar.

Acknowledgments: Zhengshun Cheng appreciates the support from State Key Laboratory of Hydraulic Engineering Simulation and Safety (HESS-1710), Tianjin University, China.

Author Contributions: Kai Wang and Muk Chen Ong conceived and designed the numerical study; Kai Wang and Zhengshun Cheng contributed analysis tools; Ting Rui Wen performed the simulations and analyzed the data under Kai Wang’s supervision; Ting Rui Wen wrote the paper; Kai Wang, Zhengshun Cheng and Muk Chen Ong gave comments and revised this paper.

Conflicts of Interest: The authors declare no conflict of interest.

Abbreviations

1P	One per Revolution
2P	Two per Revolution
COB	Center of Buoyancy
COG	Center of Gravity
COM	Center of Mass
HAWT	Horizontal Axis Wind Turbine
MWL	Mean Water Level
TLP	Tension Leg Platform
VAWT	Vertical Axis Wind Turbine
WADAM	Wave Analysis by Diffraction and Morison Theory
DMS	Double-Multiple Streamtube
PI	Proportional Integral

References

1. DNV GL, AS. *Global Performance Analysis of Deepwater Floating Structures; Recommended Practice*, DNVGL-RP-F205; DNV GL AS: Oslo, Norway, 2017.
2. JWPA. *Offshore Wind Power Development in Japan*, 2017. Japan Wind Power Association. Available online: <https://jwpa.jp> (accessed on 7 September 2017).
3. Karimirad, M.; Moan, T. Feasibility of the Application of a Spar-type Wind Turbine at a Moderate Water Depth. *Energy Procedia* **2012**, *24* (Suppl. C), 340–350. [[CrossRef](#)]
4. Karimirad, M.; Moan, T. Comparative Study of Spar-Type Wind Turbines in Deep and Moderate Water Depths. In *Proceedings of the ASME 2012 31st International Conference on Ocean, Offshore and Arctic Engineering*, Rio de Janeiro, Brazil, 1–6 July 2012; pp. 551–560.
5. Paulsen, U.S.; Pedersen, T.F.; Madsen, H.A.; Enevoldsen, K.; Nielsen, P.H.; Hattel, J.H.; Zanne, L.; Battisti, L.; Brighenti, A.; Lacaze, M.; et al. Deepwind—An Innovative Wind Turbine Concept for Offshore. In *Proceedings of the European Wind Energy Association (EWEA) Annual Event*, Brussels, Belgium, 14–17 March 2011.

6. GWIND. Spinwind1—Prototype Launch. 2013. Available online: <http://www.gwind.no/?p=212> (accessed on 20 December 2017).
7. Paulsen, U.S.; Vita, L.; Madsen, H.A.; Hattel, J.; Ritchie, E.; Leban, K.M.; Berthelsen, P.A.; Carstensen, S. 1st DeepWind 5 MW Baseline design. *Energy Procedia* **2012**, *24*, 27–35. [[CrossRef](#)]
8. Paulsen, U.S.; Madsen, H.A.; Hattel, J.H.; Baran, I.; Nielsen, P.H. Design Optimization of a 5 MW Floating Offshore Vertical-axis Wind Turbine. *Energy Procedia* **2013**, *35*, 22–32. [[CrossRef](#)]
9. Wang, K. Modeling and Dynamic Analysis of a Semi-Submersible Floating Vertical Axis Wind Turbine. Ph.D. Thesis, Norwegian University of Science and Technology, Trondheim, Norway, 2015.
10. Cheng, Z. Integrated Dynamic Analysis of Floating Vertical Axis Wind Turbines. Ph.D. Thesis, Norwegian University of Science and Technology, Trondheim, Norway, 2016.
11. Ugochukwu, I.J. Structural Dynamic Analysis of Semi-Submersible Floating Vertical Axis Wind Turbines. Master's Thesis, University of Stavanger, Stavanger, Norway, 2016.
12. Liu, L.; Guo, Y.; Jin, W.; Yuan, R. Motion Performances of a 5 MW VAWT Supported by Spar Floating Foundation With Heave Plates. In Proceedings of the ASME 2017 36th International Conference on Ocean, Offshore and Arctic Engineering, Trondheim, Norway, 25–30 June 2017; p. V010T09A086. [[CrossRef](#)]
13. Cheng, Z.; Wang, K.; Gao, Z.; Moan, T. Dynamic Response Analysis of Three Floating Wind Turbine Concepts with a Two-Bladed Darrieus Rotor. *J. Ocean Wind Energy* **2015**, *2*, 213–222. [[CrossRef](#)]
14. Wang, K.; Moan, T.; Hansen, M.O.L. A Method for Modeling of Floating Vertical Axis Wind Turbine. In Proceedings of the 32nd International Conference on Ocean, Offshore and Arctic Engineering, Nantes, France, 9–14 June 2013; p. V008T09A016. [[CrossRef](#)]
15. Cheng, Z.; Madsen, H.A.; Gao, Z.; Moan, T. A fully coupled method for numerical modeling and dynamic analysis of floating vertical axis wind turbines. *Renew. Energy* **2017**, *107*, 604–619. [[CrossRef](#)]
16. SINTEF Ocean. *SIMO 4.10.1 User Guide*; SINTEF Ocean: Trondheim, Norway, 2017.
17. SINTEF Ocean. *RIFLEX 4.10.1 User Guide*; SINTEF Ocean: Trondheim, Norway, 2017.
18. Wang, K.; Hansen, M.O.L.; Moan, T. Model improvements for evaluating the effect of tower tilting on the aerodynamics of a vertical axis wind turbine. *Wind Energy* **2015**, *18*, 91–110. [[CrossRef](#)]
19. Jonkman, B.J.; Kilcher, L. *TurbSim User's Guide: Version 1.06.00*; National Renewable Energy Laboratory: Golden, CO, USA, 2012.
20. Johannessen, K.; Meling, T.S.; Haver, S. Joint Distribution for Wind and Waves in the Northern North Sea. In Proceedings of the Eleventh International Offshore and Polar Engineering Conference, Stavanger, Norway, 17–22 June 2001.



© 2018 by the authors. Licensee MDPI, Basel, Switzerland. This article is an open access article distributed under the terms and conditions of the Creative Commons Attribution (CC BY) license (<http://creativecommons.org/licenses/by/4.0/>).

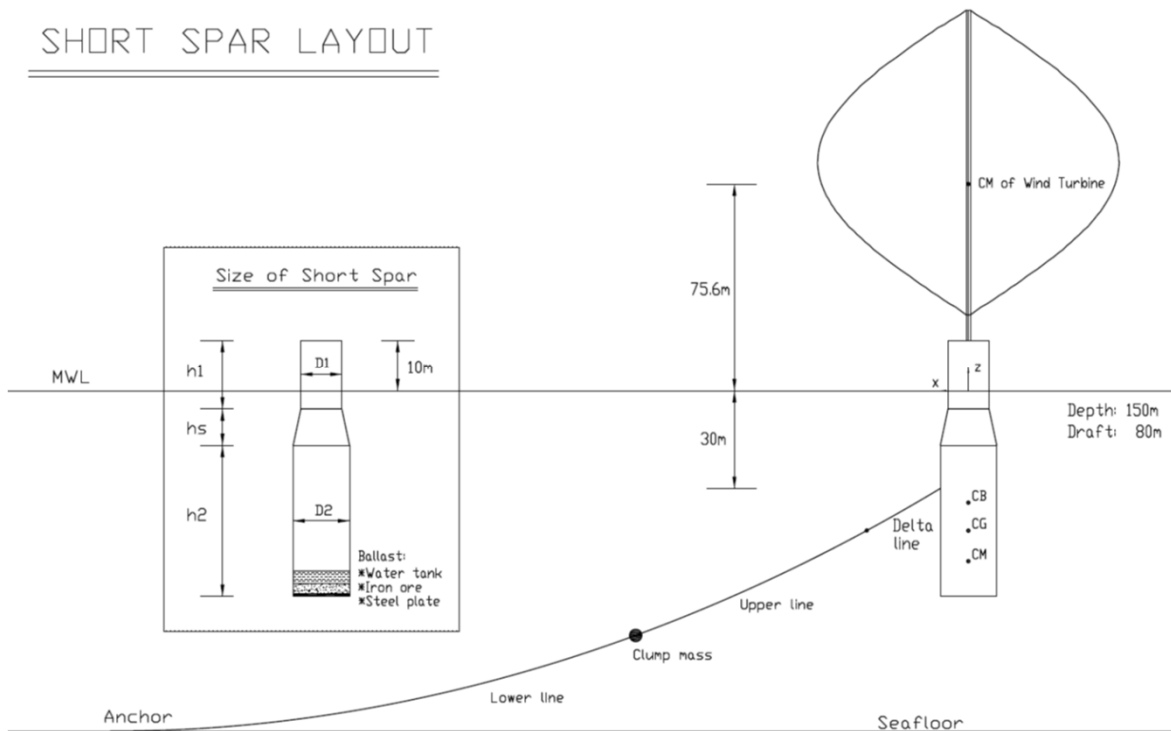
Appendix B

Calculation sheet for short spar VAWT

Appendix B: Calculation Sheet- Stability Check for the Short Spar VAWT

A. Sketch of the spar model

SHORT SPAR LAYOUT



B. Input data

Spar data

D1=	9	[m]
D2=	12	[m]
h1=	14	[m]
hs=	8	[m]
h2=	68	[m]
Z _{spar, top} =	10	[m]
ρ _{spar} =	0.30968	[ton/m ³]

Ballast data

ρ _{water} =	1	[ton/m ³]
ρ _{iron ore} =	7	[ton/m ³]
ρ _{steel} =	8	[ton/m ³]
h _{water} =	5.5	[m]
h _{iron ore} =	4.5	[m]
h _{steel} =	1	[m]

Wind turbine data

M _{turbine} =	754.226	[ton]
Z _{turbine, CM} =	75.6	[m]

Mooring line data

L _{delta} =	50	[m]
L _{upper} =	125	[m]
L _{clump} =	2	[m]
L _{lower} =	250	[m]
W _{delta} =	0.042525	[ton/m]
W _{upper} =	0.042525	[ton/m]
W _{clump} =	17.253	[ton/m]
W _{lower} =	0.042525	[ton/m]
Z _{fairlead} =	-30	[m]

Environmental data

Z _{MWL} =	0	[m]
Z _{seafloor} =	-150	[m]
ρ _{sea water} =	1.025	[ton/m ³]

C. Center of gravity

CM of spar and ballast

Type	z[m]		hi[m]	Di[m]	Vi[m ³]	Mi[ton]	z _{cm,i} [m]
spar	10	-4	14	9	890.642	275.814	3
	-4	-12	8	10.536	697.479	215.995	-8.560
	-12	-80	68	12	7690.619	2381.631	-46
water	-69	-74.5	5.5	12	622.035	622.035	-71.75
iron ore	-74.5	-79	4.5	12	508.938	3562.566	-76.75
steel	-79	-80	1	12	113.097	904.779	-79.5

$$M_{spar\&ballast} = 7962.820 \quad [\text{ton}]$$

$$CM_{spar\&ballast} = \frac{\sum M_i \times z_{cm,i}}{\sum M_i} = -62.863 \quad [\text{m}]$$

CG of spar, ballast and turbine

$$CG = \frac{M_{spar\&ballast} \times z_{CM} + M_{turbine} \times z_{CM,turbine}}{M_{spar\&ballast} + M_{turbine}} = -50.882 \quad [\text{m}]$$

D. Center of buoyancy

Type	z[m]		hi[m]	Di[m]	Vi[m ³]	F _{B,i} [ton]	z _{b,i} [m]
submerge d spar	0	-4	4	9	254.469	260.831	-2
	-4	-12	8	10.536	697.479	714.916	-8.560
	-12	-80	68	12	7690.619	7882.884	-46

$$\text{Displacement} = \sum V_i = 8642.567 \quad [\text{m}^3]$$

$$\text{Total buoyancy, } B_{\text{total}} = 8858.631 \quad [\text{ton}]$$

$$CB = \frac{\sum F_{B,i} \times z_{b,i}}{\sum F_{B,i}} = -41.683 \quad [\text{m}]$$

E. Tension of mooring lines

$$\text{Water depth from fairlead to sea bottom, } h = 120 \quad [\text{m}]$$

$$\text{Equivalent } L'_{\text{delta}} \text{ in center line} = 49.729 \quad [\text{m}]$$

$$\text{Length of catenary, } S = 426.729 \quad [\text{m}]$$

$$\text{Horizontal force, } H = \frac{W}{2h} (S^2 - h^2) = 29.714 \quad [\text{ton}]$$

$$\text{Distance to touchdown point} = 403.864 \quad [\text{m}]$$

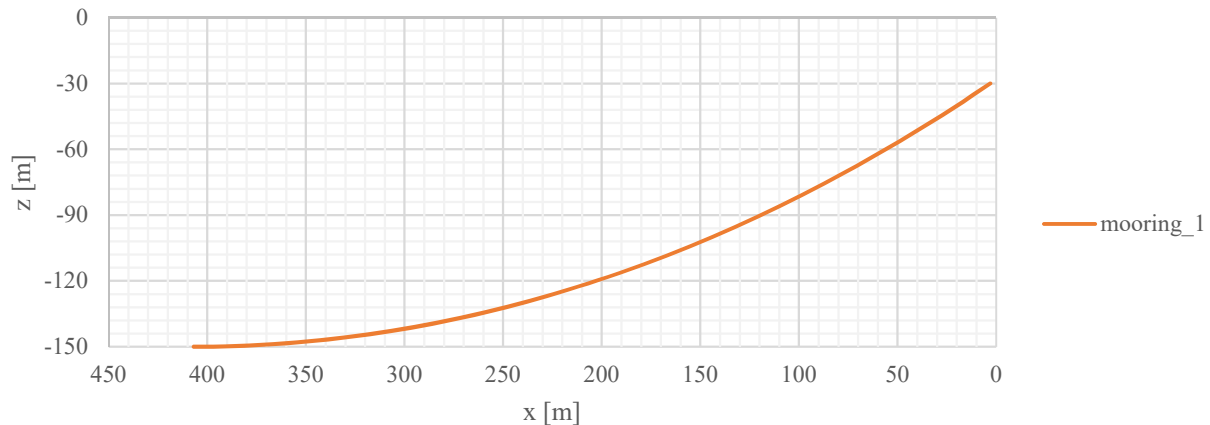
Vertical force, $V = \sum W_i \cdot S_i = 54.705$ [ton]

Total vertical force with three mooring line **164.116** [ton]

The geometry of mooring line under static equilibrium can be found from the following figure:

$$z = \frac{H}{W} \left(\cosh \frac{W}{H} x - 1 \right)$$

Short spar_mooring layout



F. Initial stability of spar VAWT

Equilibrium force check

Gravity force of spar & ballast, $F_{spar\&ballast} = 78115.27$ [kN]

Gravity force of wind turbine, $F_{turbine} = 7398.96$ [kN]

Total buoyancy force, $F_B = 86903.17$ [kN]

Total tension of mooring lines, $F_V = 1609.98$ [kN]

Equilibrium force in Z direction: $\sum F_Z = 0 \rightarrow F_{spar\&ballast} + F_{turbine} + F_V - F_B = -4.37$ [kN]

Since $\sum F_Z$ is close to zero, the spar can remain static equilibrium.

Initial stability check

Freeboard check, $f = 10$ [m] > 0 "OK"

Area inertia in roll or pitch direction, $I = \frac{1}{64} \pi D^4 = 322.062$ [m⁴]

Displacement, $\nabla = 8642.567$ [m³]

$z_{spar, bottom} = -80$ [m]

$$\overline{BM} = \frac{I}{\nabla} = 0.037 \quad [\text{m}]$$

$$\overline{KB} = CB - z_{spar,bottom} = 38.317 \quad [\text{m}]$$

$$\overline{KG} = CG - z_{spar,bottom} = 29.118 \quad [\text{m}]$$

$$\overline{KB} + \overline{BM} - \overline{KG} = 9.237 \quad [\text{m}] > 0 \quad \text{"OK"}$$

(Theory part of initial stability can be referred to chapter 2.)

Therefore, this short spar can satisfy the criteria of initial stability.